11-2023

Exploration of Motion Capture System to Investigate Human Shoulder Kinematics

Ola Alsaadi

Exploration of Motion Capture System to Investigate Human Shoulder Kinematics

Abstract

The glenohumeral joint (GH) is commonly conceptualized as a ball-and-socket joint [1], and its center of rotation (COR) is presumed to coincide with the geometric center of the medial-superior region of the humeral head [2]. Recent research has endorsed improvements in COR estimation through invasive and noninvasive techniques, including cadaver studies, stereophotogrammetry, and motion capture (MOCAP) systems. Despite increased interest in wearable technology within human movement analysis, the problem of COR estimation employing MOCAP systems and its validation against bi-planar fluoroscopy remains relatively unexplored.

This study employed a marker-based MOCAP system to compare the accuracy, error, and precision of three distinct in vivo tracking methods against the COR position identified via bi-planar fluoroscopy. The analysis conducted on a cohort of five healthy participants indicated that the accuracy of the tested methods was influenced by the type of arm movement and the arm employed (dominant vs. non-dominant).

Document Type

Masters Thesis

Degree Name

M.S.

First Advisor

Michelle Sabick

Second Advisor

Kevin Shelburne

Third Advisor

Robert Dores

Keywords

Glenohumeral joint (GH), Center of rotation (COR), Motion capture (MOCAP)

Subject Categories

Biomechanical Engineering | Biomechanics | Biomedical Engineering and Bioengineering | Engineering | Kinesiology | Life Sciences | Mechanical Engineering | Other Biomedical Engineering and Bioengineering

Exploration of Motion Capture System to Investigate Human Shoulder Kinematics

_____

A Thesis

Presented to

the Faculty of the Daniel Felix Ritchie School of Engineering and Computer Science

University of Denver

_____

In Partial Fulfillment

of the Requirements for the Degree

Master of Science

_____

by

Ola Alsaadi

November 2023

Advisor: Michelle Sabick, PhD

Author: Ola Alsaadi
Title: Exploration of Motion Capture System to Investigate the Human Shoulder Kinematics
Advisor: Michelle Sabick, PhD
Degree Date: November 2023

Abstract

The glenohumeral joint (GH) is commonly conceptualized as a ball-and-socket joint [1], and its center of rotation (COR) is presumed to coincide with the geometric center of the medial-superior region of the humeral head [2]. Recent research has endorsed improvements in COR estimation through invasive and noninvasive techniques, including cadaver studies, stereophotogrammetry, and motion capture (MOCAP) systems. Despite increased interest in wearable technology within human movement analysis, the problem of COR estimation employing MOCAP systems and its validation against bi-planar fluoroscopy remains relatively unexplored.

This study employed a marker-based MOCAP system to compare the accuracy, error, and precision of three distinct *in vivo* tracking methods against the COR position identified via bi-planar fluoroscopy. The analysis conducted on a cohort of five healthy participants indicated that the accuracy of the tested methods was influenced by the type of arm movement and the arm employed (dominant vs. non-dominant).

Acknowledgements

I want to thank my advisor, Dr. Michelle Sabick, for her guidance, patience, and mentoring. Dr. Kevin Shelburne, for his great help throughout my research. Dr. Robert Dores, for his amazing response to serve as an external chair for the committee on short notice.

I also want to thank my husband (Ali Alalwai) and my family for their encouragement, which has fueled my curiosity to learn and grow.

Lastly, I thank my research superstars (Thor Andreassen, Moira Pryhoda, Kathryn Colone, Nick Marquis, Justin Huff, and Sean Higinbotham). Your presence has made a significant impact on my education, and I appreciate the role you played in my success.

Table of Contents

List of Figures

List of Tables

Chapter One: Introduction

1.1: Introduction and Motivation

The shoulder, one of the most intricate joint systems in the human body, presents a fascinating yet challenging subject of study in biomechanics. Understanding the shoulder's musculoskeletal intricacies is pivotal, as it holds the key to refining treatments for shoulder pathologies and monitoring rehabilitation progress. The complexity of the shoulder extends to the eighteen muscles involved in its motion, posing challenges for precise kinematic analysis and clinical assessment [3].

Among the shoulder's major joints, the glenohumeral (GH) joint stands out for its remarkable range of motion (ROM), enabling various movements. However, this mobility comes at a cost: GH joint instability can lead to humeral head translation on the glenoid, resulting in discomfort and impairment [4]. Moreover, as a non-weight-bearing joint, the GH joint is susceptible to tendon overuse and structural changes in bones and muscles [5].

Shoulder-related disorders, such as rotator cuff tears, dislocations, and GH joint osteoarthritis, are prevalent and often cause significant pain and functional impairment. This underscores the importance of noninvasive shoulder kinematic data in identifying pathologies, managing symptoms, and evaluating rehabilitation effectiveness.

Epidemiological data reveal that shoulder pain affects a substantial portion of adults, making it a widespread regional pain disorder [6], [7]. Sports-related shoulder injuries are also common. For instance, swimmers experience shoulder injuries between 23% and 38% of the time [8], further emphasizing the impact of shoulder problems on daily life and overall well-being.

Diverse kinematic representations and protocols in the literature highlight the need for standardized reference positions for shoulder joints. Researchers have proposed three-dimensional models using retroreflective skin markers to establish trends toward analytical standardization [9]. Standardizing the reporting of GH joint motions based on bone landmarks is essential for consistency and effective communication [10]. But challenges like gimbal lock can arise [11].

Surface markers have been used to construct patient-specific kinematic models, demonstrating their feasibility for clinical studies of shoulder pathology [12]. Studies have also shown the reliability of optoelectronic markers for tracking scapular kinematics [13], [14].

To understand normal and pathological shoulder kinematics comprehensively, it is essential to grasp various parameters, including the Center of Rotation (COR). The accurate assessment of the COR is crucial for tasks such as motion analysis, designing robotic arm exoskeletons for rehabilitation, surgical navigation, and ensuring bone alignment during surgery. According to Nikooyan et al. [15], subject-specific musculoskeletal models should be scaled to subject-specific parameters to estimate reliable (muscle and joint reaction) forces. In addition, inaccuracies in assessing the

shoulder’s COR may result in significant inaccuracies in the scaled model's computation of some essential parameters (e.g., moment arms, origins, and insertions of the muscles crossing the GH joint).

Therefore, a profound understanding of the COR is crucial, as it serves as the foundation for various research investigations related to shoulder kinematics, inverse dynamics, moment arm calculations, and rehabilitation interventions. Accurate GH COR estimation is indispensable for biomechanical applications, such as defining the upper arm's Local Coordinate System (LCS) [10].

Marker-based MOCAP technology has advanced dramatically during the past twenty years. Camera resolutions are now routinely greater than one megapixel, and tracking software from manufacturers allows for marker replacement/switching, gap filling, and signal filtering [16]–[20].

A study by Topley et a. [21] used passive, retroreflective marker-based, commercially-available optoelectronic MOCAP systems to assess whole-body human motion to investigate the capacity of optoelectronic MOCAP systems to measure retroreflective marker positions in human movement measurement precisely. The study concluded that the precision of the marker position is mainly determined by the tracking software's algorithms and the camera system's optical properties.

This study seeks to employ a MOCAP system to comprehensively explore COR localization, addressing the challenges faced in engineering and clinical applications. Marker-based MOCAP systems are commonly used to quantify COR, with retroreflective markers tracked by infrared cameras for 3D kinematic analysis.

1.2: Objectives and Aims

The objectives of this study are:

1. Compare marker-based methodologies for locating the COR of the humeral head against the gold standard of bi-plane fluoroscopy.
2. Recommend COR techniques for various upper limb movements.

Chapter Two: Literature Review

2.1: Literature Review and Background

Understanding shoulder girdle biomechanics requires knowledge of its complex structure. The literature review chapter starts by outlining the shoulder anatomy; through its system of muscles, joints, and articulations, the shoulder girdle connects the upper limb to the rest of the skeletal system, and the different methods used to measure shoulder kinematics with their advantage and disadvantages. Lastly, this section discusses the importance of finding COR.

2.2: Shoulder Anatomy

2.2.1: The Scapula

The scapula, also known as the shoulder blade, forms the posterior part of the shoulder girdle [22] and connects the clavicle to the humerus. It is a durable, flat, triangular bone (Figure 1) with several muscle groups attached. The rotator cuff muscles are connected to the scapular surface (Figure 2) and consist of the subscapularis, teres major, infraspinatus, and supraspinatus. The complex system enables GH joint abduction external and internal rotation. The triceps, biceps, and deltoid are extrinsic muscles that work with the levator scapulae, trapezius, rhomboids, and serratus anterior muscles to control the scapula's rotational movements and provide stability.

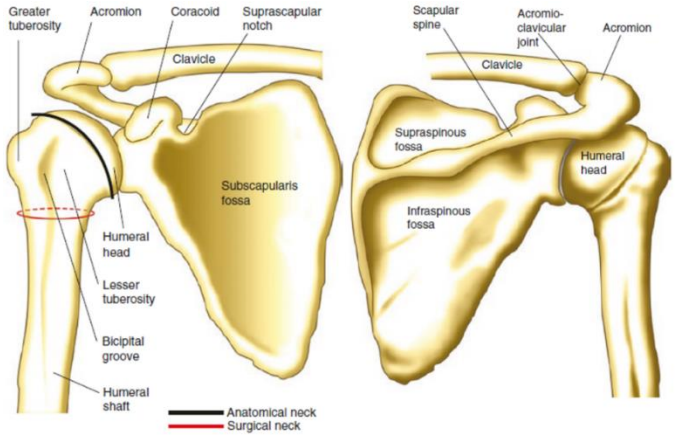

Figure 1: Shoulder bones (anterior and posterior views) [3].

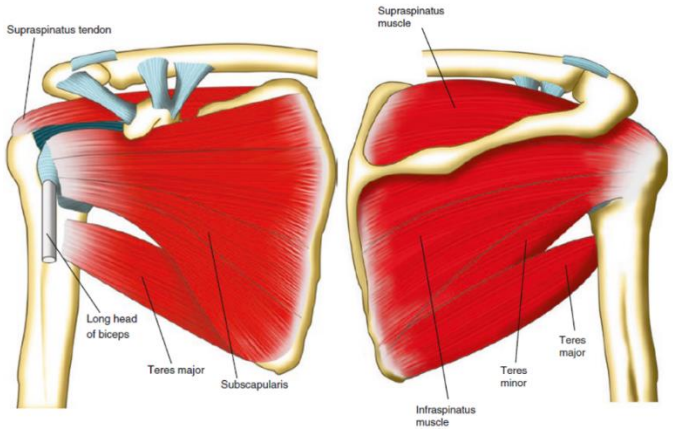

Figure 2: Shoulder muscles (anterior and posterior views) [3].

The scapula engages in six different motions essential in the mechanical function of the shoulder girdle described below (Figure 3), using the glenoid as the point of reference [23] to enable fully functional movement of the upper extremities [24]:

- **Protraction** – The pulling forward of the shoulders using the latissimus dorsi, rhomboids, and trapezius muscles.
- **Retraction** – The pulling backward motion of the shoulders using the same muscles as protraction in the opposite direction.
- **Elevation** – The upward "shrugging" motion with the natural direction of the glenoid enabled using the trapezius, levator scapulae, and rhomboid muscles.
- **Depression** – The downward pulling motion in opposition to elevation and against the glenoid using the latissimus dorsi, serratus anterior, pectoralis major and minor, and trapezius muscles.
- **Upward Rotation** – The motion about the glenoid with the trapezius and serratus anterior muscles to lift the arms.
- **Downward Rotation** – The motion of the glenoid using the latissimus dorsi, levator scapulae, rhomboids, and the pectoralis major and minor muscles to lower the arms.

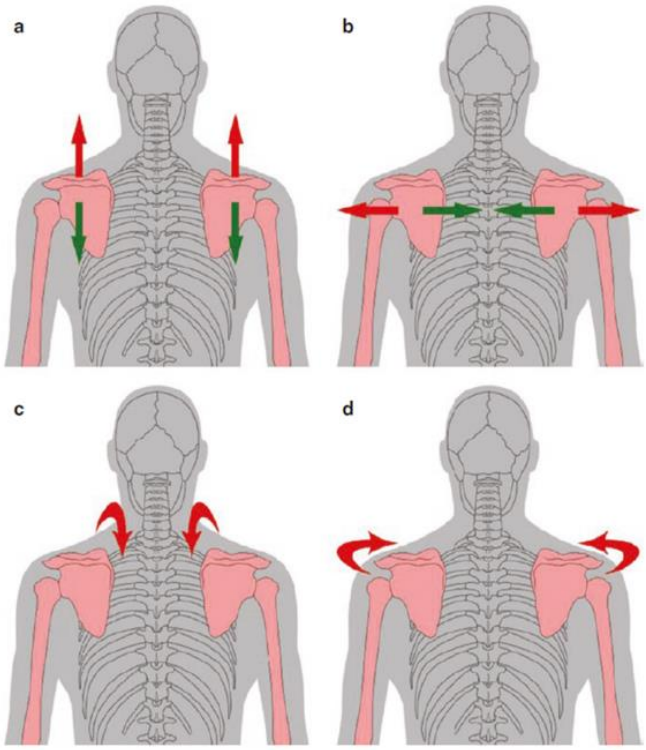

Figure 3: Directions of scapular movements:
(a) upward/downward, (b) medial/lateral, (c) rotation,
and (d) protraction [3].

2.2.2: The Humerus

The humerus consists of a proximal portion, the head, which forms the synovial GH ball and socket joint along with the glenoid fossa on the scapula, allowing for movement with six degrees of freedom (6DOF). The head of the humerus is divided by an inferior residual epiphyseal part of the neck into two regions: the greater and lesser tubercles (Figure 4). Moving distally is the cylindrical shaft of the humerus, which contains a deltoid tubercle on its lateral aspect and a radial groove on its posterior part, the spiral groove [25]. The subacromial, subdeltoid, subcoracoid, and coracobrachialis bursae are the synovial bursae found in the GH joint that allow for frictionless movement by the

humerus about the humeral head. The coracoacromial and acromioclavicular ligaments stabilize the GH joint, stopping the humerus from migrating proximally.

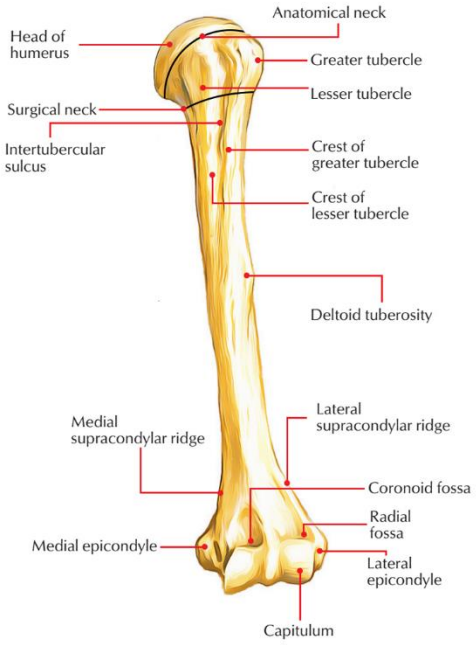

Figure 4: Humerus bone anatomy
(https://www.earthslab.com/anatomy/humerus/)

2.3: Shoulder Girdle Joints

The sternoclavicular (SC), acromioclavicular (AC), and scapulothoracic joints, as well as the GH joint [26], are the four joints that make up the shoulder girdle (Figure 5). The SC joint is a synovial saddle joint that connects the upper limb to the axial skeleton. The costoclavicular ligament stabilizes and joins the clavicle to the manubrium of the sternum. The AC joint is a planar synovial joint that binds the acromion of the scapula and the clavicle and is stabilized primarily by the coracoclavicular ligament and supported by the superior and inferior AC ligaments.

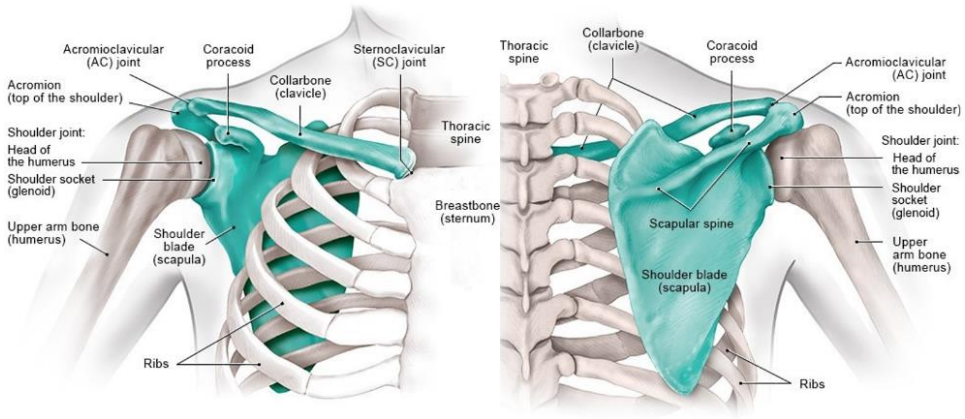

Figure 5: Joints of the shoulder girdle (pectoral girdle)
anterior and posterior views
(https://www.informedhealth.org/how-does-the-shoulder-work.html).

Unlike traditional joints, the scapulothoracic joint is formed by the scapula gliding over the posterior thoracic cage. The GH joint is supported by the tendons of the biceps and triceps brachii and the rotator cuff muscles, which adhere to the joint capsule. The shallow articulation of the glenoid fossa alone can only hold around one-third of the humeral head, so the fibrocartilaginous ring known as the labrum adds depth and rigidity, holding the humeral head in place. The capsule is surrounded by many bursae, which help with motility (Figure 6).

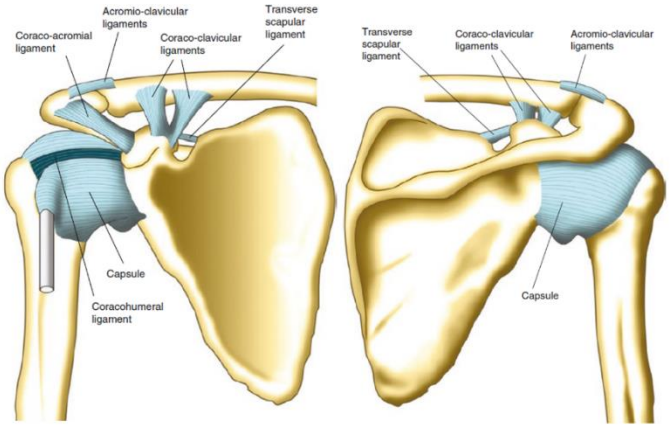

Figure 6: Shoulder capsule and ligaments
(anterior and posterior views)
[3].

2.4: Different Methods Used in Measuring Shoulder Kinematics

Over the years, various research projects have aimed to track shoulder biomechanics using different techniques to find a better way to treat shoulder injuries and investigate strategies to develop better medical devices. Some methods could be very low-tech and designed for simplicity, like using templates to fit a coordinate system to the scapular anatomy observable on standardized radiographs [27]. Other studies use noninvasive, non-radioactive methods to measure shoulder mechanics, such as a goniometer or a digital inclinometer, and some use high-tech methods with advanced features to investigate and track the shoulder, like wearable sensors [28] and MOCAP systems.

2.4.1: Cadaver-Based Experimental Methods

Cadaveric research has played a significant role in discovering all shoulder anatomical structures and elucidating their biomechanical function (Figures 7 and 8). Cadaver studies have been used to clarify how the anterior and posterior rotator cuff

structures contribute to shoulder instability [29]. Additionally, cadavers were used to quantify the moment arms of the muscles around the GH joint [30].

Cadavers were used by Fung et al. [31] to compare rotation of the scapula and clavicle as a function of humeral elevation for multiple elevation planes during a simulated passive ROM examination by applying a combination of *in vitro* kinematic testing and graphic reconstruction of cadaveric bony anatomy; the study found that the biggest scapular and clavicular rotations were produced by elevation in the coronal plane, which was followed by elevation in the scapular plane at low elevation angles.

A cadaver study by Karduna et al. [32] used eight fresh-frozen human cadaver glenohumeral joints fastened to a mechanical testing apparatus using a specially designed translation table. The GH joint's superior translation was simulated, and various scapular posterior tilting, upward rotation, and external rotation angles were examined on the specimens; the study found that posterior tilting did not influence subacromial contact forces, demonstrating the value of using cadavers in numerous shoulder studies.

A study by Teece et al. [33] showed that there are similar patterns of shoulder girdle motion during progressive humeral elevation (AC joint internal rotation, upward rotation, and posterior tilting) when comparing passive movement in cadaver specimens to patients' active motion during scapular plane abduction.

Recording the passive motion of a cadaveric model also enabled investigation into passive AC joint motion under normal gravitational forces. The closeness of motion patterns between the active and passive circumstances shows that passive tension in the

soft tissues, joint capsule, ligaments, and the form of the thorax influence motion and position.

A biomechanical study by Hartzler et al. [34] used cadavers in modeling tendon transfer and found that in a native shoulder, transferring the teres major and latissimus dorsi proximally to the anterior footprint of the supraspinatus could efficiently restore active internal rotation especially when the arm was abducted, proving the feasibility of transferring the shoulder.

CT data of cadaver scapulae were also employed to examine the accurate positioning of the glenoid by [35] using 3D surface models of CT data for ten human scapulae. The 3D models were printed to investigate the precise positioning of the glenoid in reverse total shoulder arthroplasty (RTSA), using augmented reality technology to improve and enhance surgical planning.

Despite its long historical significance, using cadavers in research can be costly and time-consuming. The applicability of results collected in cadavers to living subjects is often limited since cadavers do not have muscle activity or neurological function.

Numerous studies investigated the feasibility of using acromion marker clusters to track scapular kinematics using cadavers. For example, Cereatti et al. [36] concluded that because no muscles, including the deltoid, were contracting when using a cadaveric model, the soft tissue artifacts that affected scapular tracking differed from those seen during active motions. Therefore, kinematic assessment using acromion marker clusters is only appropriate when looking at passive shoulder movements with little to no muscular activity.

Shoulder biomechanics researchers prefer noninvasive procedures using living patients to overcome the drawbacks of cadaver research. Live human subject testing has generated helpful information about scapular movement training and clinical outcomes [37].

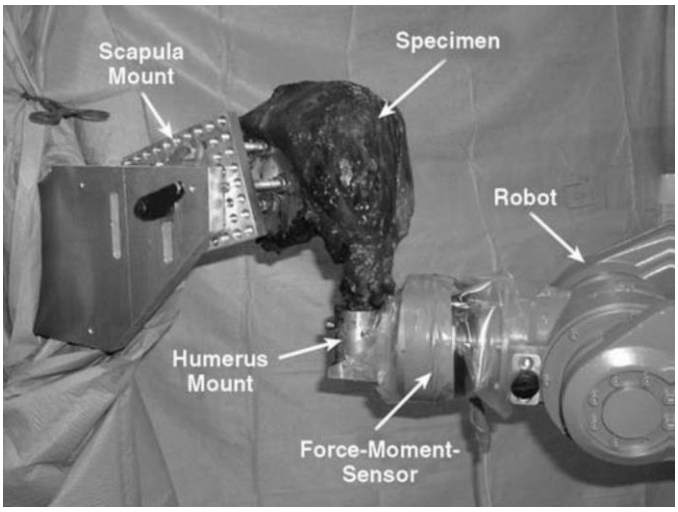

Figure 7: Close-up view of shoulder specimen mounted in a robot-assisted kinematic simulator with a force-moment sensor [38].

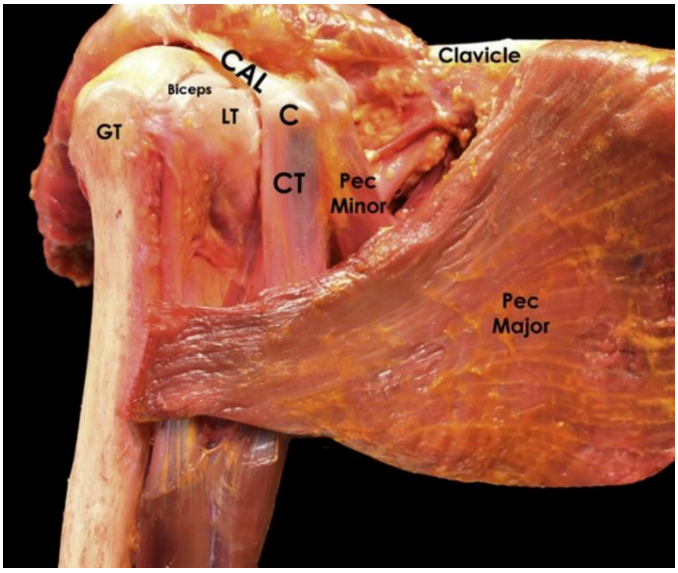

Figure 8: Shoulder anatomy (Cadaver) [39].

2.4.2: Ultrasound

Ultrasound (US) is a noninvasive, *in vivo* medical imaging technique that uses high-frequency sound waves ranging from 2 to 20 MHz to produce real-time images or video of internal organs or other soft tissues, but not of joints or deeper structures obstructed by bone. Ultrasonography is an effective and accurate technique for evaluating soft tissue injuries to the shoulder due to its dynamic nature. It has several advantages over other imaging modalities, including low cost compared to magnetic resonance imaging (MRI) [40]. It detects tendon degeneration, bursitis, and rotator cuff injuries with excellent sensitivity. The US is also an effective technology for needle-guided diagnostic and therapeutic operations.

To acquire significant diagnostic value from the US, a thorough understanding of shoulder anatomy and transducer location is essential [41].

Another advantage of the US is portability, active real-time examination, and no radiation, so tests and trials may be repeated and last longer without worrying about the hazard of radiation (Figures 9 and 10). As a result, it is frequently used to check for rotator cuff problems and shoulder impingement syndrome [42]. The US offers a valuable tool for comprehending how muscles and tendons interact or may get damaged due to acute or chronic stress [43].

US can accurately answer the questions a surgeon has concerning the rotator cuff because it can detect full-thickness rotator cuff tears with excellent sensitivity and specificity, and it is just as accurate as MRI in determining the size of a tear and detecting fatty infiltration in muscles [44].

US was used to find that hemiplegic shoulders had a higher percentage of tendonitis than unaffected shoulders and that soft-tissue damage and lesions were more common in the biceps and supraspinatus tendons [45]. Lastly, in a study by Daghir et al. [46], US was used to show that shoulder abduction caused subacromial-subdeltoid bursa (SASD bursa), and the researchers interpreted the data as evidence of the bursa's painful impingement. However, the US could have data artifacts requiring filtering and smoothing [47].

US exhibits certain drawbacks, such as the limited tissue penetration ability of US waves, and it is deemed operator-dependent, necessitating highly experienced examiners proficient in the technique due to its reliance on operator-centered factors for producing reliable results [42], [48].

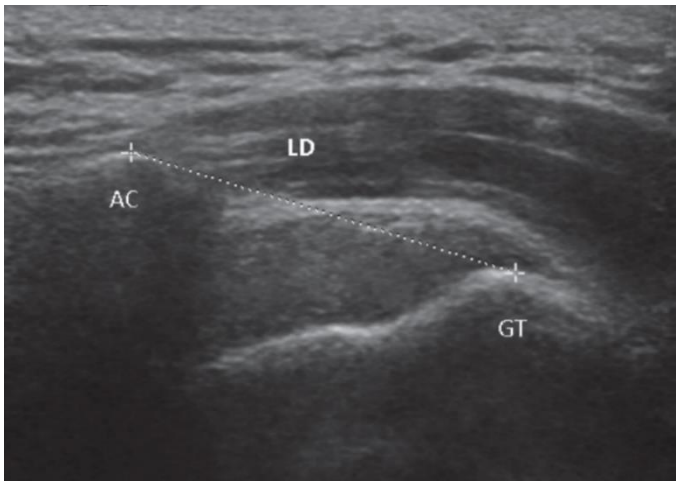

Figure 9: Ultrasound measurement of shoulder subluxation:
the lateral distance (LD) was measured from the lateral border
of the acromion to the greater tuberosity of the humerus.
AC: acromion, GT: greater tuberosity [45].

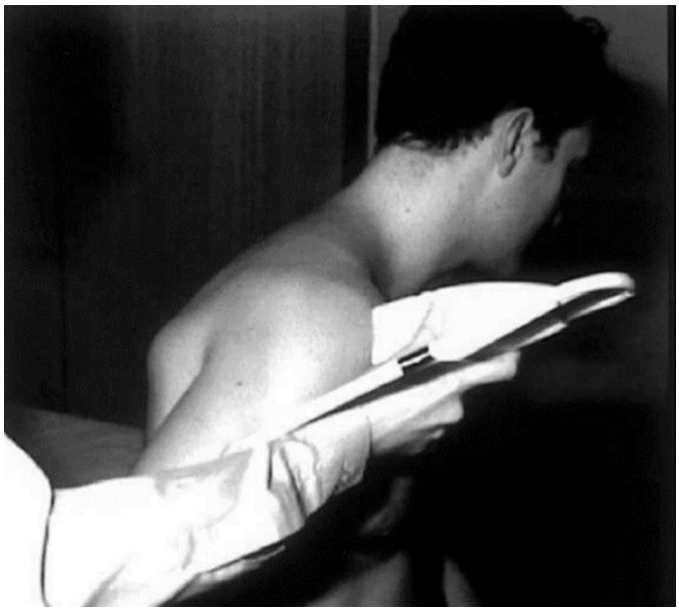

Figure 10: Ultrasound used to examine a shoulder injury [49].

2.4.3: Intracortical Bone Pins

Another technique to track musculoskeletal motion accurately is bone pins, considered another gold standard mechanism to track bones (Figure 11). This technique involves surgically implanting intracortical bone pins into bone landmarks before data collection and removing them after testing. The relationship between the bones, pins, and markers placed on the pins can be established using radiographic images of the bone.

Bone pins used in a study by McClure et al. [50] employed a direct technique to describe three-dimensional scapular motion patterns during dynamic shoulder movements. Two 1.6 mm bone pins were inserted into the spine and the scapula to assess active scapular mobility. The study provided an understanding of normal scapular motion, which can help identify aberrant motion linked with shoulder diseases. However, the study utilized a small sample of young, asymptomatic adults because it was invasive,

and most subjects preferred having their non-dominant shoulder girdle evaluated. Furthermore, the motions studied were conducted at relatively slow speeds (between 30° and 50° per second), but functional tasks performed at high velocity induced distinct motion patterns.

The primary drawback of this technique is that it is an inherently invasive procedure requiring surgical implantation, which causes morbidity, and the surgery and the injury it causes may also affect shoulder motor function. For clinical inference, using pins includes local anesthesia during insertion and interference with the motion of muscles, tendons, or ligaments caused by pins. Such impacts on foot motions have already been studied by Maiwald et al. [51]; following the insertion of pins, subjects generally had fewer striking foot interactions as measured by the ground reaction force. They claimed that implanting pins did not consistently alter gait patterns. However, it may behave differently from the foot due to the shoulder's differing anatomy and mechanical complexity. As we can see in Hajizadeh et al.'s study [52], the effect of bone pins may alter the motion of the GH or ST joints by changing the coordination between those joints before and after pin implantation. The study showed that when shoulder bone pins were inserted, HT elevation and internal rotation ROMs changed during abduction, mainly when the arm was at its highest elevation.

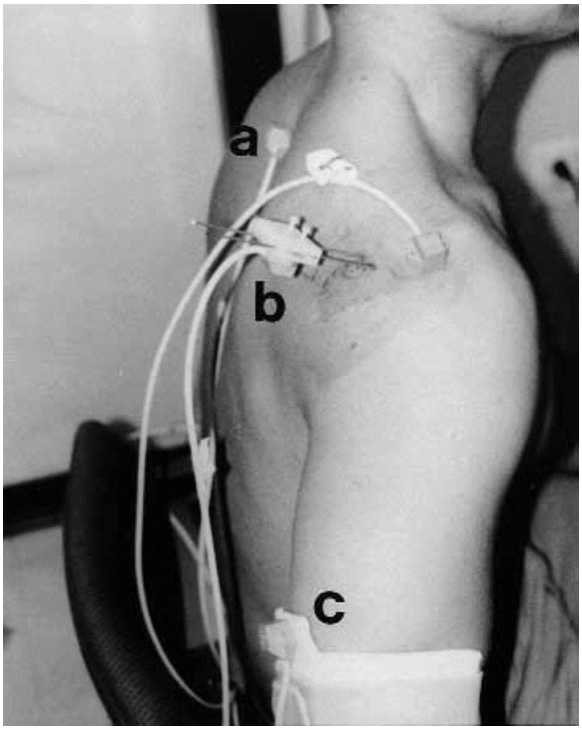

Figure 11: Subject with motion sensors attached:
Thoracic sensor (a), scapular sensor attached to bone pins
(via plastic guide) inserted into the scapula (b) and humeral
The sensor was mounted on a custom cuff
applied to the distal humerus (c) [50].

2.4.4: Biplane Fluoroscopy

Biplane fluoroscopy, also known as dual plane fluoroscopy, 3D radiography, and stereo radiography, can calculate the translation and rotation of bone with submillimeter accuracy and precision within the living body. Consisting of two X-ray sources (Figure 12) and corresponding detector panels positioned in a quasi-orthogonal arrangement, this gold standard of noninvasive *in vivo* quantification of bone motion uses X-ray tubes to create beams that pass across the joint of interest, enter image intensifiers, and create x-ray videos [53].

Biplanar fluoroscopy has various applications in orthopedics, bioengineering, and sports medicine since it can quantify 6DOF joint motions with precision during static and dynamic movements; therefore, the accuracy of biplanar fluoroscopic measurements of joint mobility aids in assessing joint function and improving implant design [54], [55].

A study by Bey et al. [56] investigated the precision of a new model-based tracking technique for quantifying three-dimensional GH joint kinematics from biplane radiography images. The study used tantalum beads implanted into the humerus and scapula of both shoulders from three cadaver specimens and captured biplane radiography pictures of the shoulder while manually moving each specimen's arm. The dynamic measuring precision of the study's technique was (0.130±0.058 mm and 0.077±0.033 mm on the X-axis, 0.123±0.054 mm, and 0.095±0.043 mm on the Y-axis, and 0.060±0.014 mm and 0.067±0.022 mm in the Z-axis on the fixed laboratory coordinate system) for the scapula and humerus, respectively. Overall dynamic accuracy demonstrated that RMS error in any direction for the scapula was less than 0.385 mm and less than 0.374 mm for the humerus. These errors equate to scapula rotational inaccuracies of around 0.25° and humerus rotational inaccuracies of approximately 0.47°. The model-based technique outperformed all previously reported noninvasive methods for monitoring *in vivo* GH joint mobility. Later, in Bey et al. [57], more advanced biplane x-ray equipment was employed to offer reliable *in vivo* measurements of subacromial space width during shoulder elevation. Between three and four months after rotator cuff repair, these measurements were taken in patients with repaired and asymptomatic contralateral shoulders. The study's findings showed that compared to the contralateral

shoulder, the reconstructed shoulder's humerus is positioned more cranially on the glenoid. This technique offered even more precise 3D measurements of *in vivo* subacromial space width during shoulder mobility than other methods.

Another study by Giphart et al. [58] measured GH three-dimensional translations and rotations during abduction, scaption, and forward flexion for 13 healthy subjects. The humerus and scapula were located and oriented in three dimensions in each frame using bone geometries from computed CT images. The study confirmed that changes in the plane of arm elevation had a wide range of effects on GH kinematics, including in GH translations, GH elevation, and scapulohumeral rhythm. In addition, Giphart's study showed that biplane fluoroscopy has emerged as a highly accurate and precise method to measure *in vivo* three-dimensional kinematics within fractions of a millimeter. 3D/2D registration techniques with biplane fluoroscopic images used by Kijima et al.[59] to compare the 3D scapular and GH kinematics during scapular-plane abduction between symptomatic rotator cuff tears, asymptomatic rotator cuff tears, and healthy shoulders. The technique's accuracy was within 0.5mm for in-plane translation, 1.3mm for out-of-plane translation, and 0.8mm during in-plane rotation and out-of-plane abduction.

In another study by Baumer et al. [60], the 3D positions of the humerus, scapula, and ribs were recreated using model-based tracking and measured with biplane fluoroscopy to find HT, GH, and scapulothoracic (ST) joint positions and kinematics and found to be accurate within ±0.4 mm and 0.5°. Lastly, Fluoroscopy exposes patients to lower levels of ionizing radiation than CT, with a typical exam session often lasting less than one

minute, and the average dosage for regular fluoroscopy is around 10–50 mGy/min in a conventional fluoroscopy suite setup [61].

Using fluoroscopy in research has a few limitations, including radiation exposure to the participant, which makes follow-up sessions or repeated trials difficult. A study by Giphart et al.[62] discussed the drawbacks of fluoroscopy radiation, the study recommended using the lowest amount of radiation to allow for sufficient image quality for motion tracking. The study also suggested that MRI might be utilized to get bone geometry to limit radiation exposure further. Additionally, while fluoroscopy provides a focused and functional examination of a particular region of interest, more than the 3D imaging volume is needed to visualize other segments; for example, the torso position and orientation are required to measure the kinematics of the scapulothoracic and HT joints, but they may not be visible inside the fluoroscopy frame [63]. Therefore, in addition to biplanar fluoroscopy, it may be necessary to use an external surface-based tracking system synced with the radiographic method.

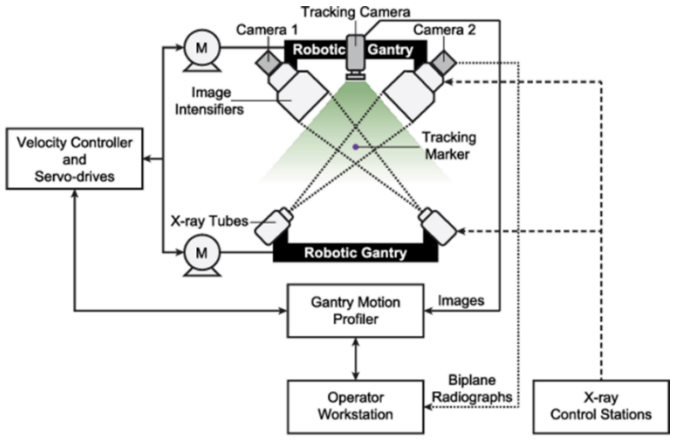

Figure 12: Schematic diagram showing the interactions between the various components of the X-imaging system [64].

2.4.5: Motion Capture

Biomechanics studies have extensively employed MOCAP systems to investigate lower and upper-extremity kinematics[65]–[67]. Kinematic analysis, a widely adopted approach, is crucial in quantifying human movement for research and clinical biomechanics purposes. Particularly in clinical applications, the noninvasive assessment of shoulder motion during dynamic activities is essential. MOCAP systems utilize diverse technologies, including infrared cameras, electromagnetic sensors, IMUs, and force plates, to track *in vivo* dynamic movements. These systems provide 3D spatial coordinates (X, Y, Z) for markers placed on body segments, allowing the calculation of velocities, moments, and accelerations for joint kinematics and kinetics. The applications of MOCAP span from sports performance analysis to rehabilitation monitoring, offering objective metrics such as range of motion (ROM), muscle activation, and compensatory movements for tailored therapy plans and improved recovery outcomes [68].

Despite the valuable kinematic data MOCAP systems provide, processing data from marker-based systems can be time-consuming. However, the benefits outweigh this challenge. Skin-mounted markers, affixed using adhesive to bony landmarks, avoid safety concerns associated with invasive implantation.

Early methods for measuring *in vivo* shoulder motion relied on electromagnetic sensors and video analysis of skin markers, yielding varying results in reported glenohumeral joint mobility. Notably, the accuracy of standard methods for shoulder motion detection remains untested for *in vivo* applications. Inaccuracies stemming from soft tissue artifacts were identified due to skin-affixed markers not moving in concert

with underlying bone [13]. Efforts to address MOCAP limitations led to the proposal of metrics for describing soft tissue artifacts and the provision of standardized datasets for artifact data exchange; understanding the uncertainties introduced by the skin and soft tissue movement relative to bones is crucial in interpreting the results [69].

A study by Carse et al.[70] found a maximum difference of 2.6% between motion markers tracked by the Vicon system compared to those followed by the OptiTrack system with the same number of cameras. Another study by Merriaux et al. [71] investigated the accuracy of the Vicon Motion Systems optoelectronic system. The system demonstrated its ability to track markers with mean absolute marker tracking errors of 0.15 mm during static trials and 0.2 mm with corresponding angle errors of 0.3°.

Comparative studies have evaluated the accuracy of MOCAP systems against other technologies. These studies demonstrated differences in marker tracking errors, with Vicon and OptiTrack systems showing minor discrepancies. The Vicon optical marker-based system was selected as the reference system based on its popularity and common usage in literature [72]–[74]. Between low- and high-speed testing, the Vicon positioning error was less than 2 mm, with better positional variability for static trials.

Research comparing marker-based optical motion capture with other methods has revealed position and rotation errors in joint kinematics. These deviations become pronounced after contact, underscoring the need for improved accuracy.

A study by Miranda et al.[75] compared marker-based optical motion capture (OMC) against biplanar video radiography during a jump-cut maneuver, revealing joint center position errors across the body as high as 30 mm, with averages between 9 and 19 mm

and joint rotation errors across the body as high as 14◦, with standards between 2.2◦ and 5.5◦. Miranda concluded that the OMC and biplanar video radiography knee joint kinematics were in the best agreement before landing. Kinematic deviations between the two techniques increased significantly after contact.

A study by Kessler et al. [76] compared to bi-planar video radiography errors for markers placed over shank soft tissue were 5-7 mm, while markers placed over bony landmarks on foot were 3-5 mm during walking and running trails. Root mean square (RMS) differences in marker positions and joint angles and a linear fit method (LFM) were used to compare the outputs of both approaches. When comparing the two systems, sagittal plane angles were in good agreement. When examining the ankle, there was moderate agreement between the systems in the frontal plane and a weak to moderate correlation for the transverse plane.

A study by Hume et al. [77] compared knee kinematics measured with a marker-based motion capture system to kinematics acquired with high-speed stereo radiography (HSSR) and described the accuracy of marker-based motion to improve the interpretation of results from these methods. Hume concluded that the movement of the skin and soft tissues relative to the underlying bones introduced uncertainty in the marker positions concerning the body segments. Flexion-extension rotation was accurately measured in all tasks and models when knee kinematics were measured with marker-based motion capture. However, the kinematics predicted for the valgus varus DOF models showed poor accuracy compared to HSSR-based measurements. The marker-based model predicted large amounts of translation in the anterior-posterior (AP) and superior-inferior

(SI) directions for the knee extension task, resulting in a maximum mean AP error of 20.9 mm at 100° of knee flexion and a maximum mean SI error of 19.7 mm at 105° of knee flexion. The maximum mean error in the medial-lateral (ML) DOF from full extension through 40° of knee flexion was 3.4 mm and then increased to 7.0 mm at 105°.

Although highly promising for various applications, motion capture technology still faces challenges in accuracy and precision due to marker placement on the skin rather than directly on the bone. Its potential benefits in long-term care and emergency medical care are evident. However, further developments are required to optimize its utility in real-world scenarios. Motion capture technology is vital in biomechanics research and clinical applications. While it offers valuable insights, efforts to address accuracy concerns and enhance precision are ongoing to unlock its full potential. That is the purpose of this study.

Chapter Three: Methods

This chapter explains the methodology employed in this study, integrating both systems, MOCAP and fluoroscopy. It begins with subject recruitment, then data collection and processing, which involves model creation and establishing coordinate systems. The chapter concludes with kinematics calculation and data analysis.

3.1: Subject Recruitment

The study included five healthy adults (3M, 2F; age: 30.8±5.4 yrs; BMI: 21.9±2.7 kg/m2) with no known shoulder pathology or limitation of ROM. Exclusion criteria included a history of shoulder injury or surgery and MRI contraindications. All subjects were right-arm dominant. However, both arms were evaluated. Before subject recruitment, the University of Denver Institutional Review Board (IRB) granted ethical approval for this study (IRB # 1066258), and all participants provided written informed consent before the start of the data collection.

3.2: Laboratory Set-up

The lab had a 10-camera video MOCAP system (Vicon, Oxford, UK). Eight cameras were mounted to the wall and ceiling surrounding the subject, one was mounted on tripods behind the subject, and one was suspended from the fluoroscopy gantry. The cameras were set to sample data at 100 Hz; the three-dimensional space was

Calibrated using the Vicon passive calibration wand across the relevant view volume at the beginning of a data collection day.

The Vicon coordinate system's origin was on the laboratory floor at the corner of the force plate. The laboratory coordinate system was defined with the Z-axis in the vertical direction, the Y-axis pointing laterally to the subject's right, and the X-axis in the posterior direction (Figure 13).

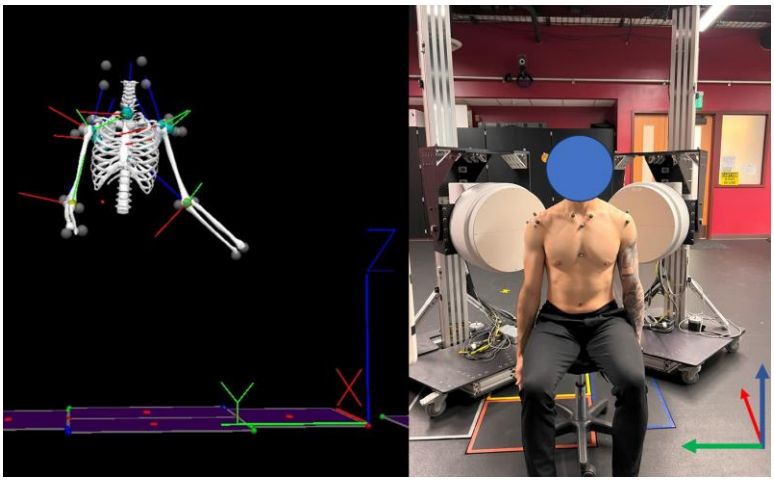

Figure 13: Vicon/V3D lab Coordinate System.

3.3: Motion Capture Data Collection

A total of 30 retroreflective markers (13mm diameter) were placed over prominent, visible upper extremity bony features, and each marker's 3D position in space was detected with the Vicon infrared cameras.

3.3.1: Marker Set

Once the subject was ready, the research team applied reflective markers to the subject. A full-upper body marker set was created for this study. Markers were placed on bony landmarks where subcutaneous tissue is thin and relatively well anchored to the underlying skeleton, limiting marker movement artifacts [78]. Markers were placed on both left and right upper extremities and trunk following ISB recommendations with modification as demonstrated (Figure 14). A minimum of three markers identified each segment.

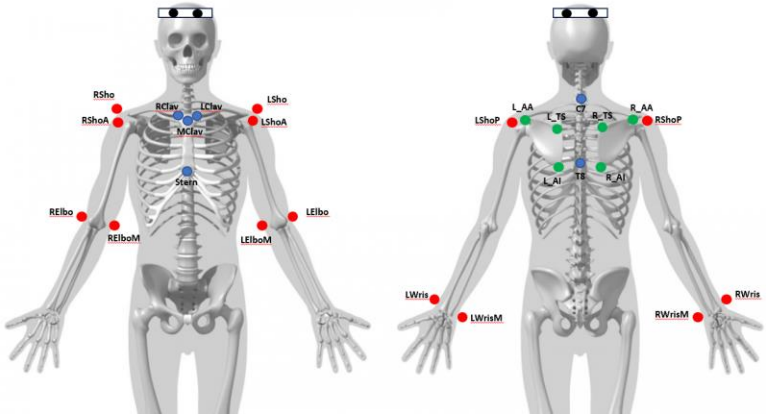

Figure 14: Marker set bony landmark location.
(anterior and posterior views).

Table 1: Motion capture marker set.

Marker Group	# of Markers	Marker Names	Marker Location
Trunk	6	C7	Spinous Process of C7.
		T8	Spinous Process of T8.
		Clav	Suprasternal Notch.
		Rclav	Top of the right Sternal Medial end of the clavicle bone.
		Lclav	Top of the left Sternal Medial end of the clavicle bone.
		Stern	Xiphoid Process.
Scapula	12	R_AA	Angulus Acromialis of the right scapula.
		L_AA	Angulus Acromialis of the left scapula.
		R_ST	Trigonum Spinae Scapulae of the right scapula.
		L_ST	Trigonum Spinae Scapulae of the left scapula.
		R_AI	Inferior Angles of right Scapula.
		L_AI	Inferior Angles of left Scapula.
		RSho	Right Acromion, the part that covers the humerus's head.
		LSho	Left Acromion, the part that covers the humerus's head.
		RShoA	Lesser Tubercle of the right humerus.
		LShoA	Lesser Tubercle of the left humerus.
		RShoP	Greater Tubercle of the right humerus.
		LShoP	Greater Tubercle of the left humerus.
Humerus	8	RElbo	Lateral Epicondyle of right humerus
		LElbo	Lateral Epicondyle of the left humerus.
		RElboM	Medial Epicondyle of the right humerus.
		LElboM	Medial Epicondyle of the left humerus.
		RWris	Radius-Styloid Process of the right wrist.
		LWris	Radius-Styloid Process of the left wrist.
		RWrisM	Ulna-Styloid Process of the right wrist.
		LWrisM	Ulna-Styloid Process of the right wrist.

3.4: Motion Trials Captured

Static and dynamic calibration trials were collected for both arms as follows:

Static Calibration Trials:

1. Neutral pose arm relaxed at side.
2. Neutral T-pose with arms abducted 90°.

Dynamic Calibration Trials:

1. Circumduction low.
2. Circumduction high.

Dynamic Motion Trials:

1. Abduction with weight.
2. Abduction without weight.
3. Flexion.
4. Internal and external rotation with the arm at the side.
5. Internal and external rotation with the arm adducted to 90°.

Synchronized motion capture and fluoroscopic image data were collected for the dynamic motion trials as the arm moved through the full range of motion. Subjects were asked to sit in a chair to perform the movement in the volume between the two X-ray sources and the two image intensifiers. Study participants performed each arm movement while seated with straight backs. Data was collected for approximately two seconds while the subject remained still for static trials in an anatomical position. The static calibration file was used in Visual3D (C-Motion, Inc., Germantown, MD) software (V3D) to define the kinematic model, and the dynamic calibration was used in the auto-labeling pipeline in Vicon Nexus. While the participants performed each activity, images were taken of

them simultaneously using the Vicon camera and bi-planar fluoroscopy. On a different date, CT images were taken for the participants for each shoulder.

3.5: Biplanar Fluoroscopy Data Collection

The movement of the upper extremity bones was collected simultaneously with the biplanar fluoroscopy (Figures 15, 16, 17, and 18). The fluoroscopy view volume was calibrated as in the previous research conducted by Kefala et al. [54]. The main components of bi-planar fluoroscopy are X-ray sources, X-ray detectors, image intensifiers, and two cameras [54]. Shoulder kinematics were measured using a high-speed stereo radiography (HSSR) imaging system comprising two 40 cm image intensifiers connected to high-speed, high-definition digital cameras (70° relative angle). 167 mm separated the source image from the receptor, and imaging intensities between 70 and 85 kV and 80 mA were used. A pulse width of 1250 s was used to acquire sampling rates at 25 Hz. The first camera recorded motions from an anterior view, and the second recorded from an anterior-medial view [79].

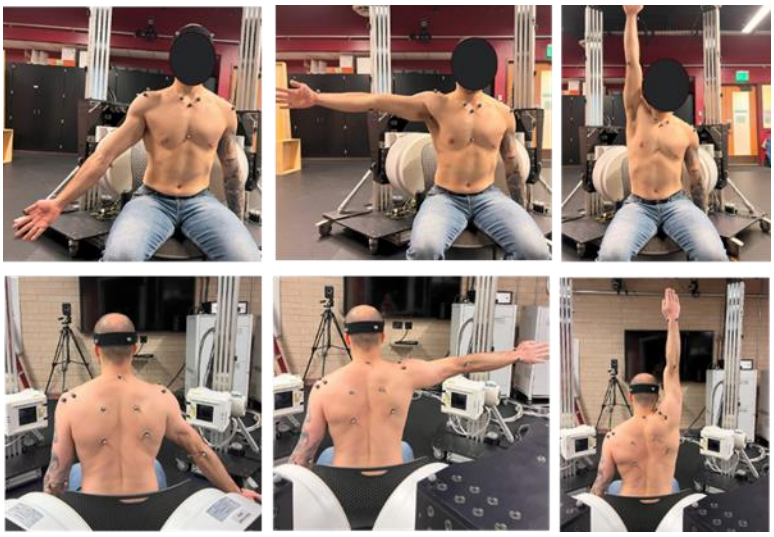

Figure 15: Anterior and posterior views of a subject performing abduction movement, illustrating the transition from the natural position through 90° of abduction to maximum abduction.

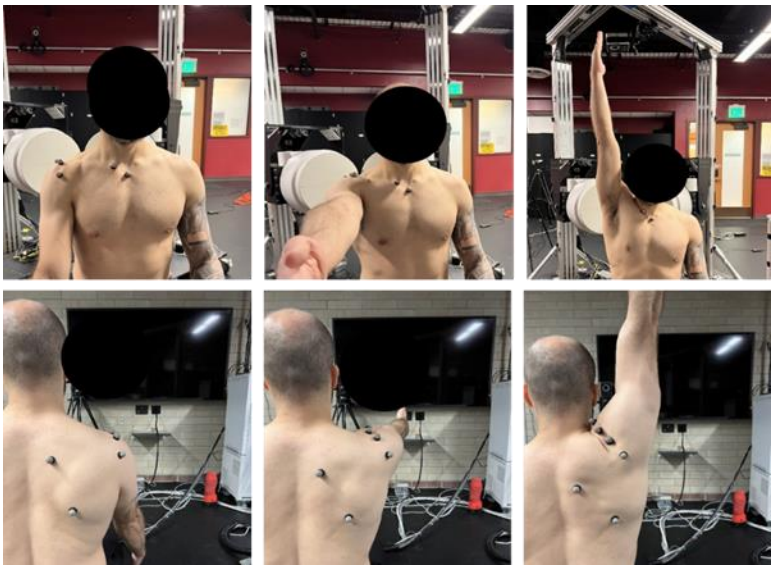

Figure 16: Anterior and posterior views of a subject performing flexion movement, illustrating the transition from the natural position through 90° of flexion to maximum flexion.

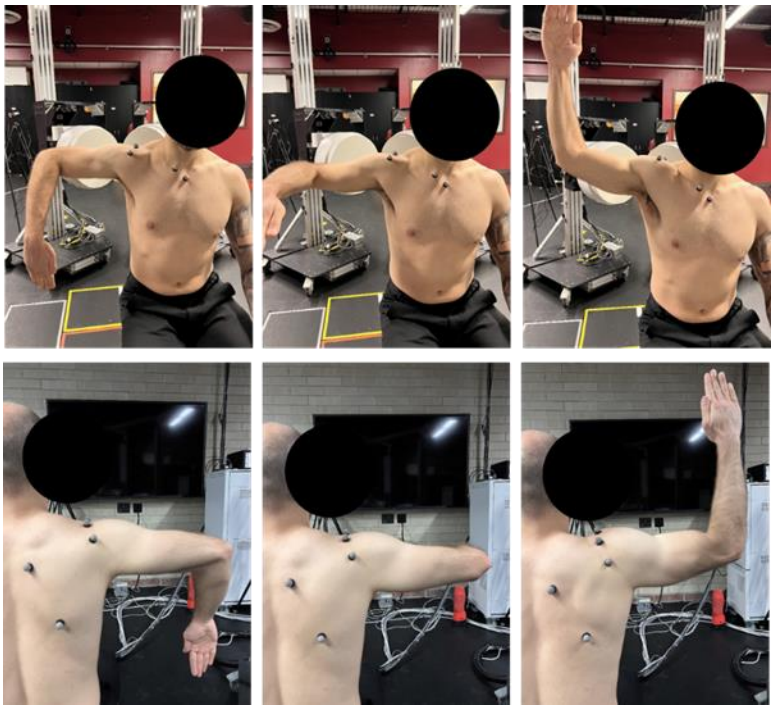

Figure 17: Anterior and posterior views of a subject performing external rotation at 90° movement, illustrating the transition from the negative 90° to maximum external rotation.

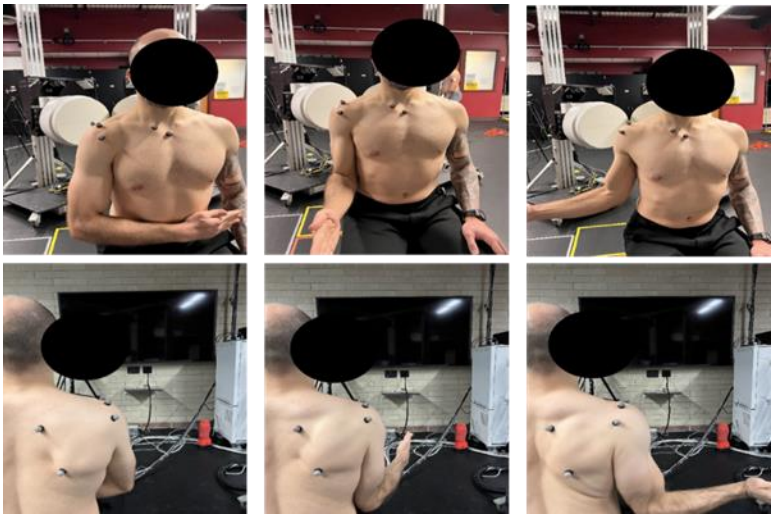

Figure 18: Anterior and posterior views of a subject performing external rotation to side movement, illustrating the transition from the natural position through 90° to maximum external rotation.

3.6: CT Scans Data Collection.

The bone models of each subject's scapulae, humeri, and trunk were obtained from a custom CT protocol designed. The CT scan protocol involves a preliminary localization procedure followed by a comprehensive axial scan focused on the shoulder region. Before the scan, participants were directed to eliminate any mobile metallic prosthetic implants, accessories, or fastenings that could impede the imaging process within the designated scan area. Detailed instructions were provided to ensure that participants-maintained immobility throughout the procedure. During the positioning phase, participants were supine, with their upper limbs resting adjacent to the body and the shoulder positioned in a neutral position. Notably, both the dominant and non-dominant sides of the body were subjected to scanning, encompassing anatomical structures such as the humerus, scapula, and approximately one-half of the trunk. The CT scanner generated images with a resolution of 512x512 with 0.625 mm axial slice thickness.

3.7: Motion Capture Data Processing

The MOCAP data was processed using Vicon Nexus software (Vicon Motion Systems v1.7.2, Denver, CO). Markers were labeled, and gaps in the marker trajectories were filled using pattern filling. Patterns filling utilized another marker as a reference, ensuring that the trajectories originated from markers attached to the same segment under the assumption that the segment was rigid and, thus, there would be little relative movement between the two markers. Once all markers were labeled and gaps filled, the marker trajectories were exported to be analyzed using V3D software.

In V3D, a model was created for each subject using their static calibration trial in an anatomical position with their hand resting to the side. The static trial was loaded into the subject's workspace, the model template created for this study was applied to the trial, and their height and weight were set based on measurements recorded during the collection.

3.8: Visual 3D Model

All dynamic trials were chosen for data analysis. The motion of each subject was analyzed with a seven-segment, 6DOF model, including the trunk, left upper arm, right upper arm, left forearm, right forearm, left scapula, and right scapula. In addition to the tracked marker location, multiple virtual landmarks were created for the model.

3.8.1: Model Virtual Landmarks

Table 2: Creation of virtual landmarks utilizing V3D for dominant and non-dominant Sides (***** denotes landmarks employed for COR, discussed in the following section).

Model Virtual Landmarks	
Acromion	*****Moving 4cm distally in the global coordinate system from the center of the acromion marker.
Shoulder Centerpoint	*****Starting from the acromion marker and ending with the greater and lesser markers. The landmark is created by moving distally 40%, medially 40%, and anteriorly 25%, offset by percent function in V3D.
Shoulder Midpoint	*****Midpoint between the greater and lesser humeral head markers.
Elbow Joint Center	Midpoint between the EM and EL markers.
Middle Upper Trunk	Midpoint between C7 vertebra and sternal notch markers.
Middle Lower Trunk	Midpoint between T8 vertebra and xiphoid markers.
Scapulae Lateral Border	Midpoint between Trigonum Spinae (TS) and Angulus Inferior (AI) markers.
Scapulae	Midpoint between the virtual acromion marker and the scapula lateral border virtual landmark.

3.8.2: V3D Model Local Coordinate System

A local coordinate system was added to each segment (Figure 19).

Trunk/Thorax:

Proximal Endpoint (Origin): Middle upper trunk virtual landmark

Distal Endpoint: Middle lower trunk virtual landmark

Z-Axis: Vector from the distal to the proximal endpoint of the segment.

X-Axis: The vector perpendicular to the plane formed by the sternal notch, C7 vertebra, and the midpoint between the xiphoid process and T8 vertebra. The positive X-axis points towards the right side of the subject.

Y-Axis: The vector formed by the cross product of the X-axis and Z-axis pointing anteriorly.

Upper Arm:

Proximal Endpoint (Origin): The specific virtual marker (Acromion, Midpoint, or Centerpoint).

Distal Endpoint: Elbow joint center.

Z-Axis: Vector from the distal to the proximal endpoint of the segment.

Y-Axis: Defined as the vector normal to the plane formed by the shoulder joint center, the medial and lateral elbow markers, directed anteriorly in the resting arm position.

X-Axis: Axis formed by the cross product of the Y- and Z-axes.

Forearm:

Proximal Endpoint (Origin): Elbow joint center.

Distal Endpoint: Wrist markers, radius, and ulnar styloid process.

Z-Axis: Vector from the distal to proximal endpoints of the segment.

Y-Axis: Defined as the vector normal to the plane formed by the elbow joint center and the wrist markers, directed anteriorly in the resting arm position.

X-Axis: Axis formed by the cross product of the Y- and Z-axes.

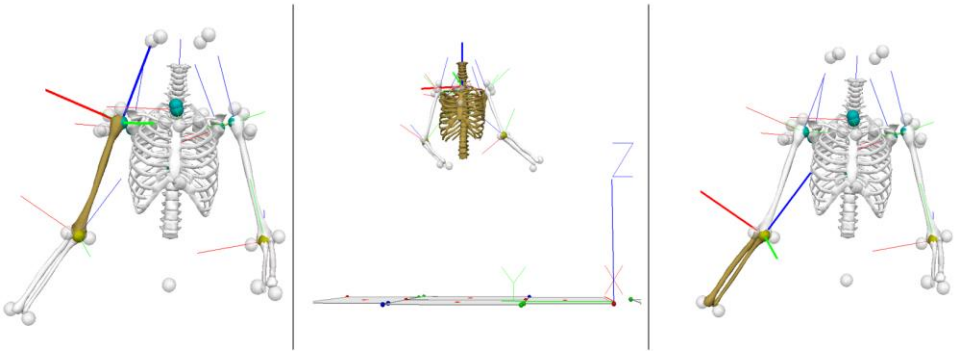

Figure 19: LCS added to the model segments
(upper arm, trunk, forearm).

Scapula:

Proximal Endpoint (Origin): The virtual marker for the left and right scapulae.

Distal Endpoint: The virtual marker created for the left and right COR joints.

Y-Axis: Vector from the distal to the proximal endpoints of the segment.

Z-Axis: Defined as the vector normal to the plane formed by the proximal endpoints of the segment superiorly to the segment.

X-Axis: Axis formed by the cross product of the Y- and Z-axes (Figure 20).

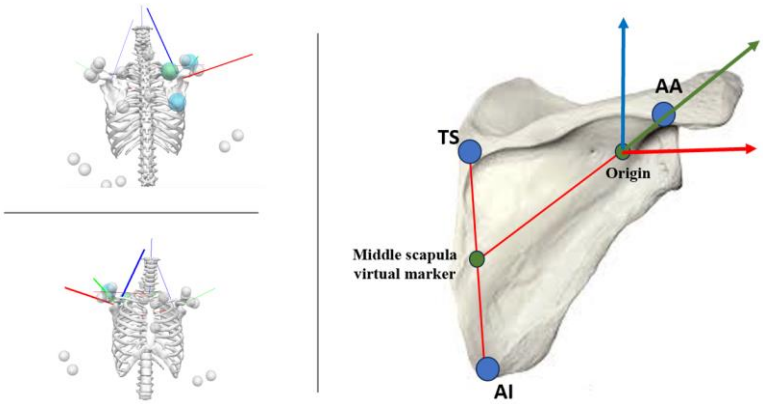

Figure 20: LCS added to the scapula segment
using V3D software.

The marker trajectories were filtered with a fourth-order, zero-lag, Butterworth filter with a cut-off frequency of 6 Hz. According to Schreven et al. [80], 4 to 8 Hz cut-off frequencies are commonly utilized in filtering movement data; the study stated that the experimenter must select an acceptable filtering process and decide on a cut-off frequency for this procedure. A high cut-off frequency removes only a small amount of noise, whereas a low cut-off frequency introduces artifacts in the trajectory [81].

High-frequency noise in the collected data during post-processing is one of the primary issues while using MOCAP systems to collect data; low-pass digital filters are frequently employed to remove noise from signals [82].[83] After filtering the data, a pipeline was created to export the location of the specific landmark (X, Y, Z) location in the VCS.

3.9: CT Processing

A 3D bone model for each bone was created from the CT images using ScanIP software (Simpleware Synopsys, Mountain View, CA, USA). The CT images for ten humeri, ten scapulae, and five trunks were separated from the surrounding tissue using a specific threshold that matched the bone density (Figures 21, 22, and 23). The ScanIP filtering and smoothing tool was used to improve the representation of the bone model surfaces to the natural bone. Later, an STL model of each bone was exported from ScanIP and re-meshed and smoothed in Hypermesh (Altair Hypermesh, MI, USA). In Hypermesh, landmarks were identified on the bones to add coordinate systems for each of the humeri, scapulae, and trunk following the ISB recommendations (Figure 24).

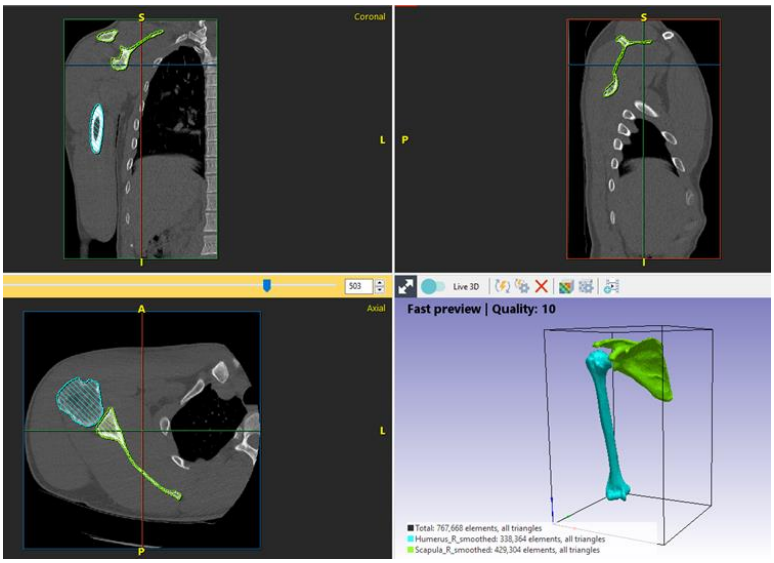

Figure 21: Segmented humerus and scapula
using Simpleware scanIP

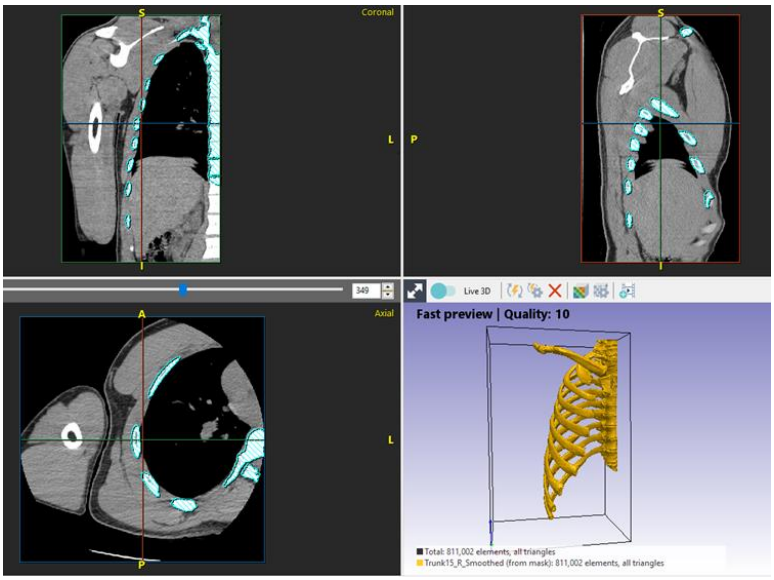

Figure 22: Segmented trunk
using Simpleware scanIP

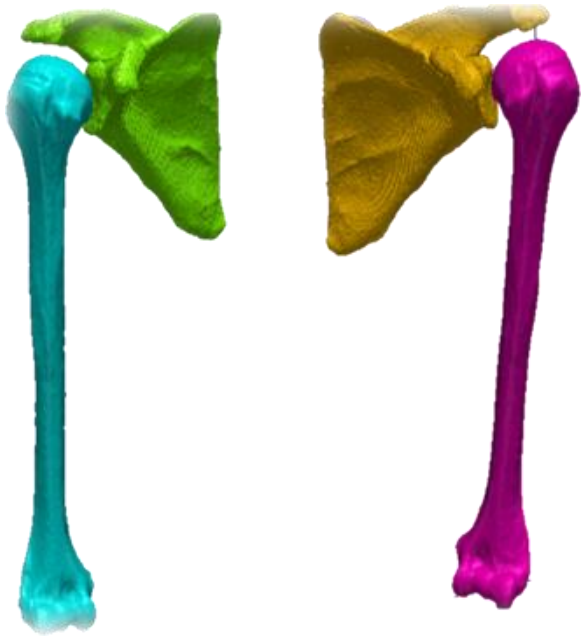

Figure 23: Segmented scapula and humerus for
dominant and non-dominant arms
of an exemplary subject

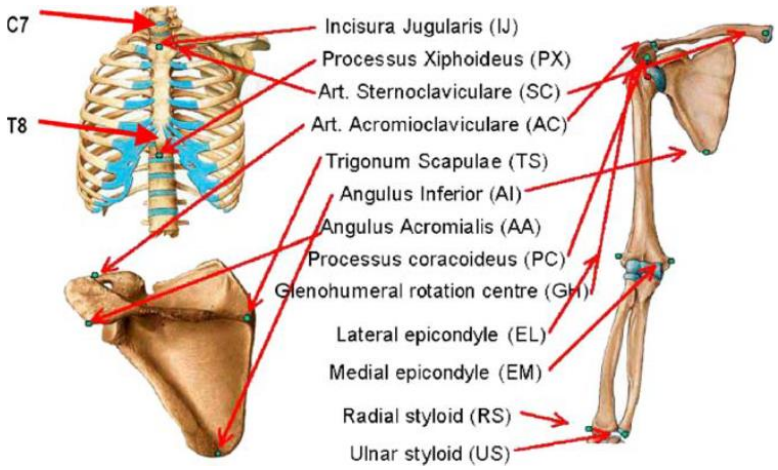

Figure 24: Bony landmarks and local coordinate systems of the thorax [10].

3.10: Coordinate Frame Assignment

Coordinate systems were created using the identified landmark positions and a custom MATLAB script (Version: 9.12.0 (R2022a), Natick, Massachusetts). STL files of the humerus and scapula bone models that represented the 3D surface of the bones were loaded into an Abaqus NSET file. The NEST file contains sets of specific nodes identified for each bone for alignment purposes. For the humerus, the nodes were (GH, EL, and EM); for the scapula, the nodes were (AA, AI, and ST); finally, for the trunk, the nodes were (IJ, PX, C7, and T8).

Humerus Coordinate System: The GH geometric center of the humeral head was used as the origin of the humeral coordinate system. A sphere was fitted to the humeral head to determine the origin of the humerus local coordinate system (HLCS). The line connecting GH and the midpoint between the most caudal point on the EL and the most caudal end on the EM is designated as the positive Y-axis, pointing superiorly. The

positive X-axis is created as the line perpendicular to the plane formed by EL, EM, and GH and points anteriorly. Lastly, the positive Z-axis points to the right of the humerus bone, perpendicular to the Y- and X-axes (Figure 25).

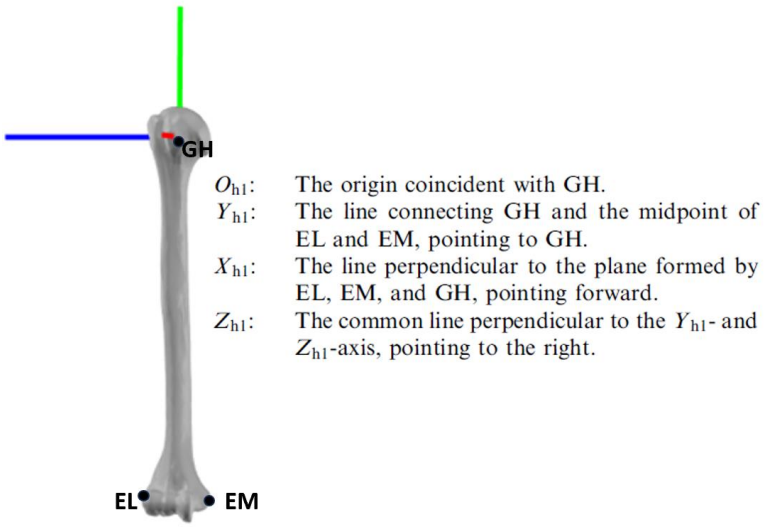

Figure 25: LCS added to the segmented humerus bone, using HyperMesh and MATLAB following the ISB recommendation, fitting a sphere method.

Scapula Coordinate System: The AA, the scapula's most laterodorsal point, was used as the origin for the scapula LCS. The Z-axis connects the TS to AA and points to the right in the same direction. The X-axis is the anterior perpendicular line to the plane created by AA, TS, and the AI points anteriorly. Finally, the Y-axis is a cranial line perpendicular to the X- and Z-axes, which points superiorly (Figure 26).

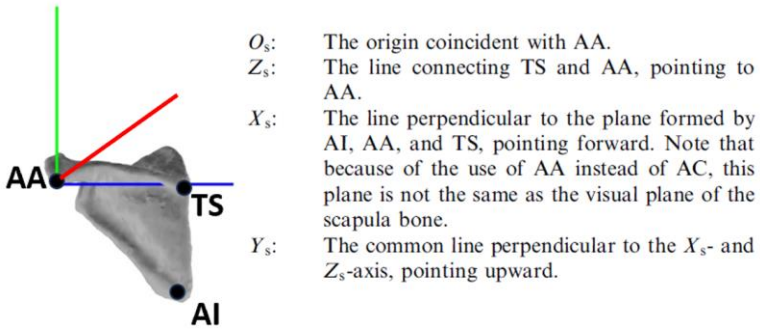

Figure 26: LCS added to the segmented scapula,
using HyperMesh and MATLAB
following the ISB recommendations.

Trunk Coordinate System: The ISB recommendation for a trunk coordinate system uses the T8 and C7 landmarks. However, the CT scan showed that each subject's entire rib cage/trunk geometry was not fully visible. Therefore, the origin of the trunk coordinate system was anterior to T1 in some subjects and anterior to T2 in others. The orientation of the trunk coordinate system was consistent over all the subjects as follows: Y-axis points superiorly, created in Hypermesh as a vector from the midpoint of T8 and the Xiphoid to the middle of C7 and the Suprasternal Notch. In instances where the visibility of the T8 vertebra was obscured, a vector was established by connecting the most distal observable vertebrae to the xiphoid process. The X-axis is created as a mutual perpendicular vector between the Y-axis and a vector from xiphoid to T8 pointed to the right. Lastly, the Z-axis points anteriorly, forming a Y cross X vector result (Figure 27).

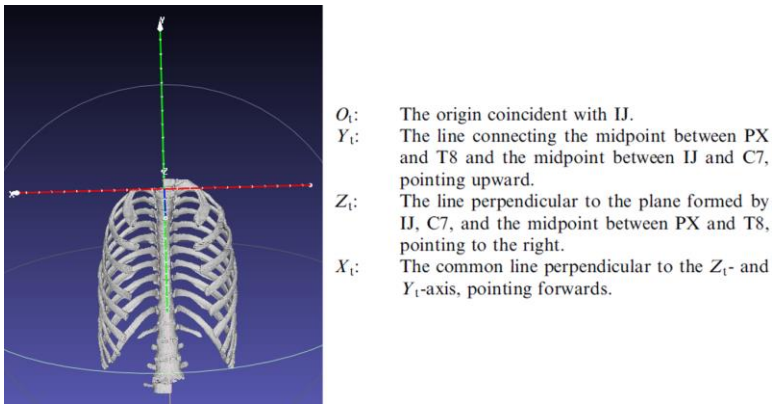

Figure 27: LCS added to the segmented trunk using HyperMesh following the ISB recommendation.

3.11: Fluoroscopy Data Processing

CT scans of each subject were used to create a 3D volumetric bone model of each bone whose silhouette was tracked with Dynamic Stereo X-ray (DSX) C-Motion, Inc. Aligned bones and TIFF stacks of the bones were used to track the individual fluoroscopy trials. An object file was created that defined the location of trials, images, TIFF stacks, bone surfaces, and calibration was created. Calibration and file setup were the same as those used in Andreassen et al. [83] (Figure 28). Fluoroscopy image sequences were used to calculate the 3D kinematics of the trunk, scapula, and humerus using a previously reported and verified model-based tracking technique[56], [84].

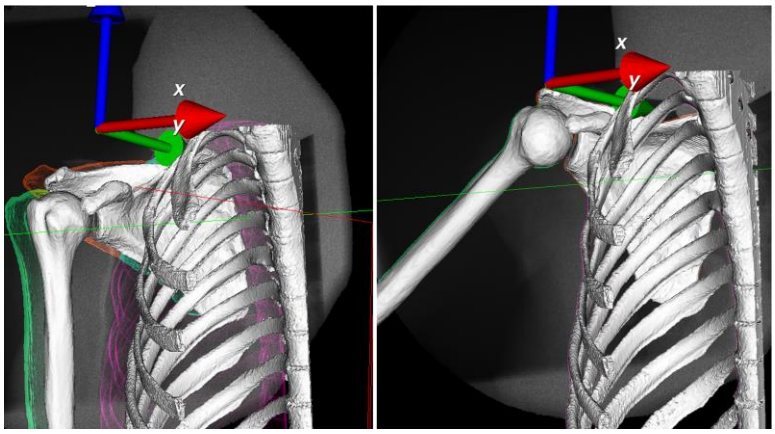

Figure 28: Bi-planar fluoroscopy DSX images,
anterior and lateral views.

Each bone was tracked separately for each motion frame (Figure 29), pose maps were saved, and transformation matrices were exported after determining the positions of each motion frame's trunk, scapula, and humerus. The transformation matrix represents the transformation of each bone from its local coordinate system to the global coordinate system.

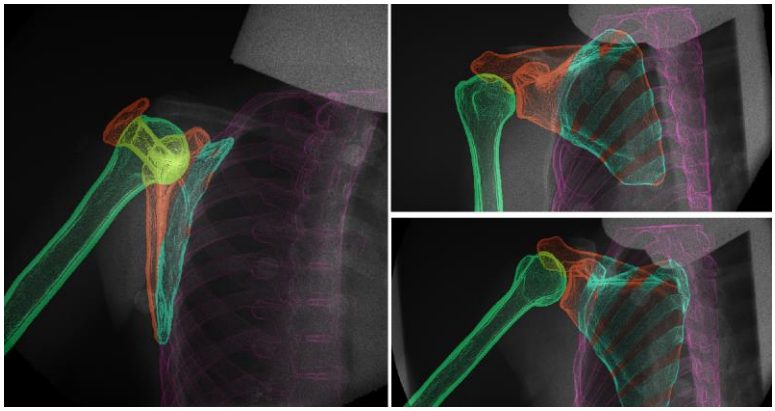

Figure 29: 3D views of the bones
(humerus, scapula, trunk) after being tracked in DSX.

To summarize the method, the diagram below shows the shoulder study workflow (Figure 30).

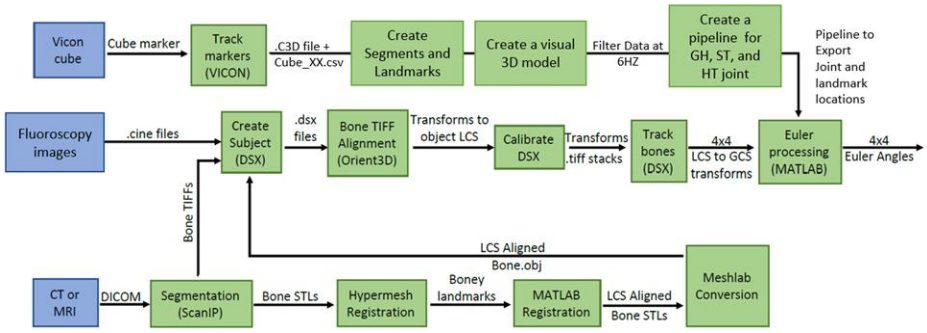

Figure 30: Shoulder study workflow.

3.12: Kinematics Calculation

3.12.1: Center of Rotation (COR) Calculation Using Landmark Locations

The location of the COR was estimated by creating three different virtual landmarks in V3D (C-Motion Inc.) based on skin-mounted markers, as shown in (Figures 31 and 32). The first method utilized a fixed displacement from the acromion marker **(Acromion method)**, a virtual landmark created by moving 4 cm in the inferior direction. Previous studies used the acromion bony landmark to estimate the COR and investigate shoulder kinematics [78], [85]–[88]. The second method for estimating COR is computed by creating a virtual landmark in the midpoint between the greater and lesser tubercle markers **(Midpoint method)** since those locations are considered the most prominent bony landmarks for the humerus head. The last and third methods created a center point between the acromion marker and the two tubercle markers **(Centerpoint method)**, a virtual landmark created starting from the acromion marker and ending with the greater

and lesser markers. The landmark is created by moving distally 40%, medially 40%, and anteriorly 25% from the acromion marker using the offset by percent function in V3D.

Figure 31: Location of the three COR generated using MOCAP system data on the subject.

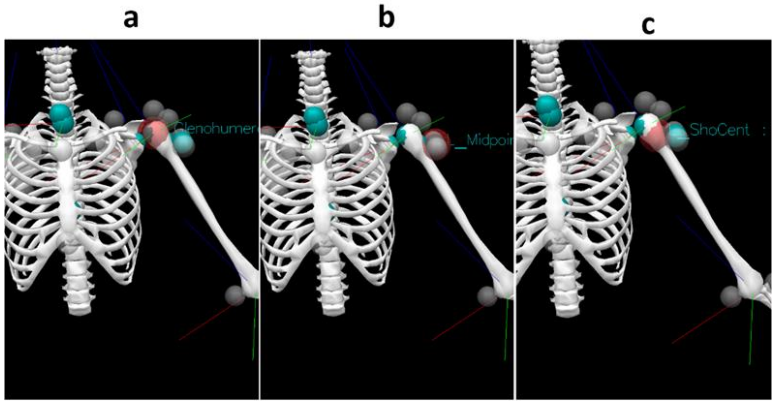

Figure 32: Location of the three virtual landmarks used to evaluate the center of the humeral head, (a) the Acromion landmark, (b) the Midpoint landmark, (c) the Centerpoint landmark.

Three virtual landmarks in V3D, established using skin-mounted markers, were subsequently compared to the COR determined via a sphere-fitting method (see Figure 33) using bi-plane fluoroscopy data.

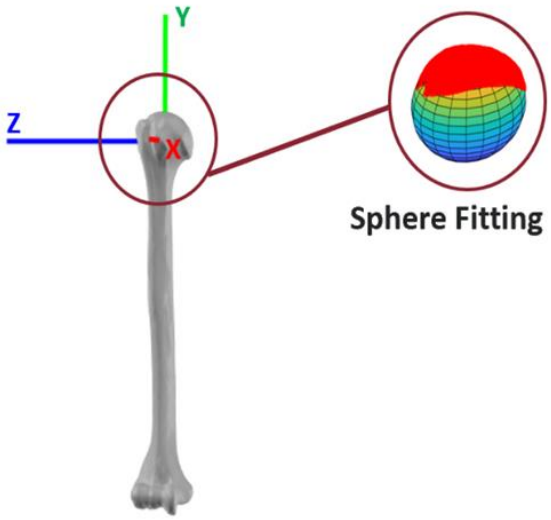

Figure 33: Glenohumeral center computation
by fitting a sphere on the humeral.

The acromion, the shoulder midpoint, and the shoulder centerpoint virtual landmarks were calculated using markers to evaluate their accuracy in locating the COR. The 3D position of each of those landmarks was filtered and exported in the Vicon coordinate system (VCS). The fluoroscopy and MOCAP data were synchronized for each movement. After aligning frames, MOCAP data was resampled from 100 Hz to 25 Hz to match the fluoroscopy sampling rate. The coordinate system for the landmark's location was converted from the VCS to the HLCS of the tracked humerus from the fluoroscopy for both arms for each subject. Transformation matrices were calculated to convert between the different coordinate systems, including the local coordinate systems of the humerus, scapula, and trunk, in both fluoroscope and Vicon coordinate systems.

3.12.2: Transformation Matrices

Data exported from DSX was uploaded into MATLAB. Three transformation matrices were extracted from the DSX data corresponding to the transformations of the humerus, scapula, and trunk with respect to the global coordinate system (GCS). After that, transformation matrices were created relating the humerus and scapula, humerus and VCS, scapula and trunk, scapula and VCS, humerus and trunk, and the trunk and VCS. The inverse of the humerus to VCS transformation matrix is computed to compute the VCS to HLCS transformation matrix. The position of the geometric humeral head center (0, 0, 0) was transformed to the VCS for each frame, and this data was used to match frames between the two systems and then for the resampling.

After matching frames and resampling frequency from 100 Hz to 25 Hz, the MOCAP data was converted to the HLCS. The MOCAP data is loaded into MATLAB from an Excel file and contains the (X, Y, Z) location of the landmarks representing the COR, including the acromion, midpoint, and centerpoint methods. After that, a matrix multiplication process was completed to generate a matrix containing transformed 3D points in HLCS in mm (Figure 34).

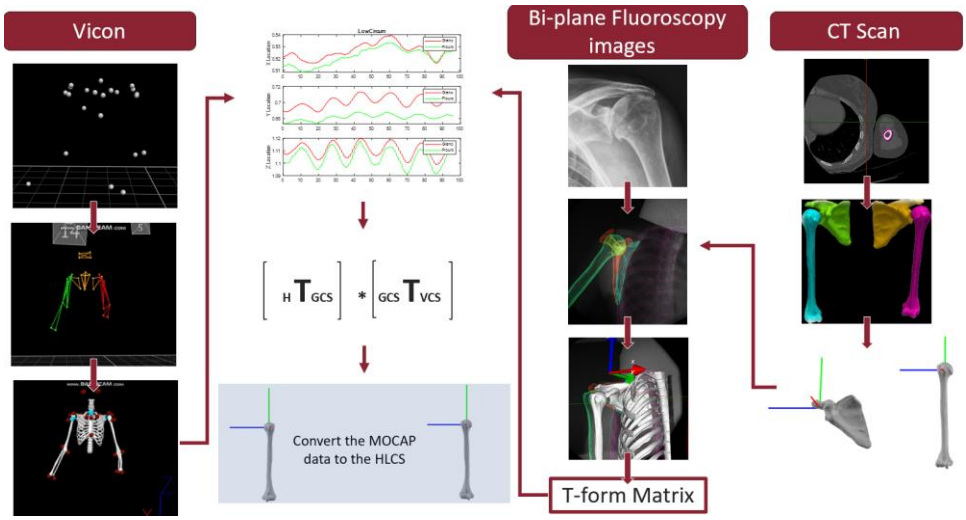

Figure 34: Diagram illustrating the process of converting MOCAP and fluoroscopy data to HLCS.

3.12.3: Range of Motion Calculation

A V3D pipeline was developed to calculate and export the data for the joint angles for three joints (GH, ST, and HT) and the humeral head's COR as a time function for each trial. The distal bone is transformed into the coordinate system of the proximal bone to present relative joint angles.

Twelve different Euler angle rotation sequences can be used in the joint angle calculations. The ISB recommends using Y-X-Y (Figure 35) to determine the elevation of the GH and HT joints, which can be found by rotating the intermediate coordinate system about the arm's X-axis and determining the rotation angle can be found by rotating the intermediate coordinate system about the arm's Y-axis. This study calculated GH and HT joint kinematics using a Y-X-Y Euler angle sequence of the humerus orientation relative to the scapula and trunk, respectively. ST joint kinematics were calculated using a Y-X-Z Euler angle sequence (Figure 36) of scapula orientation relative

to the trunk [56], [89]. For abduction and flexion, arm elevations were quantified as the second Euler rotations. For external rotation, with the forearm abducted at 90 degrees, and for external rotation at the side, arm rotations were quantified as the first Euler rotations. Joint ROM was quantified as the magnitude of the difference between the maximum and minimum joint angle in each plane during each trial.

$$Y_1X_2Y_3 = \begin{bmatrix} c_1c_3 - c_2s_1s_3 & s_1s_2 & c_1s_3 + c_2c_3s_1 \\ s_2s_3 & c_2 & -c_3s_2 \\ -c_3s_1 - c_1c_2s_3 & c_1s_2 & c_1c_2c_3 - s_1s_3 \end{bmatrix}$$

Figure 35: Y-X-Y Euler Sequence.

$$Y_1X_2Z_3 = \begin{bmatrix} c_1c_3 + s_1s_2s_3 & c_3s_1s_2 - c_1s_3 & c_2s_1 \\ c_2s_3 & c_2c_3 & -s_2 \\ c_1s_2s_3 - c_3s_1 & c_1c_3s_2 + s_1s_3 & c_1c_2 \end{bmatrix}$$

Figure 36: Y-X-Z Euler Sequence.

3.12.4: Statistical Analysis

To assess the accuracy of the different motion-capture-based methods for identifying the COR, data analysis incorporated measures of error and precision, building upon methodologies outlined in [56], [89]. The resultant displacement between predicted COR positions generated by the different methods and the true COR, established through fluoroscopy, was computed to quantify the average error.

To evaluate the normality of each model, the Shapiro-Wilk test was applied. The non-parametric Wilcoxon test was employed for non-normally distributed groups to test for significant differences among groups. All reported values were presented as mean ±

standard deviation (SD), with statistical significance defined by a p-value of less than 0.05.

Furthermore, to evaluate the accuracy of the acromion, midpoint, and centerpoint techniques in locating the shoulder center, the respective joint center coordinates were expressed within an anatomical coordinate system of the humerus using the geometric center determined from fluoroscopy data as the origin (0,0,0). The resultant error is also reported in components in this coordinate system, where X is the anterior-posterior (A/P) direction, Y is the superior-inferior (S/I) direction, and Z represents the medial-lateral (M/L) coordinate direction. Deviations from this origin were considered direct error indicators in determining the COR.

A generalized mixed-effect linear regression was also conducted to compare the impact of subjects, arm side (dominant/ non-dominant), movements, methods, and the resultant value for the COR. This technique accounts for fixed and random effects, accommodating correlated data structures often encountered in biomechanical studies. The subjects were used as a random input, while the arm side, movement, and method were utilized as fixed effects, and COR was used as the target.

Lastly, the obtained dataset underwent linear regression analysis to derive an equation that accurately captures the relationship between marker error and changes in arm elevation or arm rotation angles. This equation is a valuable tool for quantifying the increase in marker error, measured in millimeters, corresponding to each incremental degree of arm elevation or rotation.

Chapter Four: Results

This chapter discusses the essential results of the study and how they compare to previous research. The following section compares the marker-based methods tested to investigate the humerus COR, summarized in boxplots. Each boxplot represents the error in the 3D position of the COR decomposed into the A/P, S/I, and M/L directions. Plots of the resultant COR as a function of the degree of GH elevation or rotation are also presented to show how individual subjects differ from each other and to illustrate which methods show the slightest error. Finally, displacement error of COR in the A/P, S/I, and M/L directions, along with the resultant for the three marker-based methods (acromion, midpoint, centerpoint) at a minimum and maximum degree of (elevation or rotation), are presented in Tables 4,5,6,7 and 8 (Appendix).

4.1: Comparison of Humeral Center of Rotation Location

4.1.1: Abduction Activity

The analysis focused on the error of the COR location expressed in local humeral X, Y, and Z coordinates. X represents the error in the A/P direction, Y represents the error in the S/I direction, and Z is the error in the M/L direction. These error values are presented as box and whisker plots, with each set of plots depicting data from the different dynamic activities: abduction, abduction with 5-lb weight, flexion, and external rotation at 90 degrees arm abduction, external rotation at the side, high circumduction, and low circumduction.

The box plot provides a comprehensive understanding of the data by presenting the precision of the data by showing a smaller or larger interquartile range (IQR), which encapsulates the range between the first quartile (Q1) and the third quartile (Q3) of the dataset. The accuracy of the data presented by the median (middle quartile) marks the mid-point of the data and is shown by the line that divides the box into two parts. The median line summarizes 50% of the data, and the closer the median is to zero, the more accuracy the data set shows. The whiskers represent the error, and the outliers; shorter whiskers and fewer outliers indicate less error the data set shows and vice versa.

For this study, the dataset's IQR, Q1, and Q3, along with the median, remained within a displacement error of less than 40 mm from the geometric center of the humerus for all methods. The boxplot whiskers illustrate data variability and consistency. It is worth noting that a few individual outliers emerged outside the whiskers, indicating data points significantly differing from the norm. These outliers were observed mainly in the A/P direction for the midpoint and center point methods.

The data summarizing the results from the abduction activity are depicted in Figure 37.

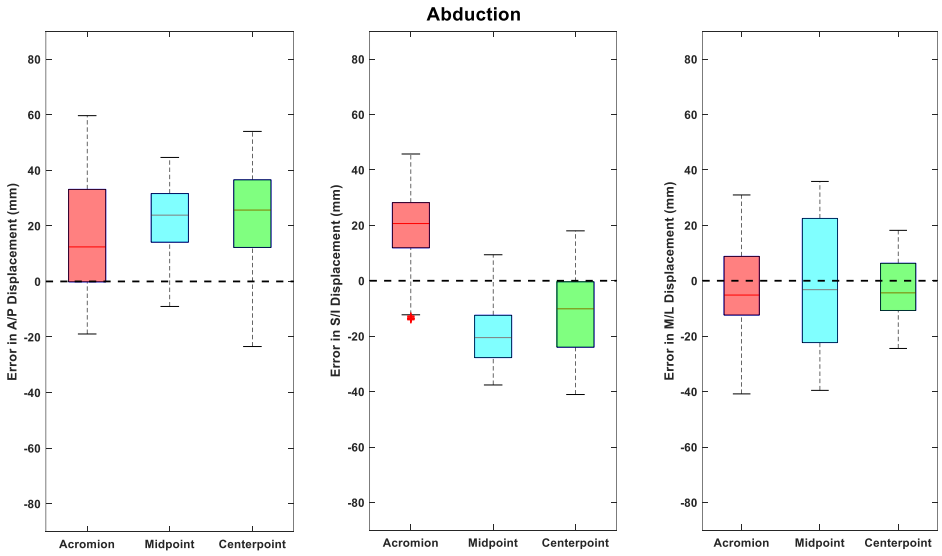

Figure 37: Box plot presenting the mean error of the humeral COR estimates, broken into the A/P, S/I and M/L directions, for the three different tracking methods (acromion, midpoint, centerpoint) for the abduction movement.

The errors in the COR during abduction movement across the complete range of motion in the A/P, S/I, and M/L directions were analyzed. For the acromion method, the median error was 12.4±19.8 mm, indicating a tendency for the COR to move anteriorly. Similarly, using the midpoint method, a median error of 23.9±11.3 mm was observed, indicating anterior movement of the COR. The centerpoint approach showed a median error of 25.7±15.9 mm, suggesting anterior COR displacement.

In the S/I direction, the errors in the COR were as follows. The acromion method showed a median error of 20.6±12.5 mm, indicating superior COR displacement. Conversely, the midpoint method displayed a median error of 20.5±10.3 mm, indicating an inferior shift of the COR. The centerpoint method resulted in a median error of 10.1±14.1 mm, implying an inferior movement of the COR.

For the M/L direction, the analysis revealed the following COR errors. The acromion method had a median error of 5.2±15.2 mm, indicating lateral COR displacement. The midpoint method showed a median error of 3.2±22.9 mm, suggesting lateral COR movement, and the centerpoint method resulted in a median error of 4.4±10.4 mm, indicating lateral movement of the COR.

To synthesize the 3D error of COR, the following equation was used to calculate the resultant error for all subjects across all movements:

$$Resultant = \sqrt{(x)^2 + (y)^2 + (z)^2}$$

In this equation, (x) represents the A/P components of error, (y) represents the S/I components of error, and (z) represents the M/L components of error. The resultant errors of each method for each subject as a function of elevation angle are depicted in Figure 38.

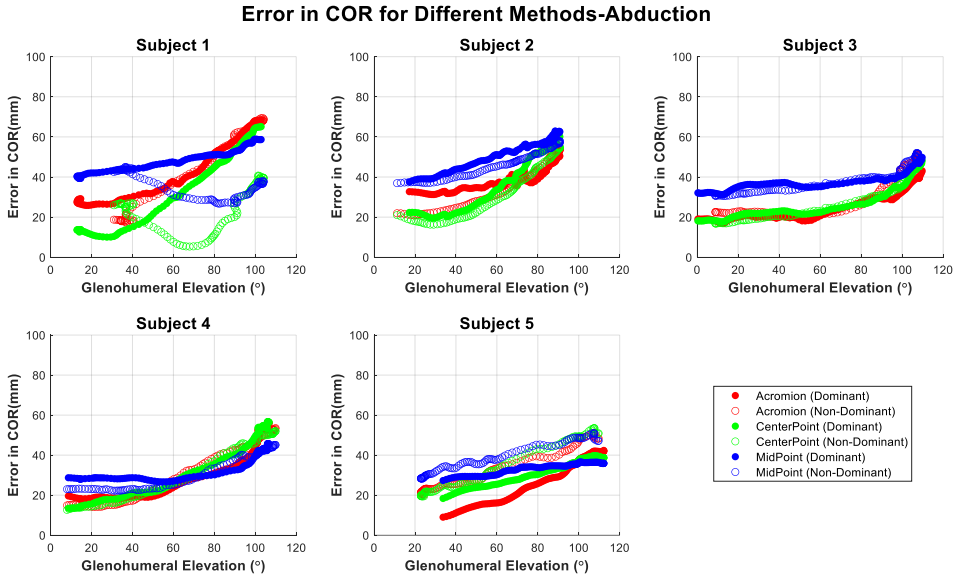

Figure 38: Error in the resultant displacement across the three tracking methods for all subjects during the abduction movement as a function of GH elevation angle.

The figure above depicts the disparities in COR error between the dominant and non-dominant arms across all subjects. It is worth noting that while participants exhibited variations in their ROM, it was observed that COR errors during the abduction movement tended to escalate as the glenohumeral elevation angle increased for all subjects across all three tracking methods. The three methods demonstrated similar performance, with the average resultant error across subjects ranging from a minimum of 23.8 mm at the neutral position to a maximum of 51.1 mm, generally increasing as the humeral elevation angle increased towards the maximum abduction angle.

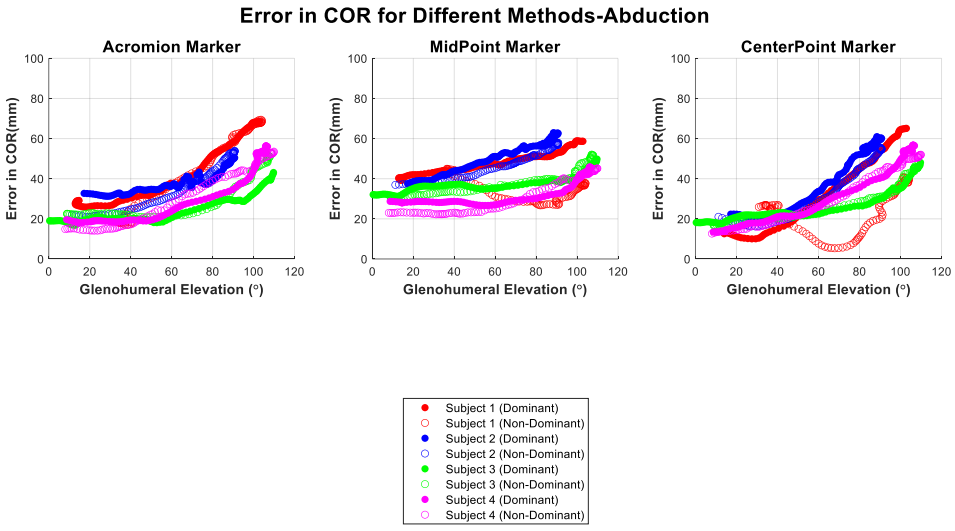

Figure 39: Error in the resultant displacement for the three tracking methods across all subjects for dominant and non-dominant arms. Note the same trend is observed as with that in Figure 38, but here, with all subjects combined.

4.1.2: Abduction Activity Holding 5 lb. Weight

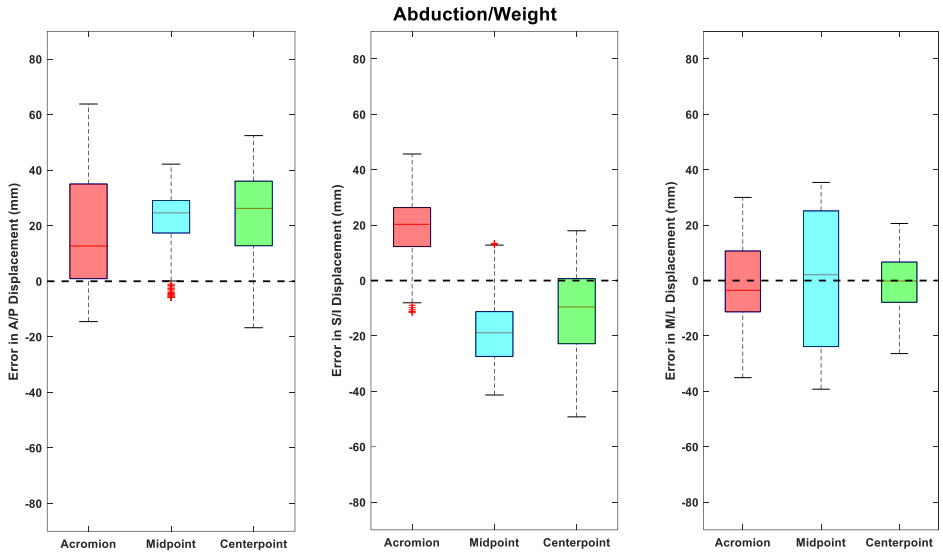

Figure 40: Box plot presenting the mean error of the humeral COR estimates broken into the A/P, S/I and M/L directions, for the three different tracking methods (acromion, midpoint, centerpoint) for the weighted abduction movement.

The study investigated COR errors during abduction movement by adding a five lb. weight, covering the complete range of motion in the A/P direction. The results revealed that for the acromion method, the median error was 12.7±20.4 mm, indicating a tendency for the COR to move anteriorly. Similarly, employing the midpoint method resulted in a median error of 24.6±10.0 mm, signifying anterior movement of the COR. Likewise, the centerpoint method displayed a median error of 26.2±15.5 mm, suggesting anterior displacement of the COR.

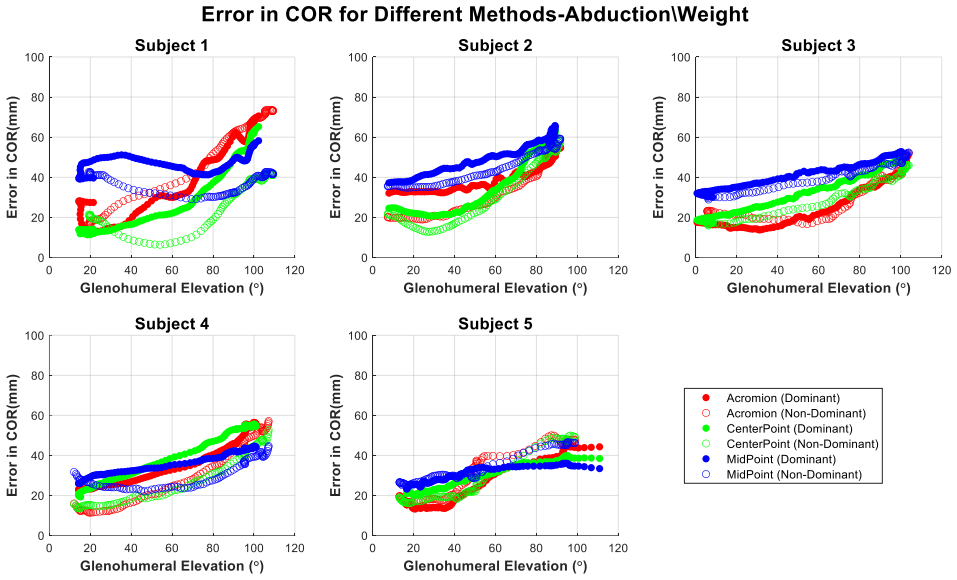

Figure 41: Error in the resultant displacement across the three tracking methods for all subjects during the weighted abduction movement as a function of GH elevation angle.

In terms of the COR errors in the S/I direction, the findings were as follows. The acromion method showed a median error of 20.3±11.2 mm, indicating superior movement of the COR. On the other hand, utilizing the midpoint method produced a median error of 18.9±11.5 mm, suggesting movement of the COR in the inferior direction. Furthermore, the centerpoint method resulted in a median error of 9.5±15.0 mm, signifying movement in the inferior direction.

Examining the COR errors in the M/L direction, the analysis revealed the following. The acromion method had a median error of 3.5±15.7 mm, indicating lateral COR displacement. The midpoint method displayed a median error of 2.1±24.2 mm, suggesting medial movement of the COR. Meanwhile, for the centerpoint method, a

median error of 0.2±10.8 mm was observed, indicating small lateral movement of the COR.

During the evaluation of humeral COR errors in the context of weighted abduction movements, it became evident that similar trends of error and bias were consistently observed. These trends held true for both weighted and unweighted abduction, and they persisted even when additional muscle groups, such as the trapezius and serratus anterior, were engaged. All three methods exhibited similar performance, with the average resultant error across subjects ranging from a minimum of 23.9 mm at the neutral position to a maximum of 52.2 mm. These errors generally increased as the humeral elevation angle progressed toward the maximum abduction angle.

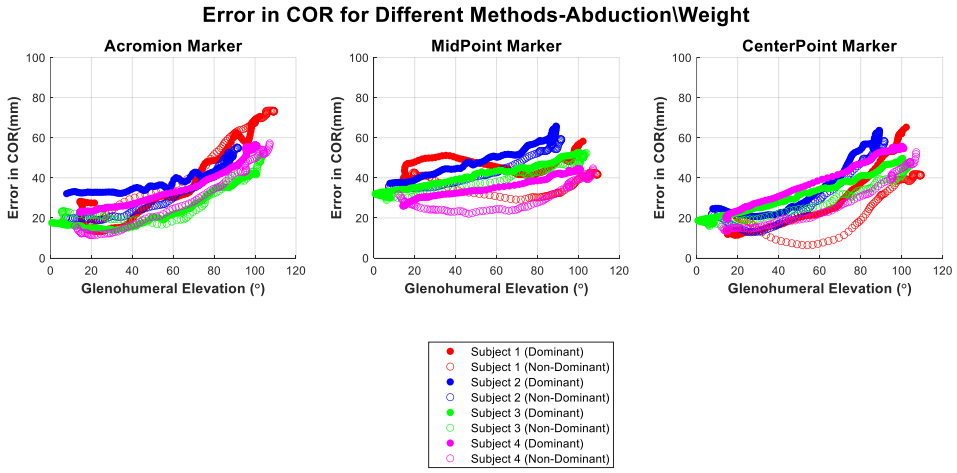

Figure 42: Error in the resultant displacement for the three tracking methods across all subjects for dominant and non-dominant arms. Note the same trend is observed as with that in Figure 41, but here, with all subjects combined.

4.1.3: Flexion Activity

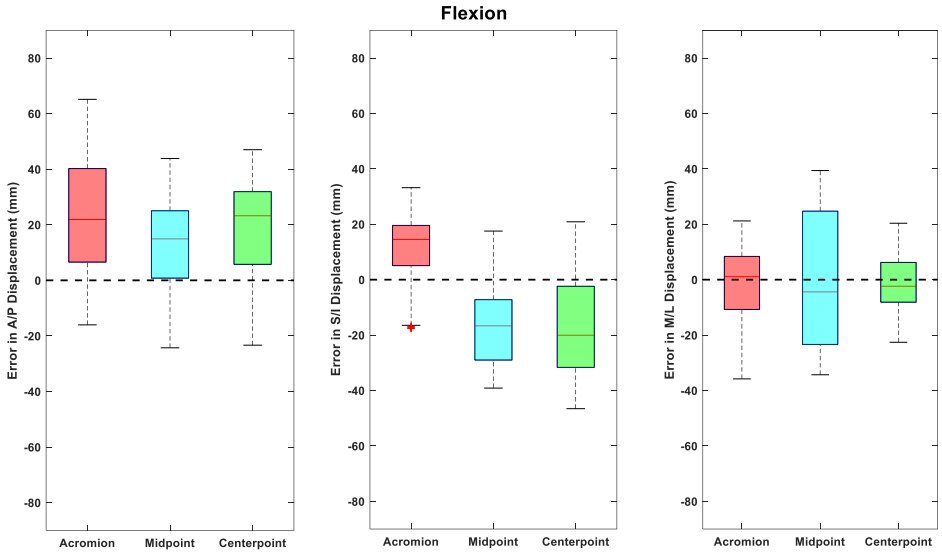

Figure 43: Box plot presenting the mean error of the humeral COR estimates broken into the A/P, S/I and M/L directions, for the three different tracking methods (acromion, midpoint, centerpoint) for flexion movement.

When examining the errors in COR during flexion movements across the complete range of motion in the A/P direction. For the acromion method, the median error was 12.9±20.9 mm, indicating an anterior shift of the COR. Similarly, the midpoint method resulted in a median error of 14.9±16.1 mm, signifying an anterior movement of the COR; also, the centerpoint method yielded a median error of 23.2±16.1 mm, suggesting anterior displacement of the COR.

Looking at the COR errors in the S/I direction. The acromion method displayed a median error of 14.5±10.9 mm, indicating a superior movement of the COR. In contrast, the midpoint method revealed a median error of 16.7±14.2 mm, suggesting movement of

the COR in the inferior direction. The centerpoint method exhibited a median error of 20.0±18.0 mm, indicating a shift of the COR in the inferior direction.

In terms of the COR errors in the M/L direction. The acromion method had a median error of 1.1±13.3 mm, signifying a slight medial COR displacement. In contrast, the midpoint method showed a median error of 4.4±24.9 mm, implying lateral movement of the COR, while the centerpoint method resulted in a median error of 2.4±9.1 mm, indicating a lateral displacement of the COR.

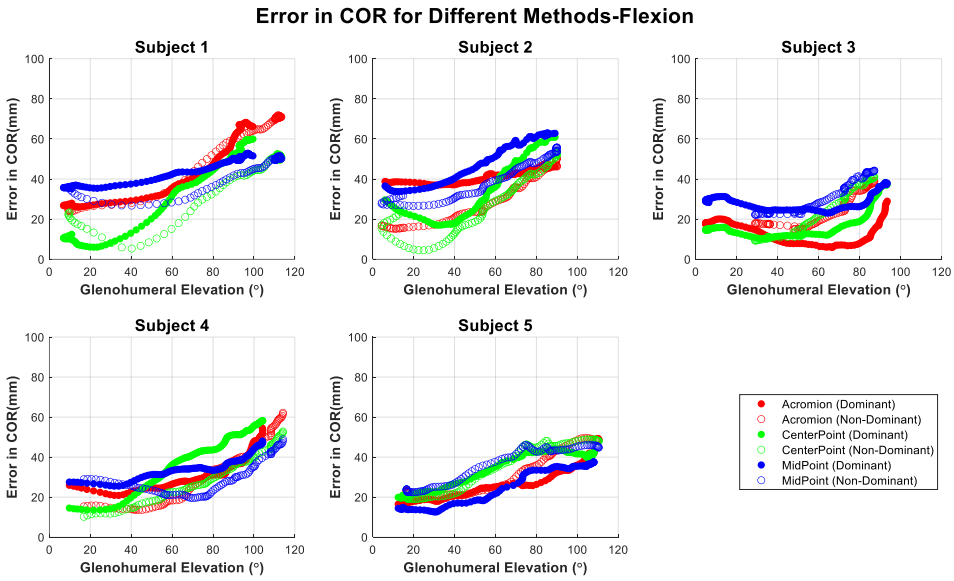

Figure 44: Error in the resultant displacement across the three tracking methods for all subjects during the flexion movement as a function of GH elevation angle.

During flexion, the humeral COR consistently shifted anteriorly across all tested COR methods. In terms of the S/I direction, the COR exhibited varying trends depending on the method employed. The midpoint and centerpoint methods resulted in an inferior shift of the COR, while the acromion method showed a superior shift. Similar trends were

observed in the M/L direction, with the calculated COR location mostly adhering to the previously described patterns.

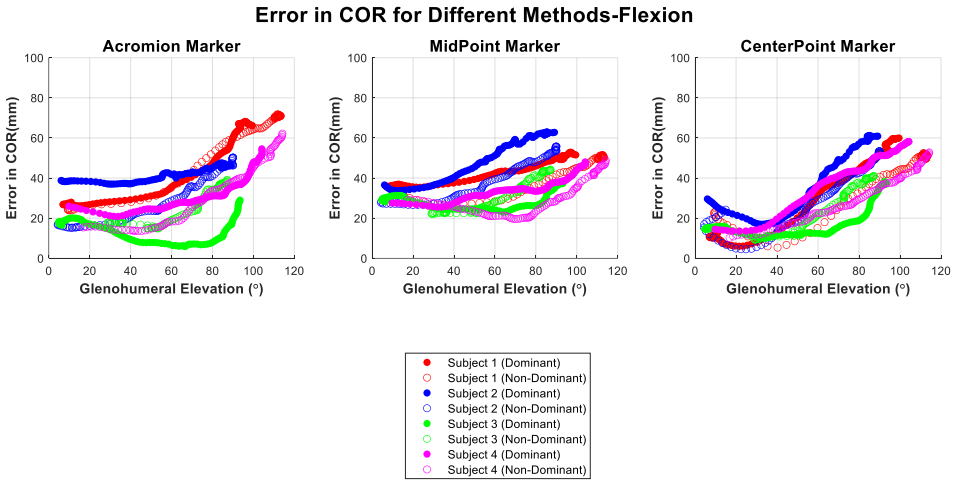

Figure 45: Error in the resultant displacement for the three tracking methods across all subjects for dominant and non-dominant arms. Note the same trend is observed as with that in Figure 44, but here, with all subjects combined.

In a broader context, all three COR methods demonstrated similar performance characteristics. The resultant error averaged across subjects ranged from a minimum of 22.9 mm at the neutral position to a maximum of 49.8 mm. Generally, these errors increased as the humeral elevation angle progressed toward the maximum flexion angle.

4.1.4: External Rotation Activities (at 90 degrees, at side)

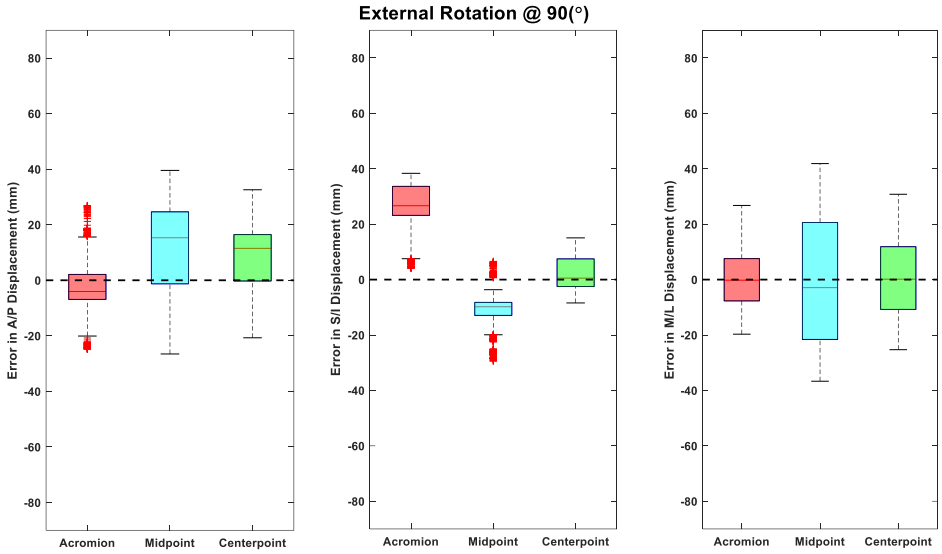

Figure 46: Box plot presenting the mean error of the humeral COR estimates broken into the A/P, S/I and M/L directions, for the three different tracking methods (acromion, midpoint, centerpoint) for the external rotation at 90° movement.

The complete analysis of COR errors during external rotation at a 90-degree movement across the complete range of motion revealed distinct patterns associated with each COR method. In the A/P direction, the acromion method displayed a relatively minor median error of 4.0±9.8 mm, suggesting a posterior shift of the COR. In contrast, the midpoint method exhibited anterior movement, with a median error of 15.3±16.5 mm, while the centerpoint method resulted in a median error of 11.5±11.7 mm, indicating anterior displacement of the COR.

Analyzing the S/I direction, noteworthy variations were observed. The acromion method led to a superior COR shift, with a median error of 26.7±10.4 mm.

Conversely, the midpoint method revealed an inferior movement of the COR, with a median error of 9.8±7.8 mm. In contrast, the centerpoint method exhibited a relatively minor superior displacement, as reflected by a median error of 0.5±5.8 mm.

Regarding the M/L direction, the calculated COR locations adhered to specific trends. The acromion method showed a minor lateral COR shift, with a median error of 0.2±9.7 mm. In contrast, the midpoint method exhibited a lateral movement, indicated by a median error of 2.9±23.4 mm, while the centerpoint method suggested a slight lateral COR displacement, with a median error of 0.2±13.6 mm.

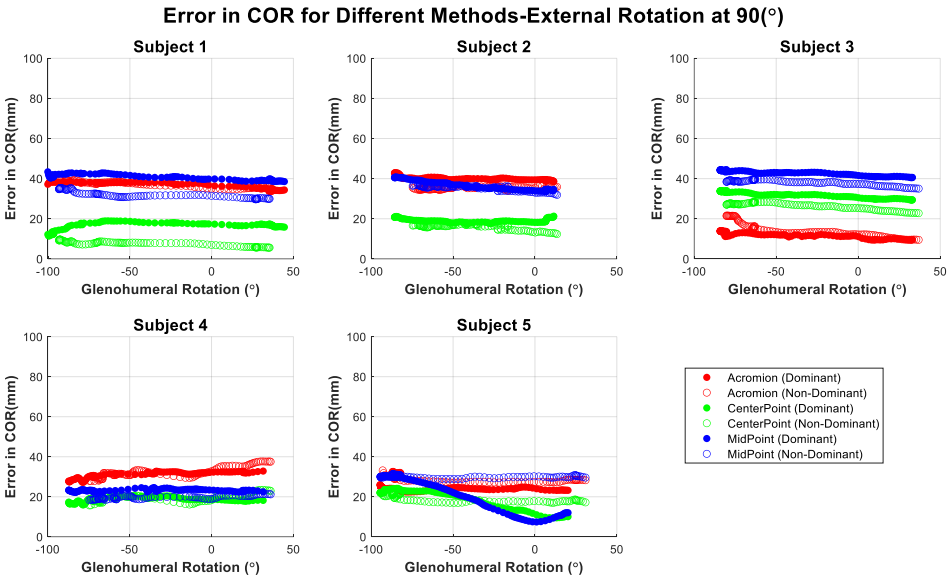

Figure 47: Error in the resultant displacement across the three tracking methods for all subjects during the external rotation at 90° movement as a function of GH rotation angle.

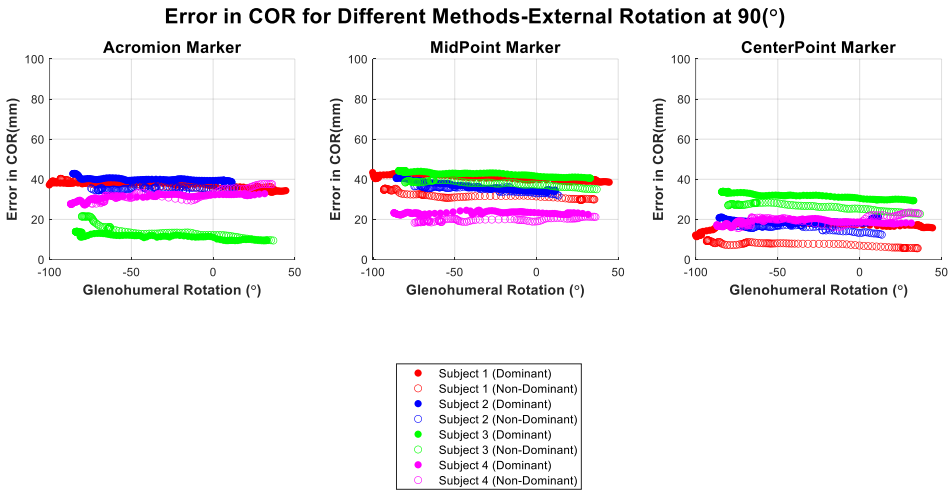

Figure 48: Error in the resultant displacement for the three tracking methods across all subjects for dominant and non-dominant arms. Note the same trend is observed as with that in Figure 47, but here, with all subjects combined.

All three methods exhibited comparable performance, with the resultant error averaging across subjects ranging from a minimum of 25.2 mm at the neutral position to a maximum of 28.0 mm. Generally, these errors were more consistent as the humeral rotation angle progressed toward the maximum external rotation angle.

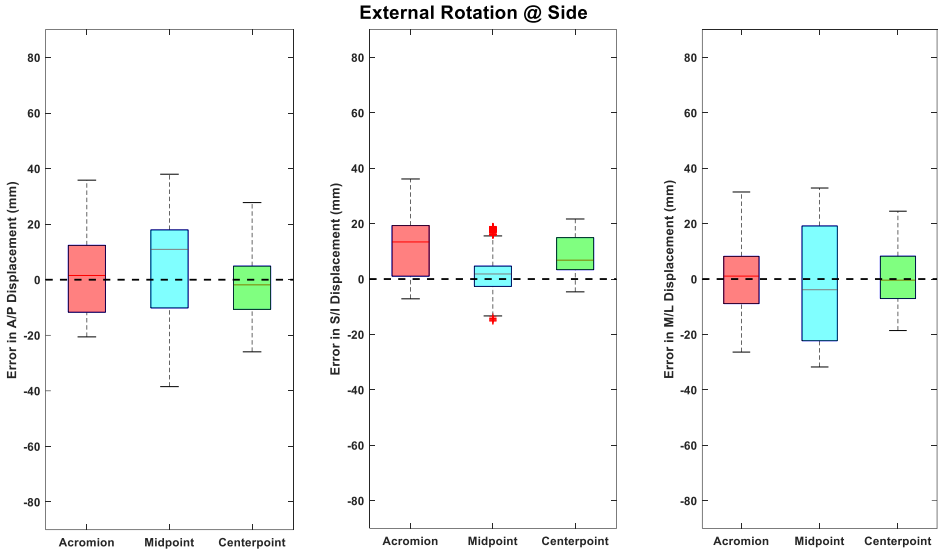

Figure 49: Box plot presenting the mean error of the humeral COR estimates broken into the A/P, S/I and M/L directions, for the three different tracking methods (acromion, midpoint, centerpoint) for the external rotational movement at the side.

The analysis of COR errors during external rotation with the arm at the side, covering the complete ROM, revealed distinctive trends associated with each COR tracking method. In terms of the A/P direction, the acromion method showed a relatively minor median error of 1.5±14.3 mm, indicating a subtle anterior shift of the COR. In contrast, the midpoint method demonstrated a more significant anterior movement, with a median error of 10.9±16.9 mm. The centerpoint method resulted in a median error of 1.8±11.4 mm, signifying a slight posterior displacement of the COR.

Examining the S/I direction, the acromion method exhibited a median error of 13.4±11.9 mm, indicating a superior shift of the COR. The midpoint method displayed a median error of 1.8±7.5 mm, suggesting superior movement of the COR. In contrast, the

centerpoint method demonstrated a median error of 6.8±6.9 mm, signifying a superior displacement of the COR.

In the M/L direction, the findings were as follows: the acromion method showed a median error of 1.1±11.9 mm, indicating a slight medial shift of the COR. The midpoint method exhibited a more pronounced lateral movement of the COR, with a median error of 3.9±20.9 mm. The centerpoint method resulted in a median error of 0.4±10.3 mm, suggesting a minor lateral displacement of the COR.

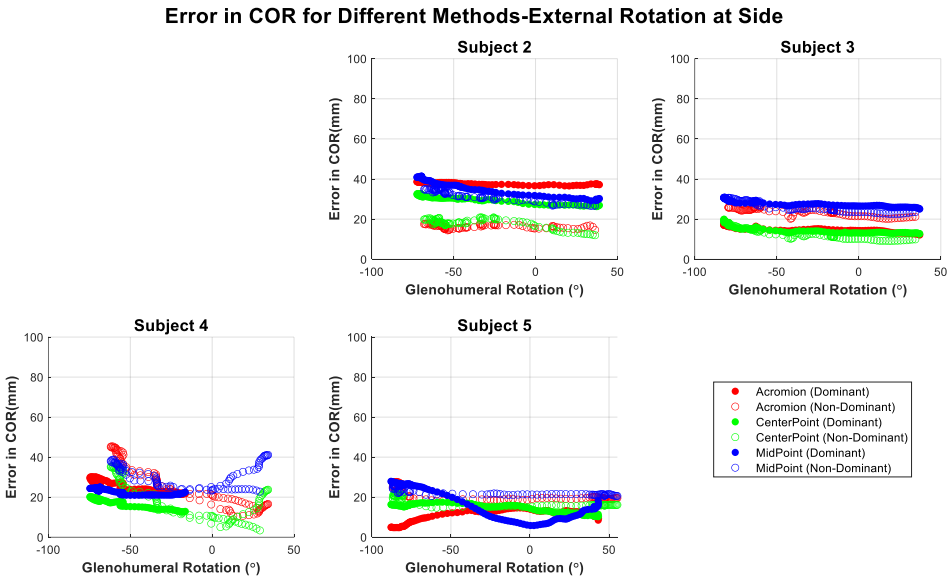

Figure 50: Error in the resultant displacement across the three tracking methods for all subjects during the external rotational movement at the side as a function of GH rotation angle.

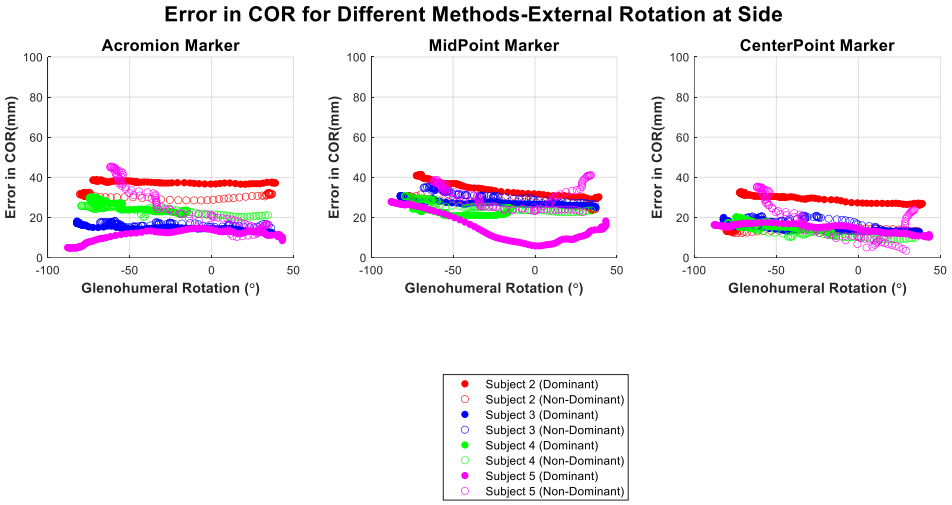

Figure 51: Error in the resultant displacement for the three tracking methods across all subjects for dominant and non-dominant arms. Note the same trend is observed as with that in Figure 50, but here, with all subjects combined.

The error in COR for the external rotation at side degrees showed that all three methods perform similarly with a resultant error average across subjects ranging from a minimum of 18.9 mm at a neutral position to a maximum of 24.7 mm and generally increasing with humeral rotation till it reaches maximum rotation angle.

The external rotation to the side graphs depicts the lowest error when comparing the COR with other movements. However, these graphs also reveal the most significant differences between the dominant and non-dominant arms.

One of the trials had to be excluded from the analysis due to the absence of fluoroscopy images, which may have contributed to the observed discrepancies in the data.

4.1.5: Low and High Circumduction Activities

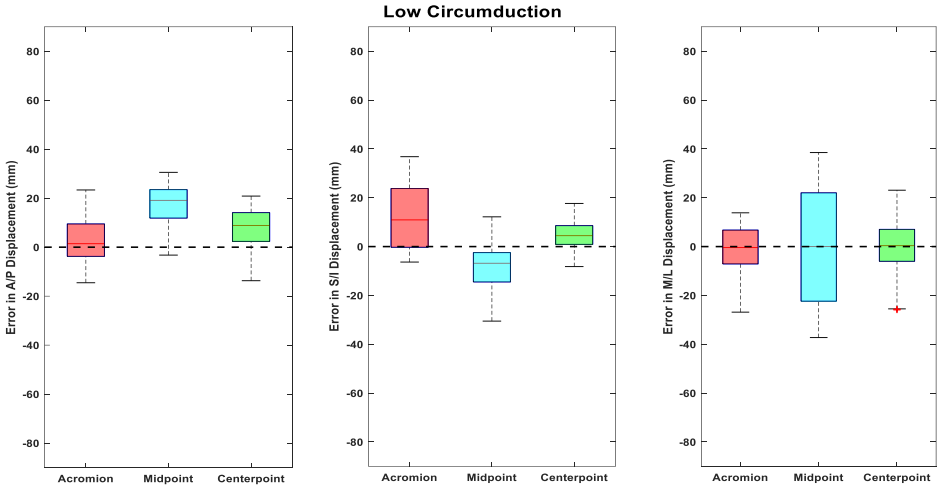

Figure 52: Box plot presenting the mean error of the humeral COR estimates broken into the A/P, S/I and M/L directions, for the three different tracking methods (acromion, midpoint, centerpoint) for the low circumduction movement.

The accuracy of COR measurements during low circumduction movement across the complete ROM was assessed using three different methods: the acromion method, the midpoint method, and the centerpoint method. The results revealed variations in error across different anatomical directions. In the A/P direction, the acromion method exhibited the lowest median error at 1.4±8.6 mm in the anterior direction, while the midpoint method had a considerably higher median error of 19.1±7.4 mm. The centerpoint method fell in between, with a median error of 8.8±8.7 mm in the anterior direction.

In the S/I direction, the acromion method had a median error of 10.9±12.6 mm in the superior direction, the midpoint method showed 6.8±9.8 mm in the inferior direction, and the centerpoint method exhibited 4.5±5.7 mm in the superior direction.

Finally, in the M/L direction, the acromion method had a median error of 0.4±10.3 mm in the lateral direction, the midpoint method had a wide range of error from 0 mm, indicating precision, to 24.5 mm in the medial direction, and the centerpoint method had a median error of 0.4±11.3 mm in the medial direction.

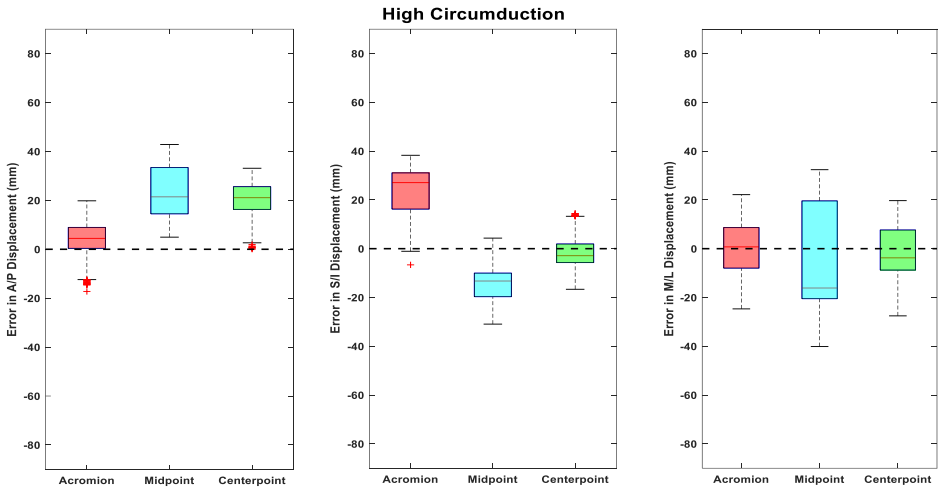

Figure 53: Box plot presenting the mean error of the humeral COR estimates broken into the A/P, S/I and M/L directions, for the three different tracking methods (acromion, midpoint, centerpoint) for the high circumduction movement

Lastly, COR error measurements during high circumduction movements in the A/P direction, the acromion method demonstrated the most minor median error at 4.5±7.1 mm, while the midpoint and centerpoint methods exhibited notably higher errors of 21.4±9.9 mm and 21.1±6.6 mm in the anterior direction, respectively.

In the S/I direction, the acromion method displayed the largest median error of 27.1±10.8 mm in the superior direction, whereas the midpoint and centerpoint methods.

we had lower errors of 13.3±8.5 mm in the inferior direction and 2.8±5.9 mm in the inferior direction, respectively.

For M/L direction, the acromion method showed a median error of 0.7±11.5 mm, showing medial movement in COR, while the midpoint method had a median error of 16.1±22.8 mm, and the centerpoint method had a median error of 3.8±11.3 mm in the lateral direction. Notably, the low and high circumduction movement incorporates a complex interplay of shoulder movements, making it challenging to determine a specific ROM for COR displacement error analysis. Additionally, it is interesting to note that the low circumduction methods generated less displacement error, possibly due to the involvement of a greater number of muscles in the process of raising the arm, leading to increased skin movement during high circumduction.

4.2: Second Order Regression Analysis

Regression analysis is indeed a valuable statistical method used across various fields. A second-order linear regression model is used to establish a quadratic relationship between the dependent variable, which is the error COR, and the independent variable, the elevation or rotation angle depending on the movement analyzed. This approach involves constructing a quadratic expression, resulting in a parabolic curve that helps describe the relationship between these two variables.

The regression model will provide insights into the nature of this relationship, such as whether the increase in error is linear or if it follows a more complex quadratic pattern.

Understanding these relationships is crucial for assessing the impact of arm movements on the accuracy and precision of COR measurements. It allows researchers to

make informed decisions and adjustments in their methodologies or equipment to improve the reliability of such measurements. This analysis performed on the centerpoint result since it generated less error in COR compared to other methods.

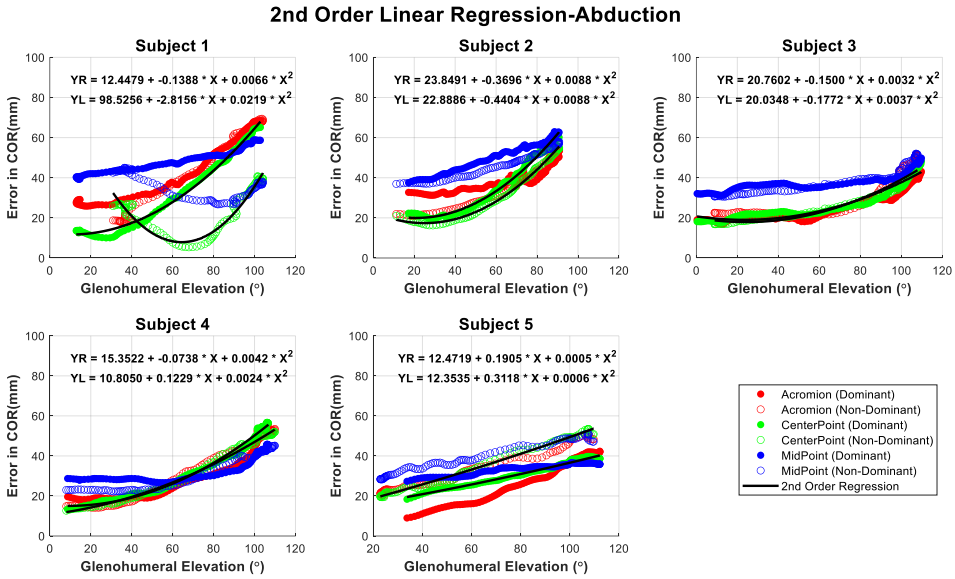

Figure 54: Second-order linear regression analysis conducted to assess the error in resultant displacement across the centerpoint method for all subjects during abduction movement, with respect to the GH elevation angle.

In the context of abduction movement, it's noteworthy that there are distinct variations in the COR error as the arm is elevated, with a particular focus on the differences between the dominant and non-dominant arms. For the dominant arm, the data reveals that, on average, the COR error increases by a relatively small 0.18 mm for each degree of arm elevation during abduction. In contrast, the non-dominant arm shows a more substantial increase in COR error, with an average of 0.77 mm for each degree of arm elevation during abduction movements.

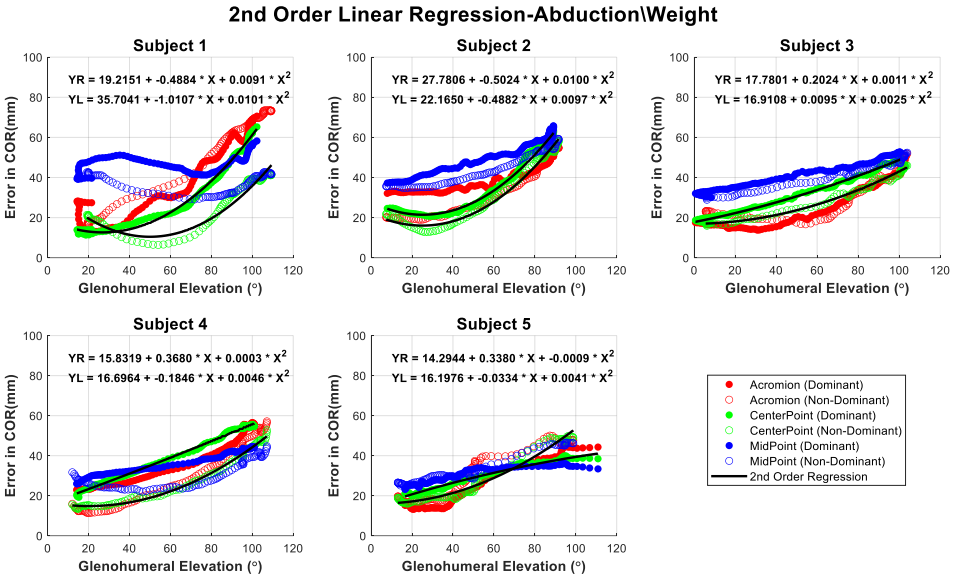

Figure 55: 2nd order linear regression analysis conducted to assess the error in resultant displacement across the centerpoint method for all subjects during weighted abduction movement with respect to the GH elevation angle.

In the context of weighted abduction movements, the analysis highlights the relationship between COR error and the degree of arm elevation, the data reveals that, on average, for each degree of arm elevation during weighted abduction, the COR error increases by approximately 0.38 mm for the dominant arm and 0.35 mm for the non-dominant arm.

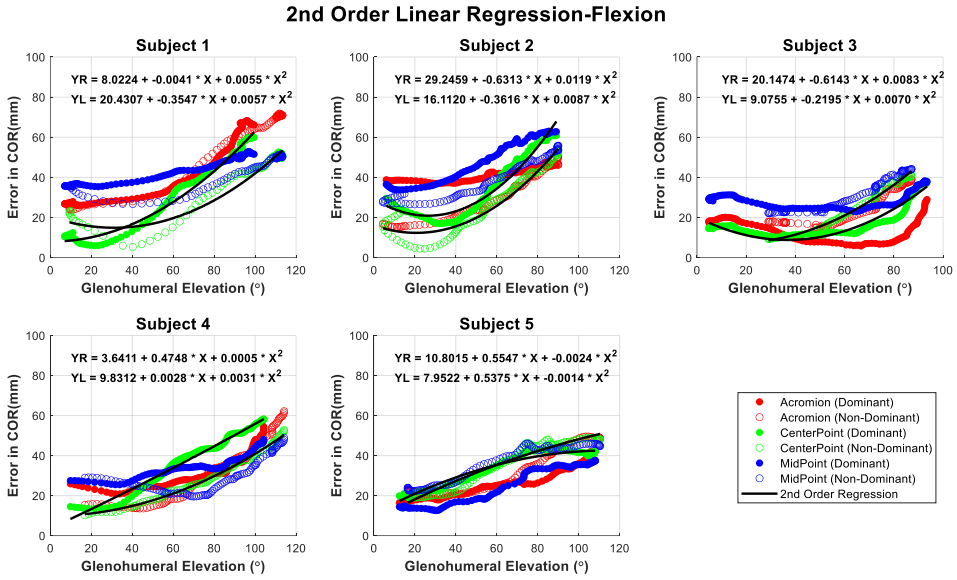

Figure 56: 2nd order linear regression analysis conducted to assess the error in resultant displacement across the centerpoint method for all subjects during flexion movement, with respect to the GH elevation angle.

In the context of flexion movements, the examination of COR error and its relationship to arm elevation reveals significant insights into the differences between the dominant and non-dominant arms. The data shows that, on average, with each degree of arm elevation during flexion, the COR error increases. For the dominant arm, this increase is notably higher, at around 0.46 mm for each degree of elevation. In contrast, the non-dominant arm experiences a slightly lower rate of increase, averaging approximately 0.30 mm for each degree of elevation.

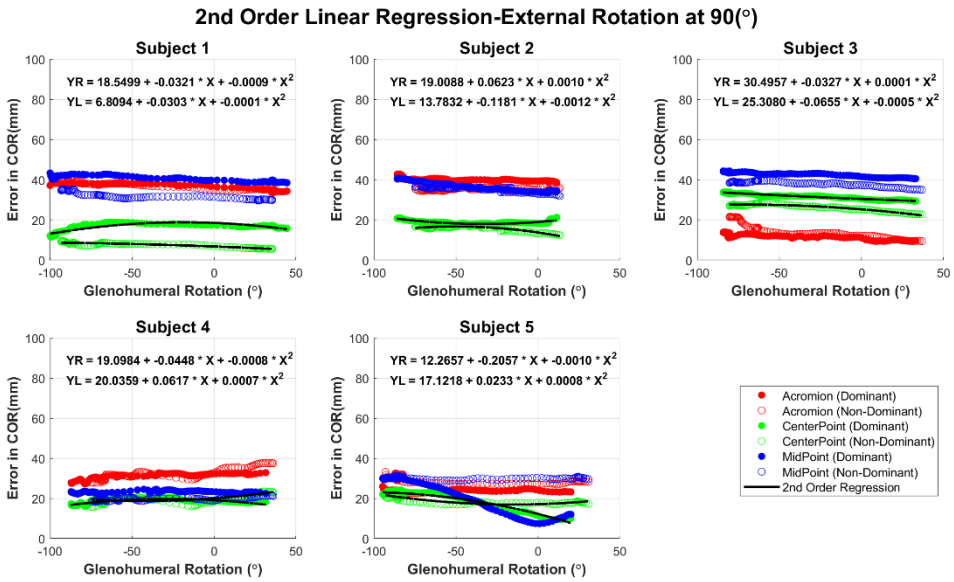

Figure 57: 2nd order linear regression analysis conducted to assess the error in resultant displacement across the centerpoint method for all subjects during external rotation at 90° movement, with respect to the GH rotation angle.

In the context of external rotation at a 90-degree movement, the analysis of COR error provides valuable insights into the impact of arm rotation on measurement accuracy. For the dominant arm, the rate of increase is slightly higher, with an average of approximately 0.08 mm for each degree of arm rotation. In contrast, the non-dominant arm exhibits a slightly lower rate of increase, at about 0.06 mm for each degree of arm rotation.

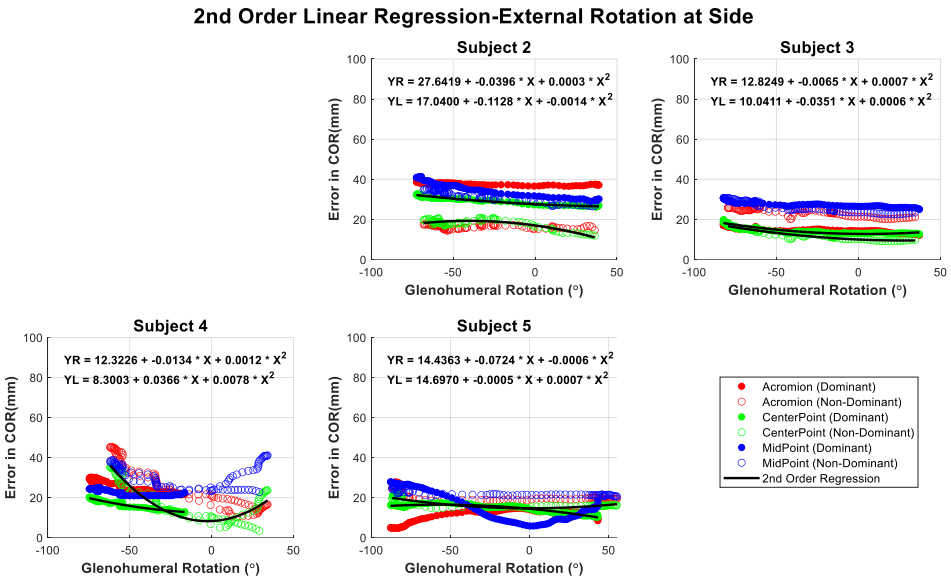

Figure 58: 2nd order linear regression analysis conducted to assess the error in resultant displacement across the centerpoint method for all subjects during external rotation at side movement, with respect to the GH rotation angle.

In the context of external rotation at the side movement, the analysis of COR error provides valuable insights into the relationship between arm rotation and measurement accuracy. For the dominant arm, the rate of increase is relatively lower, with an average of approximately 0.03 mm for each degree of arm rotation. In contrast, the non-dominant arm exhibits a slightly higher rate of increase, averaging about 0.05 mm for each degree of arm rotation.

4.3: Generalized Linear Mixed Models

The Generalized Linear Mixed Models (GLMM) analysis used estimates for both fixed and random effects, revealing significant correlations between the error in the COR and the degrees of abduction and rotation (Figure 59). Notably, the findings indicate that

the lowest COR error occurred during rotation at side movement. Furthermore, the results suggest that an increase in the angle of elevation is associated with a proportional increase in error (Figure 60). A notable observation is that the non-dominant arm exhibited less error when compared to the dominant arm (Figure 61). Finally, the centerpoint method consistently demonstrated the least amount of error across all types of movements, for both the dominant and non-dominant arms, when contrasted with the midpoint and acromion methods (Figure 62).

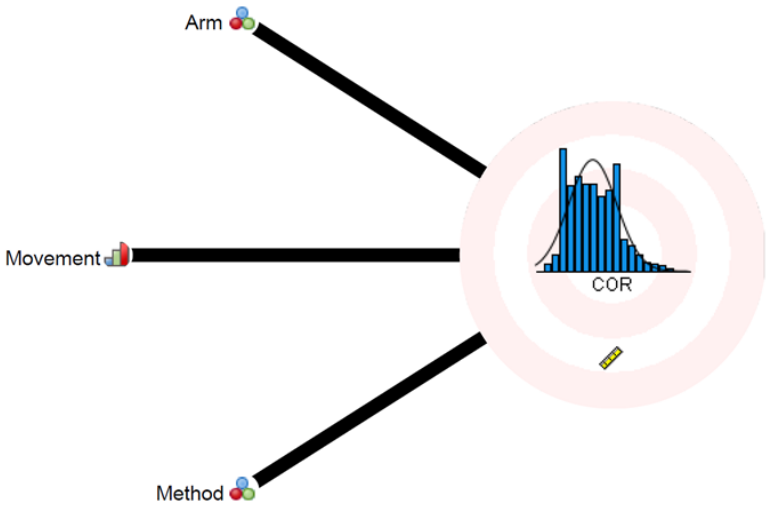

Figure 59: GLMM fixed effect inputs.

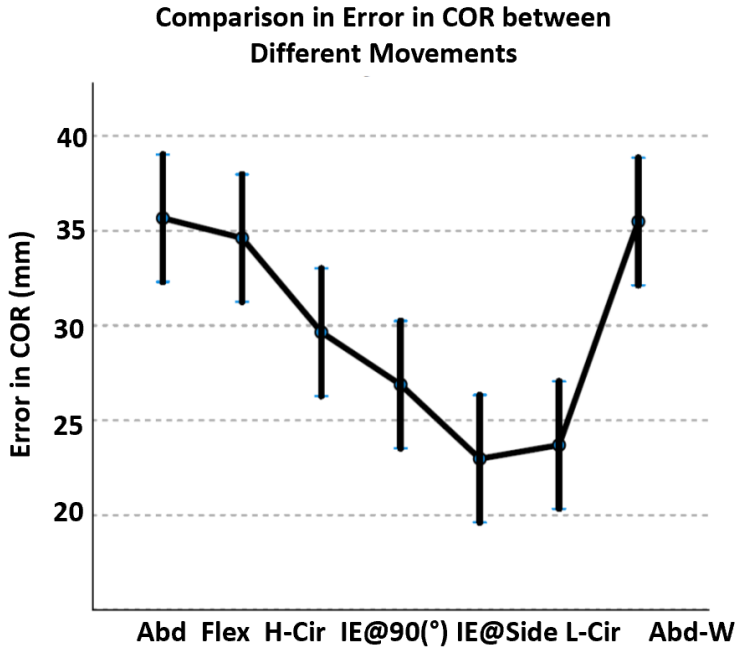

Figure 60: GLMM comparison between different movements for all subjects.

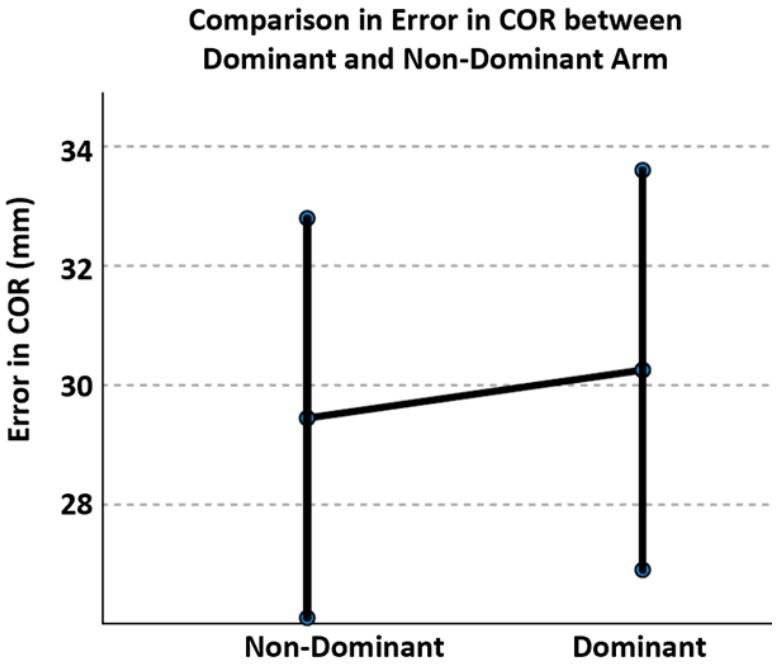

Figure 61: GLMM comparison between dominant and non-dominant arms.

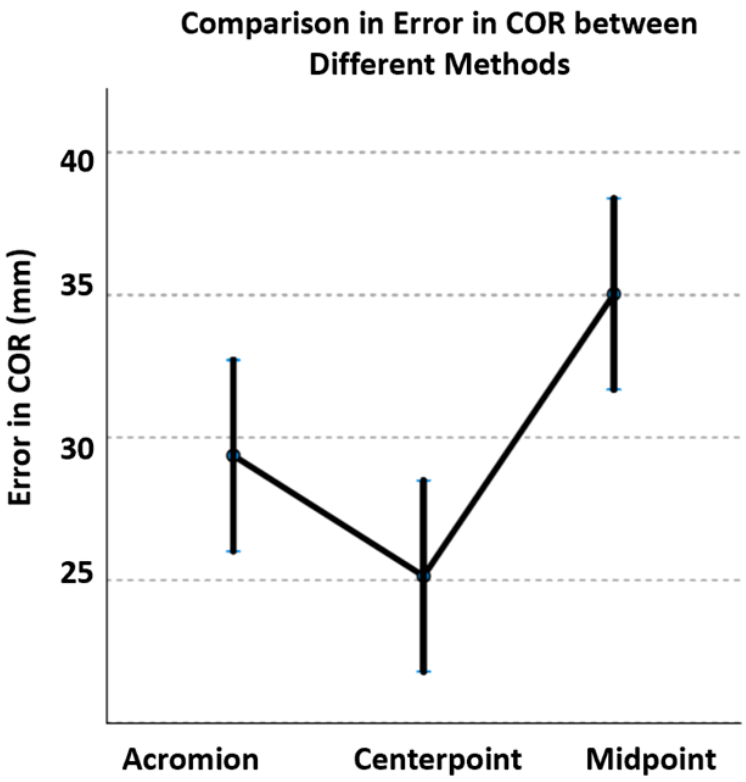

Figure 62: GLMM comparison between different methods.

Chapter Five: Discussion and Conclusion

This research is focused on investigating the use of the MOCAP system in determining humerus COR for *in vivo* biomechanical analysis of shoulder movement. First, we will compare our study results with previous literature and then move to discuss the limitations of the study and future recommendations.

5.1: Comparison with Literature

Meskers et al. [90] employed linear regression techniques to determine the rotation center of the glenohumeral joint relative to scapular landmarks utilizing 36 data points situated on both the glenoid and humeral head surfaces. Through the application of mathematical sphere fitting procedures to the humeral head and glenoid, the authors estimated the precise location of the glenohumeral joint rotation center. Orientation errors were quantified across the complete elevation range of the humerus, spanning from its resting position to the point of maximum elevation. Utilizing spheres to approximate the contours of the humeral head and glenoid was justified by the attainment of notably low residual errors and standard errors of the means. Mesker's findings unveiled a minimal increase in mean residual error when using the radius of the humeral head to estimate glenohumeral joint rotation. This observation underscores the validity of the GH joint rotation estimation method.

This data also suggests that the location of the COR is approximately 45 mm inferior to the acromion (parameter My), which is similar to the value of 4 cm that has been used in some previous work [91] and the inspiration for the acromion COR calculation.

Our research underscores the variability of COR location with specific movement types and humeral head dimensions. Our study showed larger errors in the COR when comparing our findings with the data from Veeger et al. [92] (Figure 63). Veeger achieved mean errors from (8 to 15.6) mm, but they utilized a magnetic position and orientation tracking system to acquire three-dimensional positional and orientation data from cadavers. The presence of skin tissue and active musculature in live human subjects collectively influence the accuracy of bone movement measurements. Consequently, the results of our study may align more with actual *in vivo* expectations.

Veeger's research pursued a dual approach to explore the assumption that the geometric center of rotation equates to the kinematic center. Employing *in vitro* experimentation, Veeger evaluated the kinematic center of the intact glenohumeral joint and the geometric center of the joint based on the morphologies of the humeral head and the glenoid. Veeger demonstrated no significant difference between the two methodologies. Both rotation centers, on average, exhibited a slight medial disposition (-10.5 mm and -9.7 mm) in relation to the anatomical axis (AA), as well as a sub-AAC (below AA) position (-30.1 mm and -32 mm) and an anterior (-25.9 mm and -25.8 mm) placement.

Table 2
Anatomical landmarks, rotation centers and radii for the humeral head and glenoid[a]

Parameter	#1_r			#2_r			#3_r			#4_r			Mean			Std		
	X (mm)	Y (mm)	Z (mm)	X (mm)	Y (mm)	Z (mm)	X (mm)	Y (mm)	Z (mm)	X (mm)	Y (mm)	Z (mm)	X (mm)	Y (mm)	Z (mm)	X (mm)	Y (mm)	Z (mm)
TS	− 149.2	0.0	0.0	− 137.3	0.0	0.0	− 130.6	0.0	0.0	− 126.6	0.0	0.0	− 135.9	0.0	0.0	9.9	0.0	0.0
AI	− 170.2	− 126.1	0.0	− 160.5	− 131.8	0.0	− 155.7	− 136.0	0.0	− 147.0	− 139.9	0.0	− 158.4	− 133.4	0.0	9.7	5.9	0.0
AC	− 10.9	13.8	− 10.9	− 7.3	11.5	− 32.8	− 12.7	1.0	− 26.4	− 1.2	13.6	− 34.2	− 8.0	10.0	− 26.1	5.1	6.1	10.7
PC	− 21.8	− 15.6	− 45.5	− 25.8	− 3.8	− 66.7	− 32.9	− 21.1	− 59.1	− 25.4	− 3.4	− 70.5	− 26.5	− 10.9	− 60.5	4.6	8.8	11.0
Geometric rotation center (e)	− 13.7	− 32.8 (0.5)	− 11.1	− 5.5	− 34.1 (0.7)	− 28.3	− 13.4	− 31.1 (0.3)	− 20.9	− 6.2	− 29.9 (0.5)	− 43.3	− 9.7	− 32.0 (0.5)	− 25.9	4.5	1.9 (0.2)	13.6
Kinematic center from IHA's (e)	− 16.0	− 33.3 (8.0)	− 14.3	− 5.4	− 23.1 (12.9)	− 24.3	− 13.3	− 31.0 (10.3)	− 21.6	− 7.3	− 32.9 (16.5)	− 43.2	− 10.5[b]	− 30.1[b] (11.9)	− 25.8[b]	5.0	4.7 (3.6)	12.3
Radius glenoid		29.9			37.3			26.8			29.1			30.8[c]			4.5	
Radius humeral head		28.1			30.2			23.6			27.3			27.3			2.8	

[a]TS = trigonum spinae, AI = angulus inferior, AC = acromioclavicular joint, processus coracoideus. The geometric rotation center was calculated as the center of a sphere through the glenoid, with a fixed radius based on the radius of the humeral head. The kinematic rotation center is estimated from instantaneous helical axes.
[b]Not significant,
[c]Significant ($P < 0.05$).

Figure 63: Veeger's study results for the humerus COR.

5.2: Comparing the Performance of Each Method

In our study, we explored the accuracy and precision of three distinct methods acromion, midpoint, and centerpoint for COR localization in the context of arm elevation and rotation movements. Our research revealed notable discrepancies, primarily associated with the standard acromion method, especially as arm elevation increased.

The acromion method, which used an offset distance of 4 cm as seen in prior research [86], [93], [94] exhibited high error rates in our study. Several factors may have contributed to this outcome. Most notably, the acromion region was more susceptible to skin artifacts, with their impact growing as the degree of elevation increased [95].

Significantly, the errors associated with the acromion method displayed a bias toward A/P error in the x-axis of the HLCS. When we compared the virtual 3D positioning of the COR, it was evident that the acromion method deviated considerably from the actual center calculated using fluoroscopy.

Conversely, the midpoint method exhibited an inferior shift from the geometric center. This shift can be attributed to its positioning between the greater and lesser tubercles. In contrast, the centerpoint method demonstrated the lowest error rates across most movements. This outcome can be attributed to the centerpoint's placement, situated between the three skin markers affixed to the upper arm region surrounding the humeral head.

Our investigation also uncovered a minor discrepancy in movement speed between the dominant and non-dominant arms, with movements performed by the dominant arm being faster. This observation aligns with previous studies that reported superior temporal performance of the dominant arm in tasks requiring spatial accuracy [96], [97].

One potential explanation for this disparity in movement speed is the association with COR errors. Since skin markers are susceptible to dislocation during rapid movements, the observed higher error rates during faster activities can be attributed to this factor. It's important to note that our study did not control movement speed, and all subjects were right-arm dominant.

Our study underscores the critical importance of method choice for COR localization. The centerpoint method emerges as the most accurate, while variations in movement speed between dominant and non-dominant arms introduce additional complexity to COR measurements.

By examining the acromion, midpoint, and centerpoint methods, we shed light on the variations in accuracy and precision across different anatomical directions (A/P, S/I and M/L). These findings emphasize the significance of considering the method used in COR

measurements, as it profoundly affects the accuracy and precision of results, particularly in joint or body movement analysis.

Furthermore, our findings reveal that both dominant and non-dominant arms experience an increase in error as the arm is elevated or rotated, with a slightly higher error rate in the dominant arm. This highlights the potential impact of arm dominance on COR measurements during weighted abduction and provides valuable insights for researchers and practitioners seeking to enhance measurement reliability and better understand the impact of arm elevation on data quality.

Understanding the dynamics of COR error in relation to arm dominance is essential for researchers and practitioners, enabling them to make informed decisions when interpreting and improving measurement accuracy during different dynamic movements. It underscores the complexity of arm movement dynamics and the need to consider arm dominance when evaluating these measurements, ultimately enhancing the quality of the research work.

5.3: Conclusion

In the dominion of joint center localization, research on the shoulder has remained notably less compared to the lower extremities. This gap in knowledge can be attributed to the intricate nature of the shoulder's motion patterns and the absence of a clear bony landmark to serve as a reference point for the COR. The shoulder, with its wide ROM, is essential for executing complex tasks, making precise kinematic calculations a challenge. Many studies in upper extremity research require an accurate COR for various movements, traditionally relying on fixed geometric joint centers, which, in reality, are far from static positions. The main objective of this study was to develop a reliable

marker-based method for shoulder COR localization, which could be implemented in real-time motion analysis laboratories. We hypothesized that these methods (acromion, midpoint, and centerpoint) would demonstrate minimal error compared to the established gold standard, biplanar fluoroscopy.

Our study revealed the need for improvement in surface-based marker techniques for reliable COR localization, especially in movements involving elevation and rotation. This improvement could offer substantial benefits to clinical gait laboratories, where efficient marker-based motion analysis is crucial. Accurate measurements of the humeral COR play a pivotal role in understanding shoulder kinematics and kinetics, particularly in terms of moment arms and torques [86], [98], [99].

From a biomechanical perspective, the complexity of the shoulder arises from the complex interaction among the shoulder joints, known as shoulder rhythm, and the interactive actions of multiple muscles across various joints during movement. Traditional methods for measuring three-dimensional humeral COR position and motion, such as cadaveric experiments, 2D imaging, static 3D imaging, and invasive techniques, have their inherent limitations.

In our study, we compared a marker-based tracking technique for measuring the three-dimensional humeral COR with the humerus' geometric center as a reference point. It is crucial to note that none of the methods yielded satisfactory results for all movements, with displacement errors significantly increasing as the arm reaches maximum elevation or rotation.

Our study had its limitations, including the impact of skin artifacts and muscle movement on marker placement accuracy (Figure 64). The study's limited sample size and the inability to conduct pilot trials due to radiation concerns also affected our findings. Additionally, the variations in movement speed between dominant and non-dominant arms contributed to disparities in humeral COR errors.

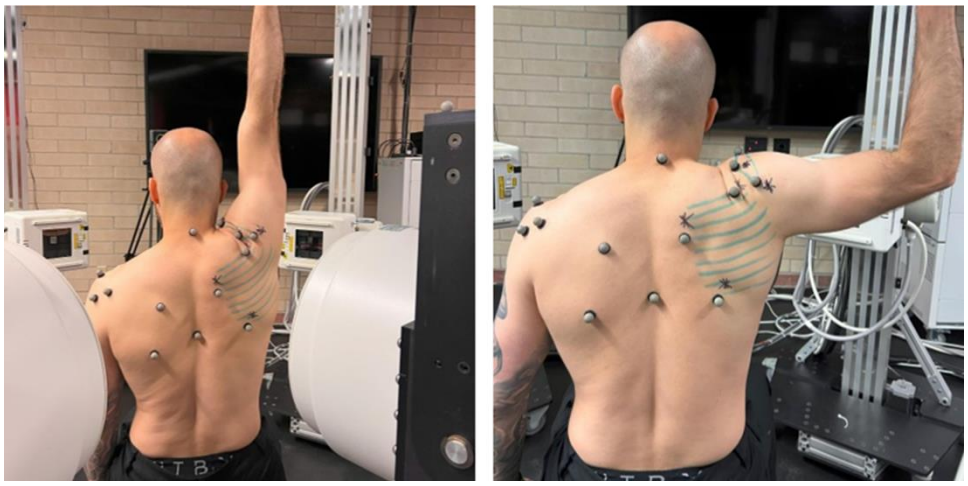

Figure 64: Posterior view for a subject were performing maximum flexion and maximum external rotation at 90°.

The figure above presents the posterior view showing a subject performing in the maximum flexion and external rotation at 90°. This demonstrates the artifacts due to skin movement and the resultant discrepancies in marker displacement relative to the underlying bones. In the figure above the black markers represent the scapular landmarks established through palpation, while the subject’s arm was placed in an abducted configuration, resembling the T-position. Thus, the figure underscores the effect of relative motion between the markers and bone, thus accentuating the impact of arm positioning on marker fidelity and overall measurement accuracy.

Notably, discrepancies in displacement errors were more pronounced for individuals with larger humeral heads (wider humerus) and greater, as indicated in Table 3.

Table 3: Humerus head size from the segmented CT scans.

Subjects	Humeral Head Size (mm)
S1_L	25.95
S1_R	25.77
S2_L	22.36
S2_R	22.84
S3_L	22.96
S3_R	22.78
S4_L	23.89
S4_R	24.10
S5_L	19.47
S5_R	19.52

To summarize, our marker-based tracking approach offers a non-invasive, real-time method for measuring dynamic humeral COR. However, error rates differ across movements and do not necessitate the implantation of tantalum beads. To enhance accuracy, we recommend attaching more markers around the humeral head in a circular pattern or increasing the inferior landmark distance from the fixed acromion markers beyond the 4 cm evaluated in this study. Our research paves the way for future studies on shoulder motion, which could prove beneficial in rehabilitation exercises, sports science, and the evaluation of motion capture system accuracy in estimating shoulder kinematics and humeral COR.

In conclusion, the challenges of shoulder joint center localization are substantial, but our study takes a step toward addressing them. Further research building upon our techniques promises to expand our understanding of shoulder biomechanics and its practical applications.

References

[1] N. Poppen and P. Walker, “Normal and abnormal motion of the shoulder,” *THE JOURNAL OF BONE AND JOINT SURGERY*.

[2] M. Calderone, A. Cereatti, M. Conti, and U. Della Croce, “Comparative evaluation of scapular and humeral coordinate systems based on biomedical images of the glenohumeral joint,” *Journal of Biomechanics*, vol. 47, no. 3, pp. 736–741, Feb. 2014, doi: 10.1016/j.jbiomech.2013.10.045.

[3] C. Panayiotou Charalambous, *The Shoulder Made Easy*. Cham: Springer International Publishing, 2019. doi: 10.1007/978-3-319-98908-2.

[4] A. M. Halder and E. Itoi, “ANATOMY AND BIOMECHANICS OF THE SHOULDER”.

[5] P. Goetti, P. J. Denard, P. Collin, M. Ibrahim, P. Hoffmeyer, and A. Lädermann, “Shoulder biomechanics in normal and selected pathological conditions,” *EFORT Open Reviews*, vol. 5, no. 8, pp. 508–518, Aug. 2020, doi: 10.1302/2058-5241.5.200006.

[6] C. H. Linaker and K. Walker-Bone, “Shoulder disorders and occupation,” *Best Practice & Research Clinical Rheumatology*, vol. 29, no. 3, pp. 405–423, Jun. 2015, doi: 10.1016/j.berh.2015.04.001.

[7] K. Walker-Bone, I. Reading, D. Coggon, C. Cooper, and K. T. Palmer, “The anatomical pattern and determinants of pain in the neck and upper limbs: an epidemiologic study,” *Pain*, vol. 109, no. 1, pp. 45–51, May 2004, doi: 10.1016/j.pain.2004.01.008.

[8] B. Liaghat, J. R. Pedersen, R. S. Husted, L. L. Pedersen, K. Thorborg, and C. B. Juhl, “Diagnosis, prevention and treatment of common shoulder injuries in sport: grading the evidence – a statement paper commissioned by the Danish Society of Sports Physical Therapy (DSSF),” *Br J Sports Med*, vol. 57, no. 7, pp. 408–416, Apr. 2023, doi: 10.1136/bjsports-2022-105674.

[9] M. Alt Murphy and C. K. Häger, “Kinematic analysis of the upper extremity after stroke – how far have we reached and what have we grasped?,” *Physical Therapy Reviews*, vol. 20, no. 3, pp. 137–155, Jun. 2015, doi: 10.1179/1743288X15Y.0000000002.

[10] G. Wu *et al.*, “ISB recommendation on definitions of joint coordinate systems of various joints for the reporting of human joint motion—Part II: shoulder, elbow, wrist and hand,” *Journal of Biomechanics*, vol. 38, no. 5, pp. 981–992, May 2005, doi: 10.1016/j.jbiomech.2004.05.042.

[11] A. Bonnefoy-Mazure, J. Slawinski, A. Riquet, J.-M. Lévèque, C. Miller, and L. Chèze, “Rotation sequence is an important factor in shoulder kinematics. Application to the elite players’ flat serves,” *Journal of Biomechanics*, vol. 43, no. 10, pp. 2022–2025, Jul. 2010, doi: 10.1016/j.jbiomech.2010.03.028.

[12] C. Charbonnier, S. Chagué, F. C. Kolo, J. C. K. Chow, and A. Lädermann, “A patient-specific measurement technique to model shoulder joint kinematics,” *Orthopaedics & Traumatology: Surgery & Research*, vol. 100, no. 7, pp. 715–719, Nov. 2014, doi: 10.1016/j.otsr.2014.06.015.

[13] A. R. Karduna, P. W. McClure, L. A. Michener, and B. Sennett, “Dynamic Measurements of Three-Dimensional Scapular Kinematics: A Validation Study,” *Journal of Biomechanical Engineering*, vol. 123, no. 2, pp. 184–190, Apr. 2001, doi: 10.1115/1.1351892.
[14] M. B. Warner, P. H. Chappell, and M. J. Stokes, “Measuring scapular kinematics during arm lowering using the acromion marker cluster,” *Human Movement Science*, vol. 31, no. 2, pp. 386–396, Apr. 2012, doi: 10.1016/j.humov.2011.07.004.
[15] A. A. Nikooyan, H. E. J. Veeger, P. Westerhoff, F. Graichen, G. Bergmann, and F. C. T. Van Der Helm, “Validation of the Delft Shoulder and Elbow Model using in-vivo glenohumeral joint contact forces,” *Journal of Biomechanics*, vol. 43, no. 15, pp. 3007–3014, Nov. 2010, doi: 10.1016/j.jbiomech.2010.06.015.
[16] J. W. Burke, P. J. Morrow, M. D. J. McNeill, S. M. McDonough, and D. K. Charles, “Vision Based Games for Upper-Limb Stroke Rehabilitation,” in *2008 International Machine Vision and Image Processing Conference*, Portrush, Ireland: IEEE, Sep. 2008, pp. 159–164. doi: 10.1109/IMVIP.2008.16.
[17] M. Khan, M. Schneider, M. Farid, and M. Grzegorzek, “Detection of Infantile Movement Disorders in Video Data Using Deformable Part-Based Model,” *Sensors*, vol. 18, no. 10, p. 3202, Sep. 2018, doi: 10.3390/s18103202.
[18] M. H. Khan, M. Zöller, M. S. Farid, and M. Grzegorzek, “Marker-Based Movement Analysis of Human Body Parts in Therapeutic Procedure,” *Sensors*, vol. 20, no. 11, p. 3312, Jun. 2020, doi: 10.3390/s20113312.
[19] L. Meinecke, N. Breitbach-Faller, C. Bartz, R. Damen, G. Rau, and C. Disselhorst-Klug, “Movement analysis in the early detection of newborns at risk for developing spasticity due to infantile cerebral palsy,” *Human Movement Science*, vol. 25, no. 2, pp. 125–144, Apr. 2006, doi: 10.1016/j.humov.2005.09.012.
[20] A. Saygılı and S. Albayrak, “An efficient and fast computer-aided method for fully automated diagnosis of meniscal tears from magnetic resonance images,” *Artificial Intelligence in Medicine*, vol. 97, pp. 118–130, Jun. 2019, doi: 10.1016/j.artmed.2018.11.008.
[21] M. Topley and J. G. Richards, “A comparison of currently available optoelectronic motion capture systems,” *Journal of Biomechanics*, vol. 106, p. 109820, Jun. 2020, doi: 10.1016/j.jbiomech.2020.109820.
[22] E. Culham and M. Peat, “Functional Anatomy of the Shoulder Complex,” 1993.
[23] R. M. Paine and M. Voight, “The Role of the Scapula,” *J Orthop Sports Phys Ther*, vol. 18, no. 1, pp. 386–391, Jul. 1993, doi: 10.2519/jospt.1993.18.1.386.
[24] S. Yang, T. U. Kim, D. H. Kim, and M. C. Chang, “Understanding the physical examination of the shoulder: a narrative review,” *Ann Palliat Med*, vol. 10, no. 2, pp. 2293–2303, Feb. 2021, doi: 10.21037/apm-20-1808.
[25] J. L. Bellamy, A. E. Johnson, M. J. Beltran, J. R. Hsu, and Skeletal Trauma Research Consortium (STReC), “Quantification of the exposure of the glenohumeral joint from the minimally invasive to more invasive subscapularis approach to the anterior shoulder: a cadaveric study,” *Journal of Shoulder and Elbow Surgery*, vol. 23, no. 6, pp. 895–901, Jun. 2014, doi: 10.1016/j.jse.2013.09.013.

[26] P. Moroder *et al.*, “Characteristics of functional shoulder instability,” *Journal of Shoulder and Elbow Surgery*, vol. 29, no. 1, pp. 68–78, Jan. 2020, doi: 10.1016/j.jse.2019.05.025.
[27] S. Namdari, J. E. Hsu, M. Barron, R. G. Huffman, and D. Glaser, “Immediate Postoperative Radiographs After Shoulder Arthroplasty Are Often Poor Quality and Do Not Alter Care,” *Clinical Orthopaedics & Related Research*, vol. 471, no. 4, pp. 1257–1262, Apr. 2013, doi: 10.1007/s11999-012-2551-9.
[28] A. Carnevale *et al.*, “Wearable systems for shoulder kinematics assessment: a systematic review,” *BMC Musculoskelet Disord*, vol. 20, no. 1, p. 546, Dec. 2019, doi: 10.1186/s12891-019-2930-4.
[29] J. Ovesen and S. Nielsen, “Anterior and posterior shoulder instability: A cadaver study,” *Acta Orthopaedica Scandinavica*, vol. 57, no. 4, pp. 324–327, Jan. 1986, doi: 10.3109/17453678608994402.
[30] D. K. Kuechle, S. R. Newman, E. Itoi, B. F. Morrey, and K.-N. An, “Shoulder muscle moment arms during horizontal flexion and elevation,” *Journal of Shoulder and Elbow Surgery*, vol. 6, no. 5, pp. 429–439, Sep. 1997, doi: 10.1016/S1058-2746(97)70049-1.
[31] M. Fung *et al.*, “Scapular and clavicular kinematics during humeral elevation: A study with cadavers,” *Journal of Shoulder and Elbow Surgery*, vol. 10, no. 3, pp. 278–285, May 2001, doi: 10.1067/mse.2001.114496.
[32] A. R. Karduna, P. J. Kerner, and M. D. Lazarus, “Contact forces in the subacromial space: Effects of scapular orientation,” *Journal of Shoulder and Elbow Surgery*, vol. 14, no. 4, pp. 393–399, Jul. 2005, doi: 10.1016/j.jse.2004.09.001.
[33] R. M. Teece, J. B. Lunden, A. S. Lloyd, A. P. Kaiser, C. J. Cieminski, and P. M. Ludewig, “Three-Dimensional Acromioclavicular Joint Motions During Elevation of the Arm,” *J Orthop Sports Phys Ther*, vol. 38, no. 4, pp. 181–190, Apr. 2008, doi: 10.2519/jospt.2008.2386.
[34] R. U. Hartzler, J. D. Barlow, K.-N. An, and B. T. Elhassan, “Biomechanical effectiveness of different types of tendon transfers to the shoulder for external rotation,” *Journal of Shoulder and Elbow Surgery*, vol. 21, no. 10, pp. 1370–1376, Oct. 2012, doi: 10.1016/j.jse.2012.01.026.
[35] P. Kriechling, S. Roner, F. Liebmann, F. Casari, P. Fürnstahl, and K. Wieser, “Augmented reality for base plate component placement in reverse total shoulder arthroplasty: a feasibility study,” *Arch Orthop Trauma Surg*, vol. 141, no. 9, pp. 1447–1453, Sep. 2021, doi: 10.1007/s00402-020-03542-z.
[36] A. Cereatti, C. Rosso, A. Nazarian, J. P. DeAngelis, A. J. Ramappa, and U. D. Croce, “Scapular Motion Tracking Using Acromion Skin Marker Cluster: In Vitro Accuracy Assessment,” *J. Med. Biol. Eng.*, vol. 35, no. 1, pp. 94–103, Feb. 2015, doi: 10.1007/s40846-015-0010-2.
[37] R. C. Rhoad *et al.*, “A new in vivo technique for three-dimensional shoulder kinematics analysis,” *Skeletal Radiology*, vol. 27, no. 2, pp. 92–97, Feb. 1998, doi: 10.1007/s002560050344.
[38] B. Marquardt, C. Hurschler, J. Schneppendahl, K.-A. Witt, W. Pötzl, and J. Steinbeck, “Quantitative Assessment of Glenohumeral Translation after Anterior

Shoulder Dislocation and Subsequent Arthroscopic Bankart Repair," *Am J Sports Med*, vol. 34, no. 11, pp. 1756–1762, Nov. 2006, doi: 10.1177/0363546506289702.
[39] G. Moatshe *et al.*, "Qualitative and Quantitative Anatomy of the Proximal Humerus Muscle Attachments and the Axillary Nerve: A Cadaveric Study," *Arthroscopy: The Journal of Arthroscopic & Related Surgery*, vol. 34, no. 3, pp. 795–803, Mar. 2018, doi: 10.1016/j.arthro.2017.08.301.
[40] S. Gyftopoulos, K. E. Guja, N. Subhas, M. S. Virk, and H. T. Gold, "Cost-effectiveness of magnetic resonance imaging versus ultrasound for the detection of symptomatic full-thickness supraspinatus tendon tears," *Journal of Shoulder and Elbow Surgery*, vol. 26, no. 12, pp. 2067–2077, Dec. 2017, doi: 10.1016/j.jse.2017.07.012.
[41] J. A. Strakowski and C. J. Visco, "Diagnostic and therapeutic musculoskeletal ultrasound applications of the shoulder," *Muscle Nerve*, p. mus.26505, May 2019, doi: 10.1002/mus.26505.
[42] M. Refaat, A. Torky, W. Salah El Deen, and S. Soliman, "Comparing Efficacy of Shoulder Ultrasound and Magnetic Resonance Imaging in Shoulder Impingement.," *Benha Medical Journal*, vol. 0, no. 0, pp. 0–0, Dec. 2020, doi: 10.21608/bmfj.2020.130630.
[43] C. Leitner *et al.*, "Ultrasound as a Tool to Study Muscle–Tendon Functions during Locomotion: A Systematic Review of Applications," *Sensors*, vol. 19, no. 19, p. 4316, Oct. 2019, doi: 10.3390/s19194316.
[44] I. Beggs, "Shoulder Ultrasound," *Seminars in Ultrasound, CT and MRI*, vol. 32, no. 2, pp. 101–113, Apr. 2011, doi: 10.1053/j.sult.2010.10.003.
[45] S. Huang, S. Liu, H. Tang, T. Wei, W. Wang, and C. Yang, "Relationship between severity of shoulder subluxation and soft-tissue injury in hemiplegic stroke patients," *J Rehabil Med*, vol. 44, no. 9, pp. 733–739, 2012, doi: 10.2340/16501977-1026.
[46] A. A. Daghir, P. A. Sookur, S. Shah, and M. Watson, "Dynamic ultrasound of the subacromial–subdeltoid bursa in patients with shoulder impingement: a comparison with normal volunteers," *Skeletal Radiol*, vol. 41, no. 9, pp. 1047–1053, Sep. 2012, doi: 10.1007/s00256-011-1295-z.
[47] R. J. Wakefield *et al.*, "Musculoskeletal Ultrasound Including Definitions for Ultrasonographic Pathology," *Musculoskeletal ultrasound*, p. 3.
[48] B. Aminzadeh, S. Najafi, A. Moradi, B. Abbasi, D. Farrokh, and M. Emadzadeh, "Evaluation of Diagnostic Precision of Ultrasound for Rotator Cuff Disorders in Patients with Shoulder Pain," *ABJS*, no. Online First, Sep. 2020, doi: 10.22038/abjs.2020.42894.2166.
[49] G. M. Allen and D. J. Wilson, "Ultrasound of the shoulder," *European Journal of Ultrasound*, p. 7, 2001.
[50] P. W. McClure, L. A. Michener, B. J. Sennett, and A. R. Karduna, "Direct 3-dimensional measurement of scapular kinematics during dynamic movements in vivo," *Journal of Shoulder and Elbow Surgery*, vol. 10, no. 3, pp. 269–277, May 2001, doi: 10.1067/mse.2001.112954.

[51] C. Maiwald, A. Arndt, C. Nester, R. Jones, A. Lundberg, and P. Wolf, “The effect of intracortical bone pin application on kinetics and tibiocalcaneal kinematics of walking gait,” *Gait & Posture*, vol. 52, pp. 129–134, Feb. 2017, doi: 10.1016/j.gaitpost.2016.10.023.
[52] M. Hajizadeh, B. Michaud, and M. Begon, “The effect of intracortical bone pin on shoulder kinematics during dynamic activities,” *International Biomechanics*, vol. 6, no. 1, pp. 47–53, Jan. 2019, doi: 10.1080/23335432.2019.1633958.
[53] K. Ito *et al.*, “Direct assessment of 3D foot bone kinematics using biplanar X-ray fluoroscopy and an automatic model registration method,” *J Foot Ankle Res*, vol. 8, no. 1, p. 21, Dec. 2015, doi: 10.1186/s13047-015-0079-4.
[54] V. Kefala, “Assessment of Normal Knee Kinematics Using High-Speed Stereo-Radiography System”.
[55] J. C. I. Iv, “Design of the High-Speed Stereo Radiography System”.
[56] M. J. Bey, R. Zauel, S. K. Brock, and S. Tashman, “Validation of a New Model-Based Tracking Technique for Measuring Three-Dimensional, In Vivo Glenohumeral Joint Kinematics,” *Journal of Biomechanical Engineering*, vol. 128, no. 4, pp. 604–609, Aug. 2006, doi: 10.1115/1.2206199.
[57] M. J. Bey, S. K. Brock, W. N. Beierwaltes, R. Zauel, P. A. Kolowich, and T. R. Lock, “In vivo measurement of subacromial space width during shoulder elevation: Technique and preliminary results in patients following unilateral rotator cuff repair,” *Clinical Biomechanics*, vol. 22, no. 7, pp. 767–773, Aug. 2007, doi: 10.1016/j.clinbiomech.2007.04.006.
[58] J. E. Giphart, J. P. Brunkhorst, N. H. Horn, K. B. Shelburne, M. R. Torry, and P. J. Millett, “Effect of Plane of Arm Elevation on Glenohumeral Kinematics: A Normative Biplane Fluoroscopy Study,” *Journal of Bone and Joint Surgery*, vol. 95, no. 3, pp. 238–245, Feb. 2013, doi: 10.2106/JBJS.J.01875.
[59] T. Kijima *et al.*, “In vivo 3-dimensional analysis of scapular and glenohumeral kinematics: comparison of symptomatic or asymptomatic shoulders with rotator cuff tears and healthy shoulders,” *Journal of Shoulder and Elbow Surgery*, vol. 24, no. 11, pp. 1817–1826, Nov. 2015, doi: 10.1016/j.jse.2015.06.003.
[60] T. G. Baumer *et al.*, “Effects of Rotator Cuff Pathology and Physical Therapy on In Vivo Shoulder Motion and Clinical Outcomes in Patients With a Symptomatic Full-Thickness Rotator Cuff Tear,” *Orthopaedic Journal of Sports Medicine*, vol. 4, no. 9, p. 232596711666650, Sep. 2016, doi: 10.1177/2325967116666506.
[61] R. L. Lawrence, R. Zauel, and M. J. Bey, “Measuring 3D In-vivo Shoulder Kinematics using Biplanar Videoradiography,” *JoVE*, no. 169, p. 62210, Mar. 2021, doi: 10.3791/62210.
[62] J. E. Giphart, O. A. J. Van Der Meijden, and P. J. Millett, “The effects of arm elevation on the 3-dimensional acromiohumeral distance: a biplane fluoroscopy study with normative data,” *Journal of Shoulder and Elbow Surgery*, vol. 21, no. 11, pp. 1593–1600, Nov. 2012, doi: 10.1016/j.jse.2011.11.023.
[63] R. L. Lawrence, J. P. Braman, and P. M. Ludewig, “Shoulder kinematics impact subacromial proximities: a review of the literature,” *Brazilian Journal of Physical Therapy*, vol. 24, no. 3, pp. 219–230, May 2020, doi: 10.1016/j.bjpt.2019.07.009.

[64] S. Guan, H. A. Gray, F. Keynejad, and M. G. Pandy, “Mobile Biplane X-Ray Imaging System for Measuring 3D Dynamic Joint Motion During Overground Gait,” *IEEE Trans. Med. Imaging*, vol. 35, no. 1, pp. 326–336, Jan. 2016, doi: 10.1109/TMI.2015.2473168.
[65] B. Hingtgen, J. R. McGuire, M. Wang, and G. F. Harris, “An upper extremity kinematic model for evaluation of hemiparetic stroke,” *Journal of Biomechanics*, vol. 39, no. 4, pp. 681–688, 2006, doi: 10.1016/j.jbiomech.2005.01.008.
[66] B. Galna, G. Barry, D. Jackson, D. Mhiripiri, P. Olivier, and L. Rochester, “Accuracy of the Microsoft Kinect sensor for measuring movement in people with Parkinson’s disease,” *Gait & Posture*, vol. 39, no. 4, pp. 1062–1068, Apr. 2014, doi: 10.1016/j.gaitpost.2014.01.008.
[67] C. Park *et al.*, “Comparative accuracy of a shoulder range motion measurement sensor and Vicon 3D motion capture for shoulder abduction in frozen shoulder,” *THC*, vol. 30, pp. 251–257, Feb. 2022, doi: 10.3233/THC-228024.
[68] C. Gu, W. Lin, X. He, L. Zhang, and M. Zhang, “IMU-based motion capture system for rehabilitation applications: A systematic review,” *Biomimetic Intelligence and Robotics*, vol. 3, no. 2, p. 100097, Jun. 2023, doi: 10.1016/j.birob.2023.100097.
[69] A. Cereatti *et al.*, “Standardization proposal of soft tissue artefact description for data sharing in human motion measurements,” *Journal of Biomechanics*, vol. 62, pp. 5–13, Sep. 2017, doi: 10.1016/j.jbiomech.2017.02.004.
[70] B. Carse, B. Meadows, R. Bowers, and P. Rowe, “Affordable clinical gait analysis: An assessment of the marker tracking accuracy of a new low-cost optical 3D motion analysis system,” *Physiotherapy*, vol. 99, no. 4, pp. 347–351, Dec. 2013, doi: 10.1016/j.physio.2013.03.001.
[71] P. Merriaux, Y. Dupuis, R. Boutteau, P. Vasseur, and X. Savatier, “A Study of Vicon System Positioning Performance,” *Sensors*, vol. 17, no. 7, p. 1591, Jul. 2017, doi: 10.3390/s17071591.
[72] H. L. Mjøsund, E. Boyle, P. Kjaer, R. M. Mieritz, T. Skallgård, and P. Kent, “Clinically acceptable agreement between the ViMove wireless motion sensor system and the Vicon motion capture system when measuring lumbar region inclination motion in the sagittal and coronal planes,” *BMC Musculoskelet Disord*, vol. 18, no. 1, p. 124, Dec. 2017, doi: 10.1186/s12891-017-1489-1.
[73] D. Pagliari and L. Pinto, “Calibration of Kinect for Xbox One and Comparison between the Two Generations of Microsoft Sensors,” *Sensors*, vol. 15, no. 11, pp. 27569–27589, Oct. 2015, doi: 10.3390/s151127569.
[74] M. Windolf, N. Götzen, and M. Morlock, “Systematic accuracy and precision analysis of video motion capturing systems—exemplified on the Vicon-460 system,” *Journal of Biomechanics*, vol. 41, no. 12, pp. 2776–2780, Aug. 2008, doi: 10.1016/j.jbiomech.2008.06.024.
[75] D. L. Miranda, M. J. Rainbow, J. J. Crisco, and B. C. Fleming, “Kinematic differences between optical motion capture and biplanar videoradiography during a jump–cut maneuver,” *Journal of Biomechanics*, vol. 46, no. 3, pp. 567–573, Feb. 2013, doi: 10.1016/j.jbiomech.2012.09.023.

[76] S. E. Kessler *et al.*, "A Direct Comparison of Biplanar Videoradiography and Optical Motion Capture for Foot and Ankle Kinematics," *Front. Bioeng. Biotechnol.*, vol. 7, p. 199, Aug. 2019, doi: 10.3389/fbioe.2019.00199.
[77] D. R. Hume, V. Kefala, M. D. Harris, and K. B. Shelburne, "Comparison of Marker-Based and Stereo Radiography Knee Kinematics in Activities of Daily Living," *Ann Biomed Eng*, vol. 46, no. 11, pp. 1806–1815, Nov. 2018, doi: 10.1007/s10439-018-2068-9.
[78] G. Rab, K. Petuskey, and A. Bagley, "A method for determination of upper extremity kinematics," *Gait & Posture*, vol. 15, no. 2, pp. 113–119, Apr. 2002, doi: 10.1016/S0966-6362(01)00155-2.
[79] L. D. Hamilton, T. E. Andreassen, C. A. Myers, K. B. Shelburne, C. W. Clary, and P. J. Rullkoetter, "Knee pivot location in asymptomatic older adults," *Journal of Biomechanics*, vol. 149, p. 111487, Mar. 2023, doi: 10.1016/j.jbiomech.2023.111487.
[80] S. Schreven, P. J. Beek, and J. B. J. Smeets, "Optimising filtering parameters for a 3D motion analysis system," *Journal of Electromyography and Kinesiology*, vol. 25, no. 5, pp. 808–814, Oct. 2015, doi: 10.1016/j.jelekin.2015.06.004.
[81] L. Cai, D. Liu, and Y. Ma, "Placement Recommendations for Single Kinect-Based Motion Capture System in Unilateral Dynamic Motion Analysis," *Healthcare*, vol. 9, no. 8, p. 1076, Aug. 2021, doi: 10.3390/healthcare9081076.
[82] S. Cizmeciogullart, S. Mihcin, A. Akan, Y. Keskin, B. Urkmez, and T. Aydin, "Cut-off Frequency Estimation Methods for Biomechanical Data Filtering," in *2018 Medical Technologies National Congress (TIPTEKNO)*, Magusa: IEEE, Nov. 2018, pp. 1–4. doi: 10.1109/TIPTEKNO.2018.8596916.
[83] T. E. Andreassen *et al.*, "Apparatus for In Vivo Knee Laxity Assessment Using High-Speed Stereo Radiography," *Journal of Medical Devices*, vol. 15, no. 4, p. 041004, Dec. 2021, doi: 10.1115/1.4051834.
[84] Y. Chu, J. Akins, M. Lovalekar, S. Tashman, S. Lephart, and T. Sell, "Validation of a video-based motion analysis technique in 3-D dynamic scapular kinematic measurements," *Journal of Biomechanics*, vol. 45, no. 14, pp. 2462–2466, Sep. 2012, doi: 10.1016/j.jbiomech.2012.06.025.
[85] K. J. McQuade and G. L. Smidt, "Dynamic Scapulohumeral Rhythm: The Effects of External Resistance During Elevation of the Arm in the Scapular Plane," *J Orthop Sports Phys Ther*, vol. 27, no. 2, pp. 125–133, Feb. 1998, doi: 10.2519/jospt.1998.27.2.125.
[86] M. E. Hahn, "Locating the shoulder joint center in relation to the humeral epicondyles: a novel prediction technique," Master of Science, Iowa State University, 2000. doi: 10.31274/rtd-20201118-210.
[87] K. Petuskey, A. Bagley, E. Abdala, M. A. James, and G. Rab, "Upper extremity kinematics during functional activities: Three-dimensional studies in a normal pediatric population," *Gait & Posture*, vol. 25, no. 4, pp. 573–579, Apr. 2007, doi: 10.1016/j.gaitpost.2006.06.006.

[88] N. Matsumura *et al.*, “Three-dimensional alignment changes of the shoulder girdle between the supine and standing positions,” *J Orthop Surg Res*, vol. 15, no. 1, p. 411, Dec. 2020, doi: 10.1186/s13018-020-01934-w.
[89] S. Tashman and W. Anderst, “In-Vivo Measurement of Dynamic Joint Motion Using High Speed Biplane Radiography and CT: Application to Canine ACL Deficiency,” *Journal of Biomechanical Engineering*, vol. 125, no. 2, pp. 238–245, Apr. 2003, doi: 10.1115/1.1559896.
[90] C. G. M. Meskers, F. C. T. Van Der Helm, L. A. Rozendaal, and P. M. Rozing, “In vivo estimation of the glenohumeral joint rotation center from scapular bony landmarks by linear regression,” *Journal of Biomechanics*, vol. 31, no. 1, pp. 93–96, Nov. 1997, doi: 10.1016/S0021-9290(97)00101-2.
[91] A. Patra, M. Singh, H. Kaur, R. K. Singla, and V. Malhotra, “Re-definition of position and calculation of safe area for axillary nerve in deltoid muscle with its clinical relevance: a cadaveric study,” *Anat Cell Biol*, vol. 51, no. 2, p. 93, 2018, doi: 10.5115/acb.2018.51.2.93.
[92] H. E. J. Veeger, “The position of the rotation center of the glenohumeral joint,” *Journal of Biomechanics*, vol. 33, no. 12, pp. 1711–1715, Dec. 2000, doi: 10.1016/S0021-9290(00)00141-X.
[93] J. Howenstein, K. Kipp, and M. Sabick, “Peak horizontal ground reaction forces and impulse correlate with segmental energy flow in youth baseball pitchers,” *Journal of Biomechanics*, vol. 108, p. 109909, Jul. 2020, doi: 10.1016/j.jbiomech.2020.109909.
[94] J. Howenstein, C. LeVasseur, and M. B. Sabick, “Testing of a Functional Glenohumeral Joint Center Location Method to Improve Shoulder Angle Quantification in Elevated Arm Positions”.
[95] Y. Miura *et al.*, “Three-dimensional Scapular Kinematics During Arm Elevation in Massive Rotator Cuff Tear Patients,” *PRM*, vol. 2, no. 0, p. n/a, 2017, doi: 10.2490/prm.20170005.
[96] N. Gueugneau, B. Mauvieux, and C. Papaxanthis, “Circadian Modulation of Mentally Simulated Motor Actions: Implications for the Potential Use of Motor Imagery in Rehabilitation,” *Neurorehabil Neural Repair*, vol. 23, no. 3, pp. 237–245, Mar. 2009, doi: 10.1177/1545968308321775.
[97] P. Gandrey, C. Paizis, V. Karathanasis, N. Gueugneau, and C. Papaxanthis, “Dominant vs. nondominant arm advantage in mentally simulated actions in right handers,” *Journal of Neurophysiology*, vol. 110, no. 12, pp. 2887–2894, Dec. 2013, doi: 10.1152/jn.00123.2013.
[98] D. C. Ackland, P. Pak, M. Richardson, and M. G. Pandy, “Moment arms of the muscles crossing the anatomical shoulder,” *Journal of Anatomy*, vol. 213, no. 4, pp. 383–390, Oct. 2008, doi: 10.1111/j.1469-7580.2008.00965.x.
[99] F. Hik and D. C. Ackland, “The moment arms of the muscles spanning the glenohumeral joint: a systematic review,” *J. Anat.*, vol. 234, no. 1, pp. 1–15, Jan. 2019, doi: 10.1111/joa.12903.

Appendix

Table 4: COR Errors and their resultants values for the abduction movement at the minimum and maximum elevation angle.

Subject-1-Right Arm												
Abduction	Acromion				Center Point				MidPoint			
Angle	A/P	S/I	M/L	Resultant	A/P	S/I	M/L	Resultant	A/P	S/I	M/L	Resultant
Min	-5.4	26.41	-6.55	27.74	-4.1	9.12	9.22	13.61	20.63	-6.3	33.92	40.2
Max	58.61	16.99	30.97	68.43	53.7	-36.09	7.21	65.11	33.32	-37.61	30.31	58.68
Subject-2-Right Arm												
Angle	A/P	S/I	M/L	Resultant	A/P	S/I	M/L	Resultant	A/P	S/I	M/L	Resultant
Min	-8.25	31.52	-2.77	32.7	-5.71	13.46	16.88	22.34	24.26	2.88	28.45	37.5
Max	41.17	19.64	21.58	50.47	44.77	-39.21	8.38	60.1	44.63	-33.69	28.14	62.6
Subject-3-Right Arm												
Angle	A/P	S/I	M/L	Resultant	A/P	S/I	M/L	Resultant	A/P	S/I	M/L	Resultant
Min	5.15	-4.19	17.84	19.04	9.13	3.71	15.26	18.16	15.66	-3.22	27.83	32.09
Max	34.91	19.85	15.66	43.1	29.65	-36.83	8.72	48.08	31.25	-31.34	22.8	49.78
Subject-4-Right Arm												
Angle	A/P	S/I	M/L	Resultant	A/P	S/I	M/L	Resultant	A/P	S/I	M/L	Resultant
Min	15.81	-2.83	-11.23	19.6	12.63	-1.65	-4.33	13.46	11.74	-21.45	15.04	28.71
Max	55.79	4.19	-0.03	55.95	43.35	-34.34	-11.19	56.43	30.04	-31.33	13.64	45.5
Subject-5-Right Arm												
Angle	A/P	S/I	M/L	Resultant	A/P	S/I	M/L	Resultant	A/P	S/I	M/L	Resultant
Min	4.89	7.94	-6.06	9	17.34	6.39	-4.67	18.35	25.68	-9.09	3.91	27.31
Max	41.16	10.24	-5.15	42.35	27.99	-27.09	-10.8	38.81	20.88	-29.14	7.51	35.95
Subject-1-Left Arm												
Abduction	Acromion				Center Point				MidPoint			
Angle	A/P	S/I	M/L	Resultant	A/P	S/I	M/L	Resultant	A/P	S/I	M/L	Resultant
Min	-13.9	12.54	1.02	18.75	-20.77	-8.33	-13.06	25.92	-1.63	-32.82	-27	42.53
Max	46.96	29.66	-40.08	68.49	37.83	-11.11	-1.59	39.46	24.08	-18.87	-21.85	37.59
Subject-2-Left Arm												
Angle	A/P	S/I	M/L	Resultant	A/P	S/I	M/L	Resultant	A/P	S/I	M/L	Resultant
Min	-7.79	19.53	-6.24	21.94	-7.36	4.67	-19.13	21.02	14.09	-1.88	-34.08	36.93
Max	44.12	20.64	-23.08	53.9	42.17	-34.68	-6.07	54.94	41.46	-30.2	-26.89	57.91
Subject-3-Left Arm												
Angle	A/P	S/I	M/L	Resultant	A/P	S/I	M/L	Resultant	A/P	S/I	M/L	Resultant
Min	0.09	-3.69	-22.22	22.52	2.48	1.7	-16.59	16.86	9.7	-2.85	-29.06	30.77
Max	26.54	25.77	-34.64	50.68	30.24	-26.32	-22.02	45.74	27	-22.09	-38	51.58
Subject-4-Left Arm												
Angle	A/P	S/I	M/L	Resultant	A/P	S/I	M/L	Resultant	A/P	S/I	M/L	Resultant
Min	10.68	1.24	10.29	14.89	12.07	2.96	2.38	12.65	12.37	-8.91	-17.22	23
Max	48.53	19.45	-11.39	53.51	44.93	-26.1	1.06	51.97	35.61	-17.77	-21.27	45.12
Subject-5-Left Arm												
Angle	A/P	S/I	M/L	Resultant	A/P	S/I	M/L	Resultant	A/P	S/I	M/L	Resultant
Min	-2.85	21.07	-0.48	21.27	8.59	16.91	-5.37	19.71	24.66	8.68	-10.93	28.34
Max	46.76	9.45	-7.84	48.35	33.66	-37.97	-3.91	50.89	26.82	-33.6	-19.39	47.16

Table 5: COR Errors and their resultants values for the abduction/weight movement at the minimum and maximum elevation angle.

Subject-1-Right Arm												
Abduction /Weight	Acromion				Center Point				MidPoint			
Angle	A/P	S/I	M/L	Resultant	A/P	S/I	M/L	Resultant	A/P	S/I	M/L	Resultant
Min	-3.9	26.5	-8.66	28.16	-5	9.94	8.32	13.89	21.28	-4.05	32.86	39.36
Max	63.81	13.71	26.85	70.58	52.44	-38.73	2.57	65.24	33.39	-39.96	26.05	58.23
Subject-2-Right Arm												
Angle	A/P	S/I	M/L	Resultant	A/P	S/I	M/L	Resultant	A/P	S/I	M/L	Resultant
Min	-14.32	28.56	3.18	32.11	-8.48	10.57	20.52	24.59	23.53	1.96	28.8	37.24
Max	42.62	13.31	24.11	50.75	37.96	-48.06	13.47	62.71	38.56	-40.2	33.37	64.93
Subject-3-Right Arm												
Angle	A/P	S/I	M/L	Resultant	A/P	S/I	M/L	Resultant	A/P	S/I	M/L	Resultant
Min	6.56	-3.43	15.94	17.57	8.62	5.05	15.78	18.68	15.12	-1.47	28.21	32.04
Max	27.7	23.29	21.64	42.17	36.98	-31.13	10.96	49.56	37.19	-27.6	25.05	52.65
Subject-4-Right Arm												
Angle	A/P	S/I	M/L	Resultant	A/P	S/I	M/L	Resultant	A/P	S/I	M/L	Resultant
Min	21.08	5.14	-7.27	22.88	18.53	7.6	-1.08	20.06	14.14	-8.29	20.17	25.99
Max	54.78	7.16	7.01	55.69	42.61	-34.05	-1.22	54.55	25.2	-29.89	20.37	44.08
Subject-5-Right Arm												
Angle	A/P	S/I	M/L	Resultant	A/P	S/I	M/L	Resultant	A/P	S/I	M/L	Resultant
Min	12.43	9.13	-3.27	15.31	12.39	16.78	2.56	20.92	21.95	6.49	15.51	23.23
Max	42.42	12.88	-2.1	44.31	29.48	-24.81	-5.31	38.47	18.3	-27.75	10.79	33.41
Subject-1-Left Arm												
Abduction /Weight	Acromion				Center Point				MidPoint			
Angle	A/P	S/I	M/L	Resultant	A/P	S/I	M/L	Resultant	A/P	S/I	M/L	Resultant
Min	-13.21	9.44	3.63	16.64	-16.69	-10.64	-8.06	21.37	0.58	-30.63	-29.64	42.62
Max	60.22	23.1	-34.75	73.26	37.59	-16.75	4.05	41.35	28.66	-24.63	-17.71	41.74
Subject-2-Left Arm												
Angle	A/P	S/I	M/L	Resultant	A/P	S/I	M/L	Resultant	A/P	S/I	M/L	Resultant
Min	-10.05	16.71	-5.14	20.17	-12.3	1.49	-17.87	21.75	10.08	-3.55	-34.01	35.65
Max	44.41	16.74	-27.26	54.73	41.68	-39.43	-9.6	58.18	37.78	-33.93	-30.33	59.15
Subject-3-Left Arm												
Angle	A/P	S/I	M/L	Resultant	A/P	S/I	M/L	Resultant	A/P	S/I	M/L	Resultant
Min	-7.41	-2.07	-21.82	23.13	-6.19	3.96	-15.53	17.18	-5.64	0.42	-30.22	30.75
Max	28.27	26.44	-34.5	51.85	32.95	-25.62	-19.12	45.91	31.81	-21.67	-35.51	52.37
Subject-4-Left Arm												
Angle	A/P	S/I	M/L	Resultant	A/P	S/I	M/L	Resultant	A/P	S/I	M/L	Resultant
Min	10.71	-11.57	2.63	15.99	12.45	-9.15	-1.99	15.58	10.76	-20.27	-21.9	31.72
Max	50.25	19.98	-18.54	57.16	43.17	-28.61	-10.21	52.78	30.11	-16.53	-28.61	44.7
Subject-5-Left Arm												
Angle	A/P	S/I	M/L	Resultant	A/P	S/I	M/L	Resultant	A/P	S/I	M/L	Resultant
Min	-5.41	18.92	0.6	19.69	1.27	17.98	-5.96	18.99	18.53	13.34	-13.6	26.57
Max	46.09	11.24	-4.7	47.67	34.39	-34.87	1.21	48.99	28.57	-33.1	-14.97	46.22

Table 6: COR Errors and their resultants values for the flexion movement at minimum and maximum elevation angle.

Subject-1-Right Arm												
Flexion	Acromion				Center Point				MidPoint			
Angle	A/P	S/I	M/L	Resultant	A/P	S/I	M/L	Resultant	A/P	S/I	M/L	Resultant
Min	7.36	23.03	-11.55	26.8	-7.63	6.54	-3.25	10.56	-17.76	-7.48	30.09	35.73
Max	64.19	15.72	-2.56	66.14	45.46	-39.07	-0.15	59.94	25.59	-36.21	26.28	51.54
Subject-2-Right Arm												
Angle	A/P	S/I	M/L	Resultant	A/P	S/I	M/L	Resultant	A/P	S/I	M/L	Resultant
Min	-15.78	33.2	-12.37	38.78	-23.34	15.62	9.28	29.58	5.09	11.73	34.24	36.55
Max	41.63	15.53	12.67	46.21	38.45	-46.56	7.8	60.88	41.3	-39.13	26.55	62.78
Subject-3-Right Arm												
Angle	A/P	S/I	M/L	Resultant	A/P	S/I	M/L	Resultant	A/P	S/I	M/L	Resultant
Min	-9.74	-7.47	13.19	18.01	-6.34	0.2	13.22	14.67	-10.39	-6.1	26.66	29.26
Max	21.24	14.62	-13.18	28.96	17.63	-32.81	-3.17	37.38	21.27	-29.18	11.79	37.99
Subject-4-Right Arm												
Angle	A/P	S/I	M/L	Resultant	A/P	S/I	M/L	Resultant	A/P	S/I	M/L	Resultant
Min	24.69	-0.6	7.84	25.92	12.88	4.29	5.18	14.53	1.93	-12.63	24.39	27.54
Max	53.8	2.61	2.99	53.94	41.9	-38.62	-11.67	58.17	29.5	-35.11	13.38	47.77
Subject-5-Right Arm												
Angle	A/P	S/I	M/L	Resultant	A/P	S/I	M/L	Resultant	A/P	S/I	M/L	Resultant
Min	4.4	15.78	2.81	16.47	1.2	19.75	4.34	19.89	-0.5	13.64	21.69	14.42
Max	41.38	8.44	4.61	42.29	30.28	-29.36	-3.42	42.13	20.69	-30.96	13.77	37.42
Subject-1-Left Arm												
Flexion	Acromion				Center Point				MidPoint			
Angle	A/P	S/I	M/L	Resultant	A/P	S/I	M/L	Resultant	A/P	S/I	M/L	Resultant
Min	-7.51	17.37	15.22	24.29	-15.99	-5.37	14.57	22.29	-24.27	-20.76	-16.27	35.85
Max	63.76	11.94	-28.73	70.94	38.12	-33.53	-3.47	50.88	26.51	-31.92	-28.35	50.26
Subject-2-Left Arm												
Angle	A/P	S/I	M/L	Resultant	A/P	S/I	M/L	Resultant	A/P	S/I	M/L	Resultant
Min	-1.89	11.09	12.32	16.69	-14.68	-2.45	3.92	15.39	-15.48	-5.47	-22.29	27.68
Max	44.78	19.96	-11.28	50.31	36.3	-38.16	-9.17	53.45	37.85	-28.77	-29.16	55.78
Subject-3-Left Arm												
Angle	A/P	S/I	M/L	Resultant	A/P	S/I	M/L	Resultant	A/P	S/I	M/L	Resultant
Min	-15.84	5.6	-6.04	17.85	-1.74	3.23	-8.58	9.33	-7.15	-2.48	-20.87	22.2
Max	31.91	21.81	5.96	39.11	30.67	-26.47	-6.86	41.09	34.22	-18.75	-20.85	44.24
Subject-4-Left Arm												
Angle	A/P	S/I	M/L	Resultant	A/P	S/I	M/L	Resultant	A/P	S/I	M/L	Resultant
Min	5.48	-13.16	-5.72	15.36	2.82	-8.93	-4	10.18	-12.36	-20.65	-16.06	28.94
Max	52.02	16.58	-28.44	61.56	43.78	-27.63	-8.02	52.39	33.32	-17.3	-29.92	48.01
Subject-5-Left Arm												
Angle	A/P	S/I	M/L	Resultant	A/P	S/I	M/L	Resultant	A/P	S/I	M/L	Resultant
Min	-5.53	20.45	7.92	22.61	-5.73	19.07	1.51	19.97	4.77	16.98	-15.62	23.56
Max	48.74	7.27	-5.1	49.54	33.04	-35.96	-0.91	48.84	28.97	-31.09	-17.47	45.94

Table 7: COR Errors and their resultants values for the external rotation at 90° movement at the minimum and maximum elevation angle.

Subject-1-Right Arm												
IE at 90°	Acromion				Center Point				MidPoint			
Angle	A/P	S/I	M/L	Resultant	A/P	S/I	M/L	Resultant	A/P	S/I	M/L	Resultant
Min	-8.94	32.72	5.46	34.35	-9.39	-5.11	11.64	15.81	-22.04	-28.27	14.16	38.54
Max	-8.46	35.33	7.94	37.19	7.23	-1.61	9.65	12.16	22.7	-27.42	24.81	43.39
Subject-2-Right Arm												
Angle	A/P	S/I	M/L	Resultant	A/P	S/I	M/L	Resultant	A/P	S/I	M/L	Resultant
Min	-24.16	28.05	-10.68	38.53	-20.7	-4.36	2.32	21.28	-14.23	-11.97	29.22	34.64
Max	-6.89	32.82	26.56	42.78	12.52	0.61	16.64	20.84	35.31	-9.36	17.74	40.61
Subject-3-Right Arm												
Angle	A/P	S/I	M/L	Resultant	A/P	S/I	M/L	Resultant	A/P	S/I	M/L	Resultant
Min	-5.03	6.8	4.55	9.6	-16.25	-5.16	23.96	29.41	-25.82	-10.52	29.48	40.58
Max	5.98	7.16	10.22	13.84	31.99	-4.46	9.8	33.75	39.13	-10.07	18.05	44.25
Subject-4-Right Arm												
Angle	A/P	S/I	M/L	Resultant	A/P	S/I	M/L	Resultant	A/P	S/I	M/L	Resultant
Min	16.16	26.99	9.4	32.84	6.22	5.57	16.15	18.18	-5.4	-13.12	17.45	22.49
Max	-4.13	23.83	-13.81	27.85	12.14	5.73	-10.97	17.34	18.79	-13.61	2.35	23.32
Subject-5-Right Arm												
Angle	A/P	S/I	M/L	Resultant	A/P	S/I	M/L	Resultant	A/P	S/I	M/L	Resultant
Min	5.29	22.55	2.54	23.22	-2.57	8.72	18.84	10.07	-9.63	-4.98	26.95	12.02
Max	-2.45	25.99	-6.63	25.98	19.75	10.14	-10.41	21.97	29.73	-3.64	-2.24	29.91
Subject-1-Left Arm												
IE at 90°	Acromion				Center Point				MidPoint			
Angle	A/P	S/I	M/L	Resultant	A/P	S/I	M/L	Resultant	A/P	S/I	M/L	Resultant
Min	-5.68	35.59	-1.17	36.06	-4.94	-1	-2.46	5.61	-17.03	-21.2	-12.56	29.96
Max	-8.14	36.61	-14.59	40.24	3.3	-0.97	-8.57	9.23	20.88	-21.51	-17.58	34.75
Subject-2-Left Arm												
Angle	A/P	S/I	M/L	Resultant	A/P	S/I	M/L	Resultant	A/P	S/I	M/L	Resultant
Min	-7.02	35.2	0.11	35.89	-4.49	0.51	-11.51	12.37	-6.65	-9.87	-29.6	31.9
Max	-3.55	33.03	-12.66	35.55	13.67	-1.14	-9.38	16.61	29.24	-10.65	-19.02	36.47
Subject-3-Left Arm												
Angle	A/P	S/I	M/L	Resultant	A/P	S/I	M/L	Resultant	A/P	S/I	M/L	Resultant
Min	-7.95	4.69	2.13	9.48	-15.71	-6.9	-14.95	22.76	-26.53	-12.11	-19.38	35.02
Max	1.7	9.25	-19.21	21.39	23.73	-3.46	-12.46	27.03	29.76	-8.25	-22.9	38.44
Subject-4-Left Arm												
Angle	A/P	S/I	M/L	Resultant	A/P	S/I	M/L	Resultant	A/P	S/I	M/L	Resultant
Min	26.18	24.83	-10.26	37.51	11.66	5.69	-18.9	22.93	-1.45	-9.93	-18.67	21.2
Max	-9.79	24.18	10.05	27.96	11.77	7.68	6.96	15.69	15.24	-6.83	-7.46	18.29
Subject-5-Left Arm												
Angle	A/P	S/I	M/L	Resultant	A/P	S/I	M/L	Resultant	A/P	S/I	M/L	Resultant
Min	0.51	27.13	7.92	28.27	-10.31	8.72	-10.65	17.2	-19.24	1.31	-22.45	29.59
Max	-8.01	32.18	1.35	33.18	14.5	15.06	1.02	20.93	28.74	6.17	-3.12	29.56

Table 8: COR Errors and their resultants values for the external rotation at side movement at the minimum and maximum elevation angle.

Subject-1-Right Arm												
IE at Side	Acromion				Center Point				MidPoint			
Angle	A/P	S/I	M/L	Resultant	A/P	S/I	M/L	Resultant	A/P	S/I	M/L	Resultant
Min	NAN	NAN	NAN	NAN	NAN	NAN	NAN	NAN	NAN	NAN	NAN	NAN
Max	NAN	NAN	NAN	NAN	NAN	NAN	NAN	NAN	NAN	NAN	NAN	NAN
Subject-2-Right Arm												
Angle	A/P	S/I	M/L	Resultant	A/P	S/I	M/L	Resultant	A/P	S/I	M/L	Resultant
Min	6.95	33.39	-14.78	37.17	-12.86	15.24	-18.05	26.89	-25.74	4.08	15.38	30.26
Max	-14.41	35.81	-1.63	38.64	-12.73	19.25	22.71	32.38	24.16	17.3	28.15	40.93
Subject-3-Right Arm												
Angle	A/P	S/I	M/L	Resultant	A/P	S/I	M/L	Resultant	A/P	S/I	M/L	Resultant
Min	-11.37	-1.84	3.81	12.13	-8.66	5.7	7.36	12.71	-20.46	-2.07	14.3	25.05
Max	16.45	-1.6	5.5	17.42	17.32	7.91	2.83	19.26	27.74	2.4	12.69	30.6
Subject-4-Right Arm												
Angle	A/P	S/I	M/L	Resultant	A/P	S/I	M/L	Resultant	A/P	S/I	M/L	Resultant
Min	16.44	13.22	5.43	21.78	1.84	12.76	-0.31	12.9	-2.94	-2.88	22.16	22.54
Max	18.27	19.54	-12.16	29.39	3.83	19.3	-3.88	20.06	18.36	4.48	15.34	24.35
Subject-5-Right Arm												
Angle	A/P	S/I	M/L	Resultant	A/P	S/I	M/L	Resultant	A/P	S/I	M/L	Resultant
Min	6.21	4.55	12.92	8.49	-1.41	10.71	14.8	11.47	-17.7	-0.72	18.94	18.24
Max	6.07	2.98	-20.73	4.99	12.75	10.96	-15.93	16.33	27.62	4.69	-5.91	27.91
Subject-1-Left Arm												
IE at Side	Acromion				Center Point				MidPoint			
Angle	A/P	S/I	M/L	Resultant	A/P	S/I	M/L	Resultant	A/P	S/I	M/L	Resultant
Min	19.22	20.48	14.67	31.69	3.85	-0.5	12.3	12.9	-20.22	-9.89	-9.14	24.3
Max	-17.49	25.32	7.31	31.63	-10.36	4.07	-7.43	13.38	19.65	-2.62	-22.27	29.82
Subject-2-Left Arm												
Angle	A/P	S/I	M/L	Resultant	A/P	S/I	M/L	Resultant	A/P	S/I	M/L	Resultant
Min	2.66	12.08	7.85	14.66	-7.25	-3.87	8.72	11.98	-21.57	-9.92	-12.35	26.76
Max	-2.8	17.27	-0.89	17.52	-6.09	4.98	-18.17	19.8	19.17	4.89	-28.63	34.8
Subject-3-Left Arm												
Angle	A/P	S/I	M/L	Resultant	A/P	S/I	M/L	Resultant	A/P	S/I	M/L	Resultant
Min	-20.56	-0.64	5	21.17	-9.71	1.94	0.23	9.9	-21.98	-1.3	-8.16	23.48
Max	11.66	2.73	-22.87	25.82	9.69	7.05	-12.29	17.16	20.32	5.09	-22.36	30.64
Subject-4-Left Arm												
Angle	A/P	S/I	M/L	Resultant	A/P	S/I	M/L	Resultant	A/P	S/I	M/L	Resultant
Min	32.23	1.85	31.24	44.93	24.84	3.46	24.31	34.93	36.7	-4.59	7.15	37.67
Max	-16.1	3.91	0.92	16.59	-18.98	9.24	10.85	23.73	-38.4	-1.68	14.64	41.13
Subject-5-Left Arm												
Angle	A/P	S/I	M/L	Resultant	A/P	S/I	M/L	Resultant	A/P	S/I	M/L	Resultant
Min	9.78	16.94	-0.24	19.56	1.21	16.11	-0.27	16.16	-14.7	10.55	-9.81	20.58
Max	-11.49	20.8	8.19	25.13	-2.39	19.5	0.14	19.65	17.02	17.44	-2.06	24.46